An investigation of the hydrodynamic forces on a jointed oscillating eel-like structure

by

Claus Christian Apneseth

Submitted in accordance with the requirements for the degree of
Doctor of Philosophy

The University of Glasgow
Department of Naval Architecture and Marine Engineering

January 2006

The candidate confirms that the work submitted is his own and that appropriate credit has been given where reference has been made to the work of others.

Abstract

This study is an investigation of the forces developed by a jointed oscillating structure resembling a mechanical eel. The structure consists of rigid segments that oscillate from side to side to facilitate self-propulsion; this study aims to develop a simple numerical method that can be used for the engineering design of such a structure. The project was undertaken as a natural first step towards the design and construction of autonomous underwater vehicles (AUV) based on this concept.

Published literature on fishlike propulsion and its mechanical implementation is investigated before a brief examination of the flow field surrounding such a structure is presented. Simple numerical methods, which try to predict the forces from this type of structure are then evaluated before the numerical implementation of some of them are presented.

To evaluate the various numeric methods a physical structure was built and tested in a towing tank. The design of this structure is presented along with the physical measurements from it. The structure had two moving segments and a head segment. The structure was tested in three different scenarios:

- *The two segments moving as one with no forward speed*
- *The two segments moving independently without forward speed*
- *The two segments moving independently with forward speed*

As all the numerical methods depend on quasi-empirical force coefficients, their solutions cannot be directly compared to the measured values. The force measurements were therefore used to compute these force coefficients. The consistency of these force coefficients can then be seen as a validation of the numerical method. The method that was found to predict the forces best was the Morison Equation with Keulegan-Carpenter number dependent force coefficients (Graham 1980).

With the best-fit force coefficients, the Morison Equation was found to be able to predict the thrust from the scenario when the two segments moved together to within 15 % of the measured value. However, in the second scenario with the two segments moving independently, the generated thrust was substantially over-predicted, in some

cases by nearly 200 %. The self-propulsion speed was however only over-predicted by about 30 % in the worst cases and in most cases by significantly less.

The Morison Equation with Keulegan-Carpenter number dependent force coefficients can therefore be seen to predict the average forces acting on a single segment oscillating structure well. It can also be seen to predict the self-propulsion speed of a two segment oscillating structure quite well and can thus be used for design purposes. This study however shows that the time history of the forces developed by such a structure is not well predicted by the Morison Equation and neither is the thrust developed in the bollard-pull condition for a two-segment structure.

Acknowledgements

Many people have helped me with this thesis and the project that it describes. Jon Erik Borgen and the people at Inocean in Oslo were the ones who initially got me started and they have helped me both financially and with good suggestions throughout.

When I began investigating fish-like propulsion I sent many requests for information to numerous biologists. Professor Videler was one of several whom always answered my questions promptly and for this, I am grateful.

At the Department of Naval Architecture and Marine Engineering, I have received a lot of help. My two supervisors, Dr. Day and Mr. Clelland have been both helpful and approachable and luckily, they haven't usually both been too busy at the same time. The technical staff at the tank have also been helpful and I would especially like to thank Bill, who made the McEel and Charlie who managed to squeeze my project into some non-existent tank time on numerous occasions. The secretaries with Thelma as the most notable one have also helped me in navigating through the bureaucratic jungle that a modern university is. And I would also thank my colleagues who have made these years more enjoyable and interesting. Edd and Dag, you guys are next.

I would also like to thank all the governmental and non-governmental organisations that have allowed me to study these last seven years. From Norway, I have been supported mainly by Lånekassen, but also by Lise and Arfinn Hejers scholarship and the scholarship for young conservative naval architects. From Britain, I have received an ORS scholarship and a scholarship from the University of Glasgow.

Last but by no means least I would like to thank my girlfriend and partner Sigrid Moldestad. Not only has she been understanding and sympathetic but as she is a qualified architect, she has also been able to help me with AutoCad and other illustration tools that at times have threatened my sanity.

There are probably many more people and bodies that I should have thanked but that would make this acknowledgement too long for anyone to read.

Thanks to all of you!

Table of Contents

Table of Figures

Table of Tables

Nomenclature

Roman letters:

A	Acceleration in global coordinates
a	Acceleration in local coordinates
Ca	Coefficient of added mass
Cd	Coefficient of form drag
Cm	Coefficient of mass
Cm_0	Coefficient of mass for attached flow
Cn	Coefficient of normal skin friction
Ct	Coefficient of tangential skin friction
D	Diameter of the eel
F	Force
f	The frequency of the oscillations
Kc	Keulegan-Carpenter number
L	Length of each moving segment
l	The length along each segment from its front most joint
M	Moment in the joint
m	Mass of the segment
N	Normal unity vector for the segment
R	Straight-line resistance
T_i	Tangential unity vector for the i-th segment
T	Period of oscillations
U	The advance speed of the eel
V	Velocity in global coordinates
v	Velocity in local coordinates
X	Global X-coordinate of the nodal point

x	The global X-coordinate of the centre of the element
Y	Global Y-coordinate of the nodal point
y	The global Y-coordinate of the centre of the element

Subscripts:

i	The counter for the segments
j	The counter for the elements of each segment
k	Number of computational elements used per segment
n	Number of moving segments
T	Tangential to the segment in question
$\perp$	Perpendicular to the segment in question

Greek letters:

α	Internal angle of vortex shedding edge
Δ	The displacement
η	The local coordinate of the segment perpendicular to it
η_T	The transport efficiency
θ	Angle between segment and global coordinate system of the eel
ρ	The specific mass of the fluid
ξ	The local coordinate of the segment along the segment
ω	The angular velocity vector of the segment

1 Introduction

In this study, fishlike propulsion is investigated from an engineer's perspective. As such, some parts of it will be exploring the propulsive methods of live fish, as in numerous previous studies. In the current study, however the understanding of fish propulsion is only sought as a means to an end. The real goal of this study is to facilitate the construction and operation of man-made under sea vehicles that utilize fishlike propulsion.

If fishlike propulsion is ever to become a common form of under sea propulsion for manufactured vehicles it has to have one or more benefits compared to existing solutions. These benefits could be better manoeuvrability, higher transport efficiency, greater impact resistance due to the lack of a propeller, or other advantages. Two applications in particular seem to be well suited to this novel form of propulsion: mine hunting in the surf zone and scientific expeditions into the kelp forests. A miniature submarine built like an eel should be as capable of venturing into these two areas as its natural counterpart.

In order to be able to design and optimize an eel-like vehicle the forces developed by fishlike propulsion have to be understood. To understand the forces developed by fishlike propulsion this study starts by investigating the kinematics of a fishlike propulsion device. Various motion patterns that the device might undertake are investigated to give an understanding of the types of hydrodynamic forces that are involved. In the next chapter, various hydrodynamic methods that can be used to determine these forces are presented. The mathematical implementation of these various hydrodynamic methods is then presented in chapter 4. To evaluate the different methods a physical model of a mechanical eel was built. This device, which will be denoted the McEel for the remainder of this thesis is presented in chapter 5. The remainder of this thesis is devoted to the comparisons of the various hydrodynamic models with the measured data from the McEel.

It is however important to emphasize that the project undertaken is not as straightforward as comparing a calculated solution with a measured result. This is because most of the hydrodynamic models rely on one or more quasi-empirical hydrodynamic force coefficients. The data from the measured tests were therefore to some extent used by the numeric predictions. Numerous tests were therefore performed to check the consistency of the hydrodynamic coefficients and thus the

validity of the various models. This was done to evaluate whether any of these methods could be used to predict the forces from un-tested motion patterns.

It is also important to emphasize that the overriding aim of this thesis is not to make a mechanical swimmer that replicates nature as closely as possible but rather to make one that it is possible to analyze and more importantly one that is practical to implement.

1.1 Fish swimming and mechanical replication

For many years, the seemingly effortless swimming of fish and other marine animals has intrigued laymen and scientists alike and it has been the subject of several scientific studies. C. M. Breder (1926) classified the various methods for aquatic propulsion. The fastest and most normal mode for fish to propel themselves is through transverse flexing of the trunk and tail portions of the body setting up a backward travelling wave. Breder described this type of locomotion as being either ostracii-, carangi- or anguilli-form locomotion depending on how big a portion of a wavelength was present in the body. The two extremes are the ostraciiform locomotion characterized by a near simultaneous contraction of all the muscles on alternating sides of the spinal cord and anguilliform locomotion characterized by the presence of more than half a wavelength along the length of the fish. The carangiform locomotion is the mode between the two and this is the mode of locomotion of faster fish like tuna, mackerel and marlin.

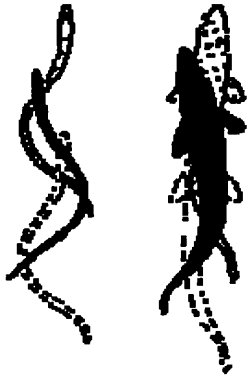

Figure 1-1: Anguilliform locomotion (left) and carangiiform locomotion (right) (Gray 1936)

Later researchers, e.g. Videler (1993), have shown this classification to be an over simplification but the terms are widely accepted and will for that reason be used in

this text. From an engineering point of view it might be of more interest whether a high aspect ratio foil like the one found on many fast fish is needed or not. This feature is often referred to as a "lunate" tail as it often curves backwards like a new moon. In such a perspective, the fish that employ such a device might be said to be carangiform swimmers whilst the ones that use a larger part of the body for propulsion might be called anguilliform swimmers. In this context, the ostraciiform swimmers will be the ones that use a rigid single flapper for their propulsion.

To verify his theories about fish locomotion Breder (1926) built two mechanical prototypes, one replicating ostraciiform locomotion and the other anguilliform locomotion. The ostraciiform model in particular is discussed in some detail as its propulsion contradicted some earlier theories. The propulsive effectiveness is not quantified for either model although the ostraciiform model is said to have: "moved forward with a sure and steady gait".

The first scientist to give an accurate description of fish kinematics was Sir James Gray. Gray (1936) reported that dolphins swim seven times faster than their muscle mass should allow them. This became known as Gray's paradox. The assumptions were that dolphins and porpoise, like other mammals, can generate one horsepower per 100 lb. of muscle tissue and that the drag of an actively swimming animal was equivalent to a towed, straight model of the same geometry. It is interesting to note that in the initial paper Gray more than indicated that the latter assumption was probably not true. His findings are however still referred to. Gray also stated that discovering whether aquatic animals were efficient swimmers was "of considerable interest" since it "would indicate whether the mechanism of swimming is or is not substantially more efficient than those, at present available for the propulsion of a torpedo or airship."

To investigate this paradox Gray enlisted one of his students, and Lighthill (1960) produced what has since been regarded as the standard analytical model for anguilliform locomotion. With the small amplitude elongated body theory, he explained how thrust is generated from added momentum experienced by an undulating body. The theory shows that the mean thrust can be calculated from the displacement and angle of the tip of the tail only. He also predicted that for maximum efficiency the speed of the backward travelling wave should be 5/4 of the desired forward speed.

One of the first and few naval architects to relate the principles of fish propulsion to ship propulsion was R. W. L. Gawn. He summarized (Gawn 1949) the knowledge of fish propulsion that he found applicable to naval architects. In his paper he states, "It is clearly of importance to ship designers to ascertain the explanation of fish locomotion." Gawn kept on studying fishlike locomotion but never seems to have found an economic use for his findings.

More recently, the biologist John J. Videler has been at the centre of fish propulsion research. In the book "Fish Swimming" (Videler 1993) he summarizes current knowledge of the field. He also explains the application of Lighthill's theory in a lucid manner after having spent a substantial amount of effort comprehending it.

Professor Akiro Azuma has written a similar book called "The Biokinetics of Flying and Swimming" which approaches the same subject from the engineer's perspective (Azuma 1992). In the book, he terms carangiform and ostraciiform locomotion to be swimming by fanning and anguilliform locomotion to be swimming by snaking. These terms might be more descriptive for the non-biologist. The book is however highly technical in nature and describes how most fish are subject to both inertial and viscous effects. According to Professor Azuma, all but one model for fish propulsion fails to consider both of these forces and as such, the work of Lighthill and others is only valid in a certain range of Reynolds number.

The one model for fishlike propulsion that does consider both resistive and reactive forces according to Professor Azuma is the one undertaken by William J. Vlymen (1974). This paper develops a method for calculating the energy spent by larval anchovy in their swimming. The method considers both perpendicular and tangential drag forces but when it comes to added mass effects, it only deals with perpendicular forces. This is because the specie in question is considered hydrodynamically equivalent to a spherical head with a long flat plate behind it. The tangential drag force thus stems from skin friction whilst there is no added mass in the tangential direction as the sections of the body that are involved with thrust generation have no cross sectional area.

The naval architect who has been most central to the exploitation of fishlike propulsion in recent years is Professor Michael S. Triantafyllou of Massachusetts Institute of Technology. In the early 1990s, he and his associates started experimenting with flapping foils and discovered that they had a high propulsive

efficiency of more than 87% (Triantafyllou 1996). They also discovered the importance of the Strouhal number to the efficiency of fishlike propulsion. In terms of the propulsive mechanism, Professor Triantafyllou placed great emphasis on the reverse von Karman vortex street that forms behind a swimming fish. Triantafyllou was however also interested in the possible drag reducing secrets of fish, and in order to make accurate measurements of a fish he had his student David S. Barrett make the mechanical fish known as the Robotuna (Barrett 1996).

The first Robotuna had eight rigid, jointed vertebrae at its core. The outer skin of the vehicle was flexible though, just like on most of the later mechanical swimmers constructed at M.I.T. The swimming mechanism was operated by electrical motors attached to the carriage that supplied their power via a wire and pulley system through a mast. The Robotuna generated most of its thrust with a high aspect ratio tail and can safely be classified as a carangiform locomotion device. The Robotuna was a success in that it reached high efficiencies and provided new insight into fish propulsion. It does not appear to have been a commercial success however. Professor Triantafyllou took out a patent on a manned underwater vehicle for Special Forces operations in cooperation with the US Navy (Triantafyllou 1999) but it is unknown how many, if any, were ever built.

In recent years, there has also been an interest in fishlike propulsion from the robotic community. Ørjan Ekeberg (1993) has published a study of what is essentially a robotic analysis of lamprey swimming. The hydrodynamic model that he employs is a rudimentary one though. In the paper, he states that inertial forces dominate at higher speeds. This seems a bit odd, as inertial forces are independent of the forward speed whilst the drag forces should increase with it. He ends up using only drag forces for what he claims to be a high Reynolds number scenario though. To simplify his hydrodynamic model further he states that the size of the tangential drag forces "does not influence the resulting swimming very much." He therefore neglects these forces as well and ends up with an equation that is essentially the drag part of the Morison Equation.

McIsaac and Ostrowski (2003) have also studied fish like propulsion extensively. Working with the University of Pennsylvania and funded in part by the Office of Naval Research in the USA they have built two eel like robots called Reel I and Reel II. Both of these robots were free swimming and capable also of propelling

themselves on firm ground. The hydrodynamic model employed to predict the motions of these robots was essentially the one developed by Ekeberg in which only perpendicular drag forces are considered in the propulsion.

2 The kinematics of an eel

2.1 Introduction

In order to determine a suitable hydrodynamic model for the analysis of a mechanical eel it is important to establish first the eel's kinematics. In particular, it is important to evaluate what kind of flow regime it (or its natural counterpart) encounters. In this chapter, it will be assumed that the water surrounding the eel can be considered stationary in earth fixed coordinates. As the eel starts to move, either by oscillating or by moving forward, this is no longer strictly true. The real flow is in other words approximated to the flow without the perturbations caused by the eel. This approximation is similar to the one normally used by the Morison Equation and seems suitable to give an overview rather than a detailed description of the flow around the eel.

Some clarifications of basic assumptions might be required before the kinematics of the eel is explained. In nature, an eel swimming in a straight line at low to moderate speed will have minimal head movement in the lateral plane (Gillis 1998). This is modelled in the physical tests by the McEel having its first segment rigidly fixed to a sting leading up to the towing tank carriage. The kinematics of this segment is therefore no different from any other underwater body moving in a straight line with a constant speed. This segment will therefore be excluded from the following kinematical description.

The exact kinematics of a segmented eel will depend on numerous variables. These are:

- The number of segments
- Amplitude and frequency of oscillations in the various joints
- Phase angle between the joints
- Physical size of the various segments
- Relative motion between the head of the eel and the water surrounding it

This description of eel kinematics will therefore be limited to what is in essence a description of the kinematics of the physical McEel. Many of the issues discussed will however be valid also for other types of eel-like vehicles.

The specific size and configuration of the physical McEel will be discussed in detail later. The main features are however as follows:

- It has a 410 mm long head and two 200 mm long moving segments.
- The joints are controlled independently.
- The maximum oscillation in each joint is 45 degrees relative to the segment in front of it.

With this introduction of the McEel particulars, the concept of segment lengths has also been introduced. In nature, an eel will swim with a backward travelling wave of nearly linearly increasing amplitude towards the tail (Gillis 1998).

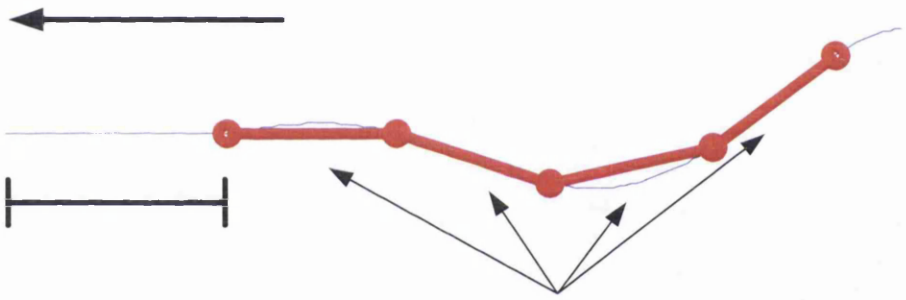

Figure 2-1: A jointed structure replicating the motions of a real eel.

Figure 2-1 shows how 4 rigid segments, drawn with a thick red line try to replicate the mathematical function of the real eel, shown here in blue, at an arbitrary point in time. As the amplitude of oscillation increases towards the tail, the mechanical eel will be required to make more rapid angular changes in this region. A mechanical eel with shortening segments towards the tail would therefore be better at replicating the idealized function mentioned in section 1.1. As the McEel is not trying to replicate every aspect of eel propulsion, the simpler solution of having the two moveable segments of the same length was chosen.

To differentiate between the various swimming patterns employed by the McEel a simple notation system was developed in which each one was given a three number designation. All angles are in degrees and the system is as follows:

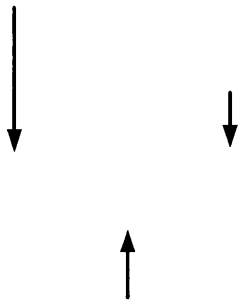

Figure 2-2: The notation system of the swimming patterns

In addition to the three-numbered designation, there are two other variables in the motion pattern of the McEel that need to be introduced; namely the forward speed and the frequency of oscillation. The forward speed will be measured in m/s and the frequency of oscillation will be measured in Hz. In theory, one could imagine a swimming pattern in which the fundamental frequencies of the various joints would not be equal but such a pattern would deviate from what is seen in nature (Gillis 1998) and all tests discussed in this thesis therefore have a uniform excitation frequency throughout. A scenario in which the angular movements in the joints consist of more than one frequency is far more plausible. Closer inspections of the angular motion in the various joints (see Appendix A) show that the over all mathematical function of the eel, with a sinusoid of linearly increasing amplitude, is best replicated if the backmost joints make a more rectangular motion than that of one pure sinusoid.

It has however been an aim to limit the number of variables in the experimental section of this thesis, as it is not aimed to be an exhaustive study. For this reason and the reason stated for having the segments the same length the angular motion of the joints will be assumed to consist of just one sinusoid.

2.2 The simplest case

In examining the kinematics of the eel, it is natural to start with the simplest case. A 30-30-0 run with zero forward speed and a frequency, f, of 0.15 Hz is therefore the example of the simplest motions that will be examined in some detail. This

swimming style is an example of ostraciiform locomotion. As this is a motion, in which the two joints move in unison it will be referred to as a single flapper scenario in this text.

Starting with this pattern, the flow regime encountered by the eel can be investigated. Under the assumptions stated the relative velocity and acceleration between the fluid and the eel could be computed. It is however important to emphasise that there is no immediate correlation between these velocity and acceleration vectors and the corresponding drag and inertia forces. To convert the following velocity and acceleration vectors to forces they have to be multiplied by various other factors such as the density of the fluid, the projected area, the volume and the appropriate hydrodynamic force coefficients.

The velocity and acceleration vectors are of interest on their own however as they give an indication as to which flow regime the mechanical eel operates in. To show the magnitude and direction of these vectors four time steps are depicted in Figure 2-3 to Figure 2-6. For each time step, part A depicts the velocity vectors and part B depicts the acceleration vectors:

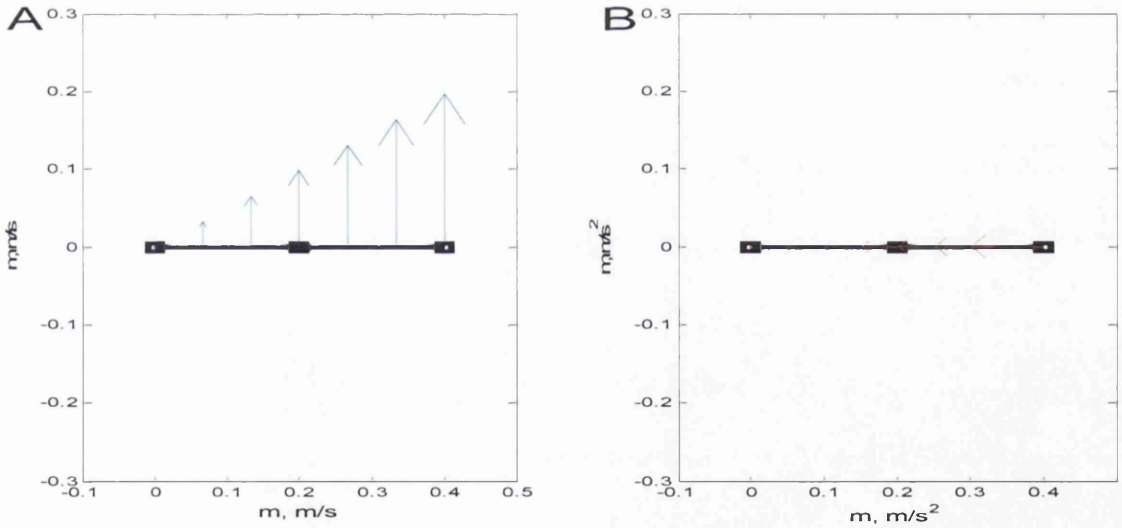

Figure 2-3: Time step 1, t = 0

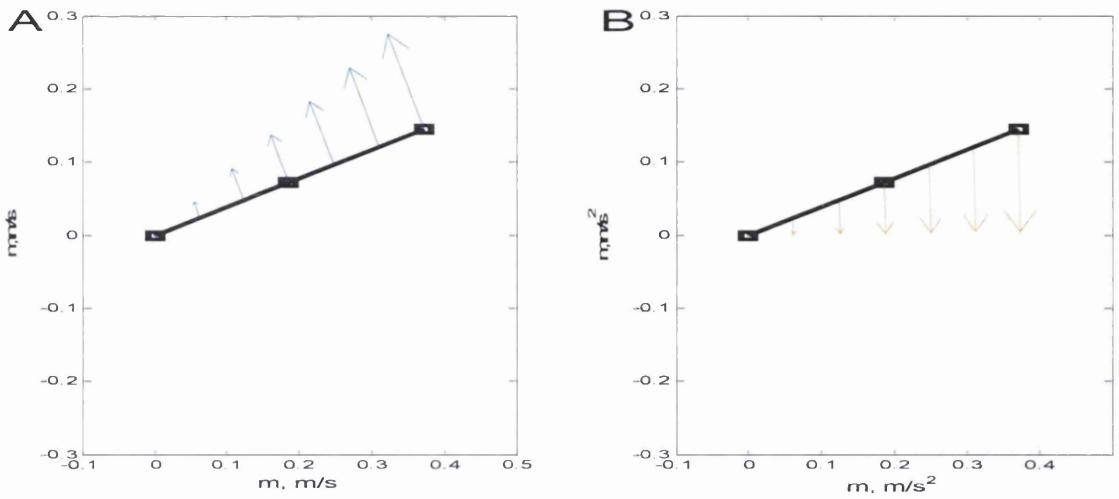

Figure 2-4: Time step 2, t = T/8

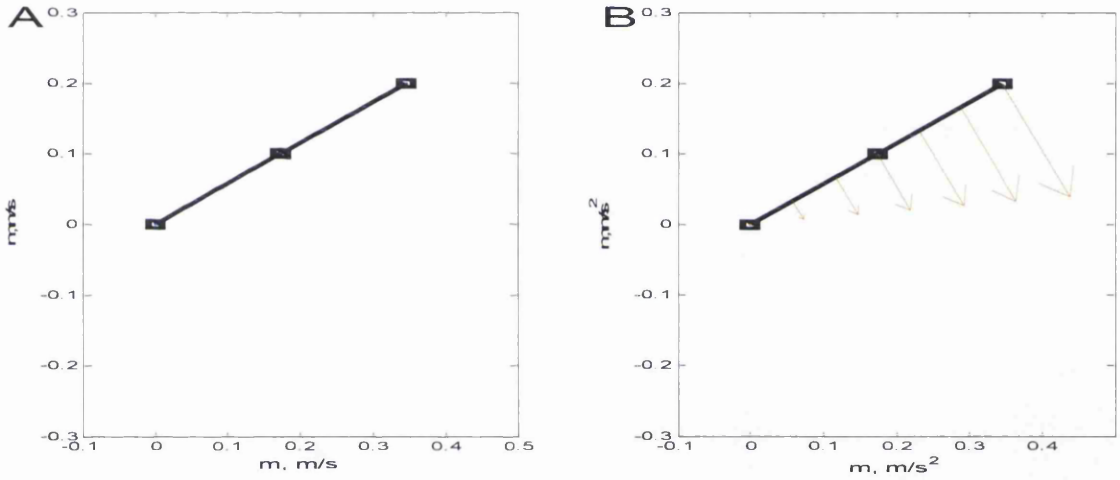

Figure 2-5: Time step 3, t = T/4

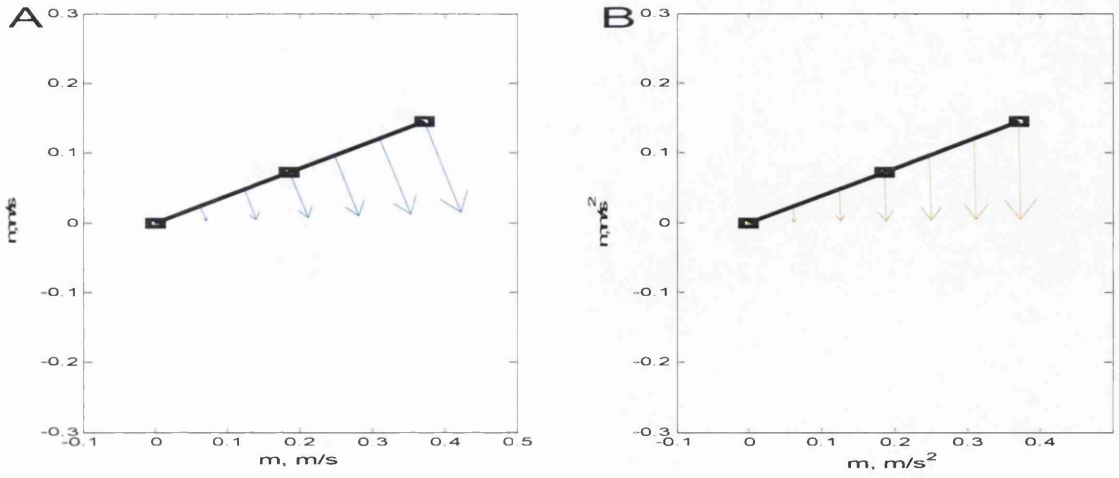

Figure 2-6: Time step 4, t = 3T/8

The four time steps constitute half a cycle. As the motions are harmonic, the second half of the cycle would be a mirror image of those shown above. The three rectangles along the eel represent its nodal points. The leftmost rectangle is therefore the front joint, the middle one is the middle joint and the rightmost one represents the tip of the tail. The scale of these graphs are such that vectors of 1 m/s and 1 m/s^2 would be drawn as the same length as a 1 m long object.

As the blue lines in part A of the figures depict the relative velocity between the eel and the stationary fluid; it can be seen that this is always perpendicular to the eel itself except in Figure 2-5 when the eel is at its extreme angle at which point the velocity vectors are zero. In the simple swimming pattern, the flow field can therefore be considered one of pure cross flow as far as the velocity is concerned.

The red lines in part B of the figures depict the relative acceleration between the nodal points of the eel and the stationary fluid. As can be seen the acceleration vectors are at varying angles to the segments. When the eel is at its extreme angles as in Figure 2-5, the acceleration is at its maximum magnitude. At this point, the direction is perpendicular to the segments. At no other time step is this so.

As the eel passes through zero degrees in Figure 2-3, the acceleration vectors are tangential to the eel itself. As far as the acceleration is concerned, even this simple swimming pattern therefore deviates from a pure cross flow. Furthermore, it can be seen that the tangential component of the acceleration vector always points to the left. This is an important point as it means that a hydrodynamic model that treats eel like propulsion as one of pure cross flow may over-predict the mean forward thrust of this swimming pattern if the eel in question has non-zero cross sectional area. The reason for this being that such a model will neglect any added mass effects in the longitudinal direction of the eel and as this added mass only accelerates towards the left, it will in effect be a varying but negative force holding the eel back.

Another important point is that the acceleration vector and the velocity vector are of similar order of numeric magnitude. As explained in section 1.1 several hydrodynamic models of fish like propulsion neglects either inertial or drag forces. One must be very careful in making the connection between the relative size of the velocity and acceleration vectors and the relative size of the drag and inertial forces computed from them. Both the drag and inertial forces rely on several other variables such as volume and projected area as well as hydrodynamic force coefficients. It is

however interesting to note the relative size of the velocity and acceleration vectors as this relationship will clearly be an input to the decision of which hydrodynamic model to use.

2.3 A more complex scenario

As mentioned before a swimming eel will set up a backward travelling wave with increasing amplitude (Gillis 1998). A mechanical eel with rigid jointed segments of equal length would replicate this by having increasing amplitude oscillations in the joints and negative phase angle towards the tail. Using positive phase angles would mean that the wave would propagate forward and this would be equivalent to putting the eel in reverse gear. The third number in the swimming pattern designation therefore signifies the negative phase angle.

A swimming pattern that is closer to the real eel swimming style would be 30-40-60. This scenario will also be examined in some detail, as it might be hard to visualize. The excitation frequency, f, is still 0.15 Hz and the forward speed will remain zero to allow comparisons with the simpler scenario. For each time step, the velocity vectors are still depicted in part A of each figure while the acceleration vectors are depicted in part B:

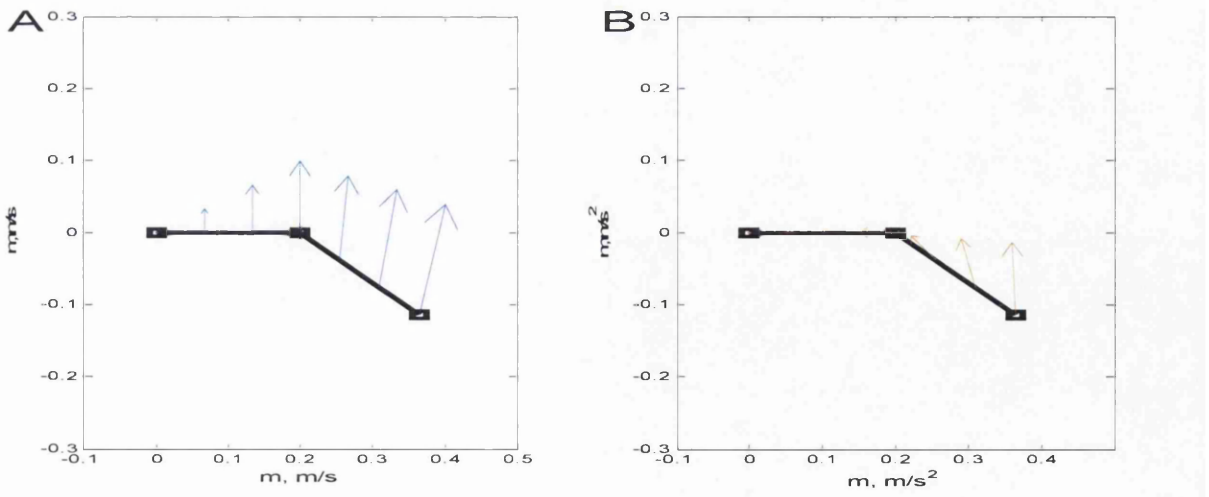

Figure 2-7: Time step 1, t = 0

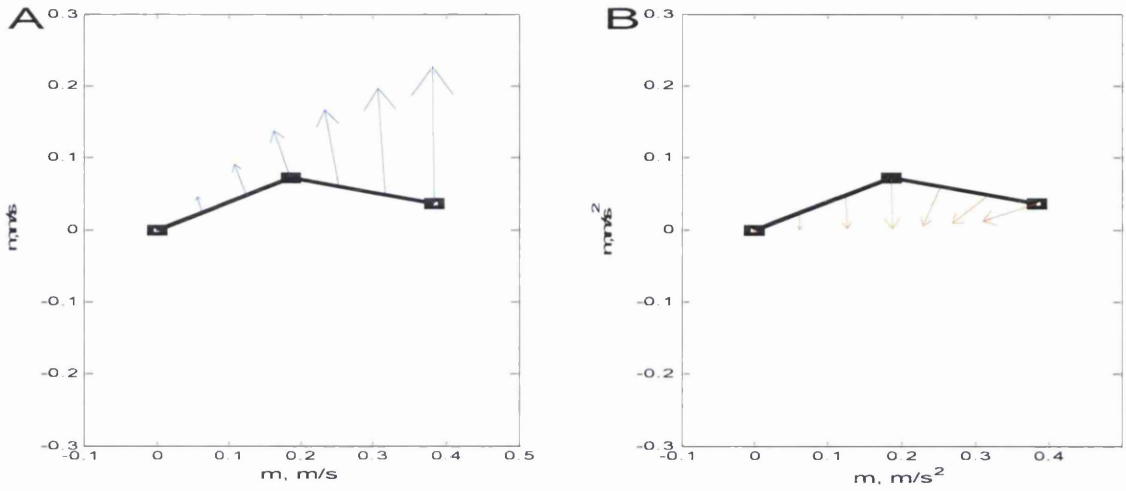

Figure 2-8: Time step 2, t = T/8

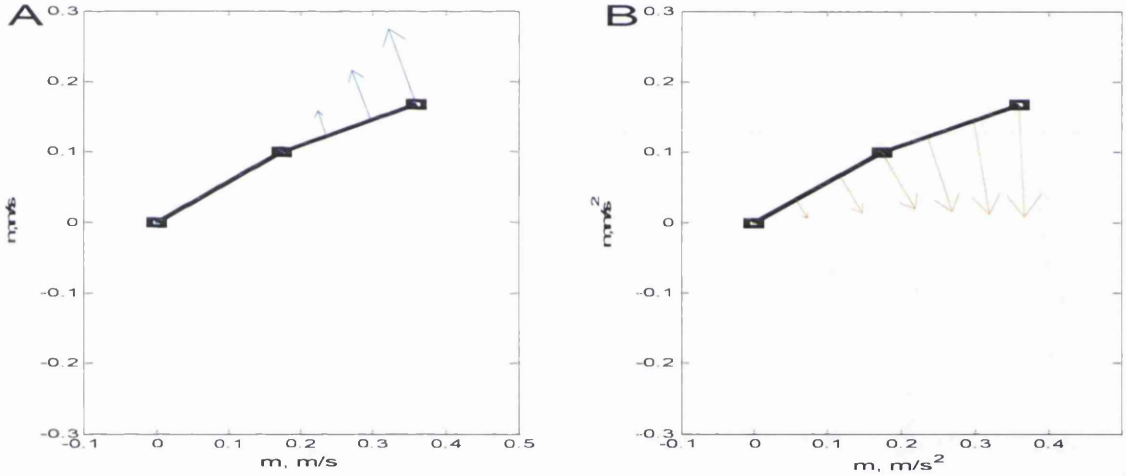

Figure 2-9: Time step 3, t = T/4

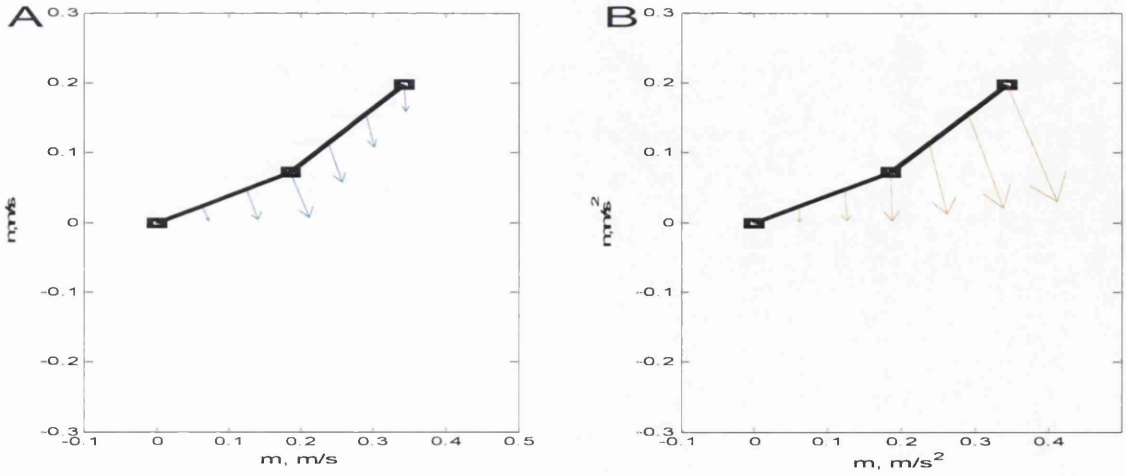

Figure 2-10: Time step 4, t = 3T/8

Again, four time steps constituting half a cycle are depicted.

In this scenario only the front segment experiences pure cross flow as far as the velocity is concerned. This is as expected as the motion of the front segment has not changed from the simpler swimming pattern.

Neither the acceleration vectors nor the velocity vectors of the backmost segment are perpendicular to the segment in this scenario. A complete hydrodynamic solution for predicting the forces generated by an eel like structure undergoing this type of motions therefore has to compute both drag and inertia forces in both the perpendicular and tangential directions.

As the exact path that the backmost segment follows in this scenario can be hard to visualize it is shown in detail:

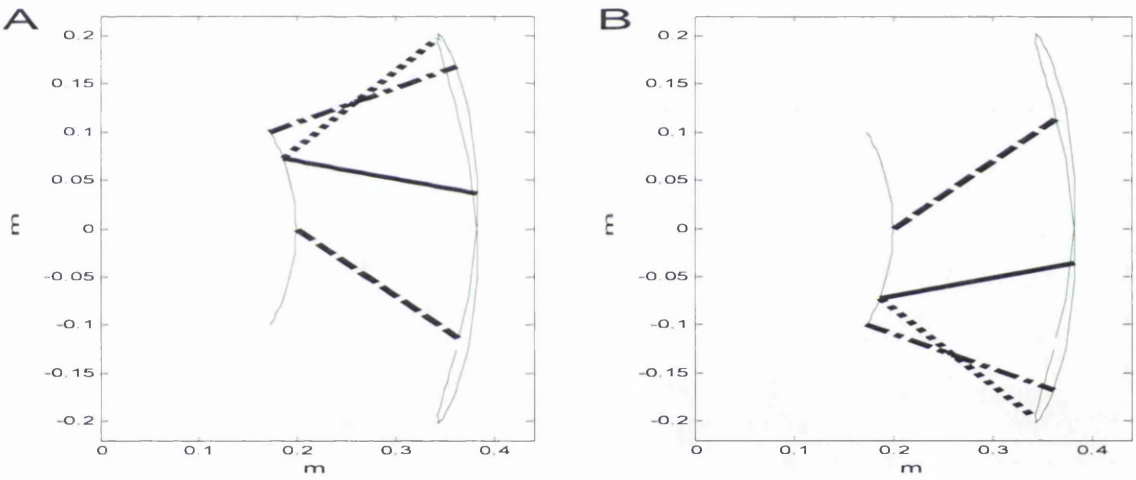

Figure 2-11: The path of the tail segment

In part A of this figure, the corresponding four time steps to the ones shown above are depicted. The dashed black line shows the tail segment at time step 1 whilst the solid black line is at time step 2. The dashed-dotted line is at time step 3 whilst the dotted line is at time step 4. The corresponding line styles in part B of the figure show time step 5, 6, 7 and 8 completing the cycle. The green lines in both parts of the figure show the paths that the endpoints of the segment follow.

As can be seen the tip of the tail no longer follows an arc. The path it follows is closer to a curved figure of eight. As the tail end of the tail segment moves outwards from its mean position it moves along the rightmost path of the figure eight and when it is moving back towards the centreline again it follows the leftmost path. This is

similar to what is seen in nature (Gillis 1996). It is thus confirmed that this pattern of motions is closer to those undertaken by anguilliform swimmers.

2.4 A scenario with forward speed

The two previous scenarios have been with zero forward speed. In naval architecture, this is equivalent to a bollard-pull test. Any free-swimming eel will however start from rest and it will therefore need to generate thrust in this state in order to reach a positive forward velocity. The bollard pull condition can therefore be said to be more elemental than the forward speed condition in addition to being mathematically less complex. For a complete solution of eel-like propulsion though, the forward speed scenario has to be investigated.

As noted earlier, various robotics researchers have chosen to neglect the inertia forces when analyzing the steady state swimming of their eels. This is based on the assumption that these forces are negligible in the Reynolds number regime in which the eels operate. The Reynolds number quoted in the paper by McIsaac and Ostrowski (2003) is 10000. As the McEel has two moving segments of 200 mm each and a 410 mm long head section this Reynolds number corresponds to an advance speed, U, of 0.0125 m/s. Raising this speed to a more realistic 0.1 m/s would yield a Reynolds number of 80000 which is still within the range of $400<Re<400000$ in which the paper claims their assumptions of negligible inertia to be valid.

Some of the numeric models described later in this thesis rely on the Keulegan-Carpenter number and for this reason it may be of interest to see which Kc number this scenario equates to. In order to compute the Kc number a span or height is needed. As will be described in section 5.5 the height of the McEel was 0.2 m throughout most of its length. If this is assumed as a height also for this numeric example the Keulegan-Carpenter number for this scenario would range from zero at the front end to 6.33 at the tip of the tail.

Again, four time steps are depicted in Figure 2-12 to Figure 2-15. For each time step, the velocity vectors are still depicted in part A of each figure while the acceleration vectors are depicted in part B:

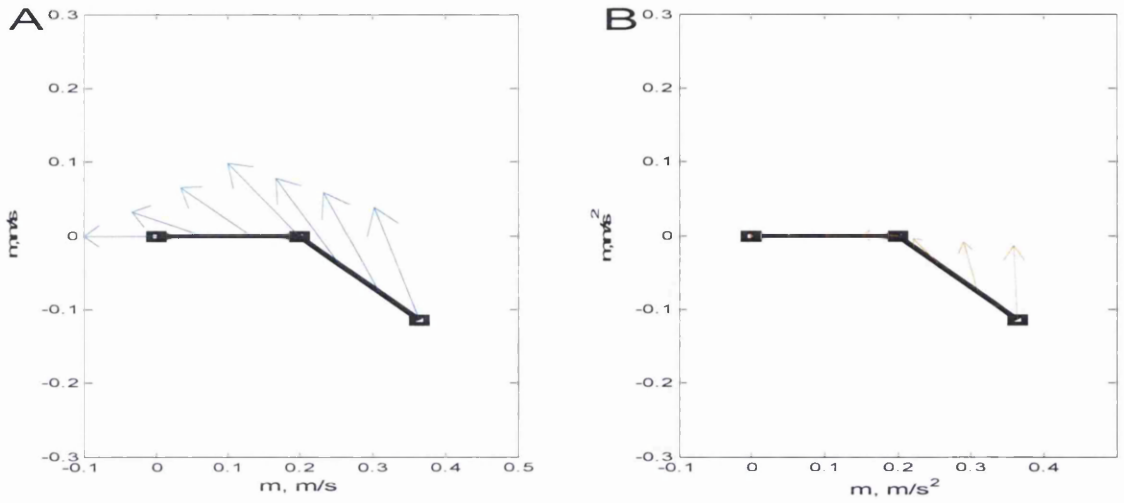

Figure 2-12: Time step 1, t = 0

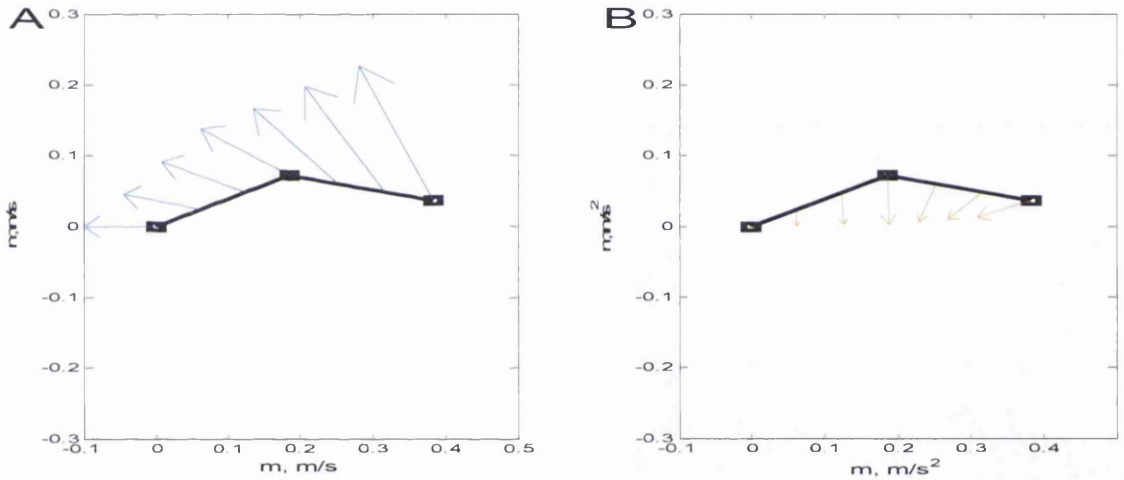

Figure 2-13: Time step 2, t = T/8

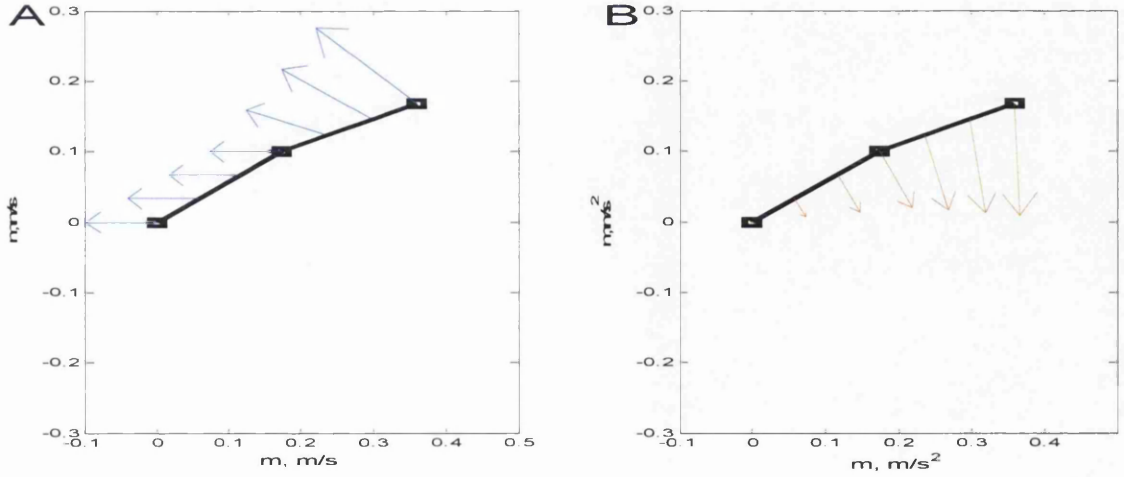

Figure 2-14: Time step 3, t = T/4

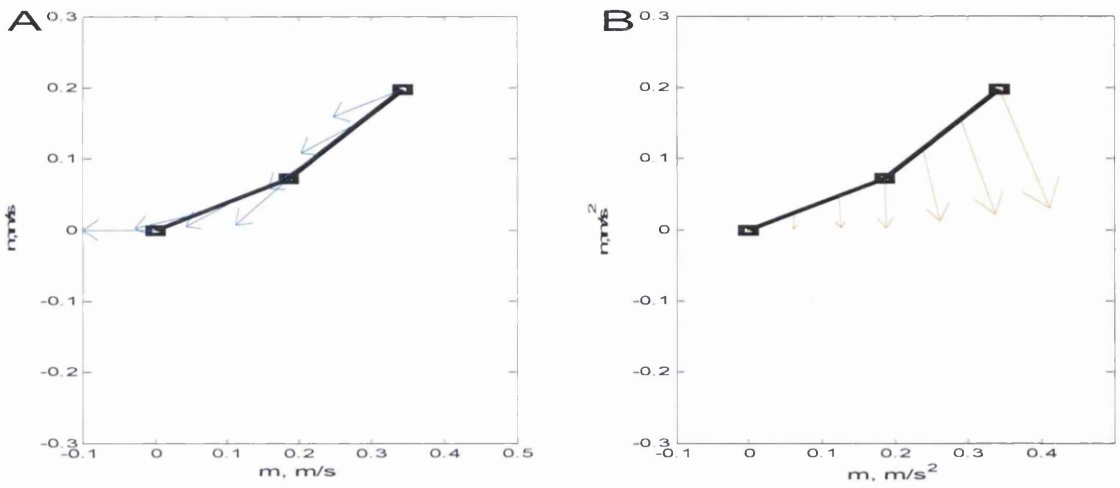

Figure 2-15: Time step 4, t = 3T/8

Not surprisingly, this moderate advance speed does not alter the numeric size of the velocity and acceleration vectors profoundly. In the first two time steps, the velocity vectors are numerically bigger than the acceleration vectors whilst in the last two time steps they are more similar in size. It is however important to emphasize that the velocity used by Ekeberg (1993) is the normal velocity. This normal velocity is numerically not of a different order of magnitude than that of the equivalent normal acceleration at any time step. How the normal acceleration and normal velocity relate to drag- and inertial-forces is evidently dependent on what hydrodynamic model one uses but these graphs should indicate that the inertial forces are not necessarily without importance.

It is important to emphasize that these graphs were drawn for a low excitation frequency, f, of 0.15 Hz and a moderate speed, U, of 0.1 m/s. It would be of interest to compute the advance velocity of the wave of the eel in comparison to the eel it self. It is however not obvious how this could be done. In order to compute any velocity a distance and a time is needed and it is not evident what the wavelength for 30-40-60 swimming pattern is. As there is a 60-degree phase difference between the two joints it is tempting to say that they together make up 2/6 of a wavelength but the distance between them in the x-direction varies with time. The two angles are:

$$\theta_{front} = \frac{\pi}{6}\sin\left(2\pi f\, t\right)$$
$$\theta_{tail} = \frac{2\pi}{9}\sin\left(2\pi f\, t - \frac{\pi}{3}\right)$$

Equation 2-1

In these equations, t, is the time variable. The mean longitudinal position of the tip of the tail can be computed:

$$X_{tail} = \frac{L}{T}\int_0^T \left(\cos\left(\frac{\pi}{6}\sin\left(2\pi f\ t\right)\right) + \cos\left(\frac{2\pi}{9}\sin\left(2\pi f\ t - \frac{\pi}{3}\right)\right)\right)dt$$

Equation 2-2

In this equation T is the period of oscillation and L is the length of each segment. It is not easy to solve Equation 2-2 analytically but a numerical solution is straightforward. In the numeric example given the mean position of the tip of the tail of the McEel is 0.363 m or 1.8L behind the front joint. If this were assumed as 2/6 of the wavelength, it would mean that the advance speed of the wave is 0.16 m/s. This velocity could be non-dimensionalised by multiplying it with the period of oscillation, T, and dividing it by the length of the oscillating portion of the eel. The non-dimensional advance speed of the wave would then be 2.67.

The eel therefore moves forward at about 60% of the speed at which the oscillations move backwards. This fictitious scenario therefore seems plausible, as a mechanical swimmer would be assumed at least initially to be less efficient than the optimal one and thus have a bigger gap between these two velocities than the 5/4 mentioned by Lighthill (1960) and indeed the inverse ratio of 0.8 measured in live eels by Gillis (1998).

The advance velocity of the McEel in this example is reasonably close to what is seen in nature but the amplitude of oscillation is not. In his study of American eels, (Anguilli Rostrata) Gillis (1998) found that the tip of the tail made transverse oscillations of 8% of the over-all length of the eels. Somewhat surprisingly, this was the case more or less irrespective of the swimming speed. It is therefore important to emphasise that the oscillations depicted in this chapter bear more resemblance to those performed by the McEel than those performed by live fish. This is because the less than perfect mechanical drive system of the McEel dictated substantial excitation angles in order to produce even, fluid motions.

When the excitation frequency increases compared to the velocity of the eel the acceleration vectors increases relative to the velocity vectors. This is because the acceleration vectors are independent of the advance velocity and depend rather on the frequency and amplitude of oscillation. This is an important point as it shows that it is not necessarily the Reynolds number that decides whether the inertial forces are

negligible or not. The deciding factor is the relative size of the advance velocity of the eel in comparison to its excitation frequency and amplitude.

3 Hydrodynamic models of fish-like motion

3.1 Introduction

Fishlike propulsion is seen by many as a flow problem. Only if the flow around the live or mechanical fish can be fully understood can the pressures be integrated and the total thrust computed. In chapter 2, it was shown how the velocity and acceleration vectors between an eel and a fluid that was stationary in earth coordinates behaves. In reality, the fluid surrounding the eel will not be stationary and this complicates the problem somewhat. One way to obtain a complete solution of this problem would be to integrate a solution to the Navier-Stokes equations around the eel. This could be achieved using CFD (Computational Fluid Dynamics). As the eel changes shape with time, finding a CFD solution to this problem would be difficult. In his masters thesis John Riis (2001) used CFD to gain an understanding of some of the scale effects involved in fishlike propulsion. Predicting the true forces developed by a live or a mechanical fish was outside the scope of his thesis. Biologists have, however, undertaken a two dimensional CFD analysis of self-propelled anguilliform swimming (Carling et al. 1998) but no other validation against measured data is given other than that the numeric model swam at 0.77 times the velocity of the backward travelling wave.

Solving this problem using CFD would not be ideal for various reasons. The first one is that the solution can only be validated against one real life scenario, that of the McEel. It would also require substantial resources both in terms of man-hours and computational power and would thus be unsuitable as an engineering design tool.

In order to find a solution applicable to several fishlike propulsion devices it was decided to look for the simplest numeric method that could predict the forces developed by the McEel to a level of accuracy appropriate to preliminary design.

As seen in the previous chapter a mechanical eel-like structure is essentially one or more cylinders subjected to a varying flow field in terms of both velocity and acceleration. Such a structure will be subject to various forces. These forces can be grouped into non-hydrodynamic inertial forces and hydrodynamic forces. The former will naturally be computed by applying Newton's laws of motion but it is not obvious how the latter ones should be resolved. The forces on a rigid moving underwater body is a challenging problem in itself. When the geometry of this body

changes continuously to facilitate self-propulsion, there is a need for some simplifications in order to solve the problem. In the current study, a number of simplifications are adopted in order to examine the feasibility of predicting the forces with sufficient accuracy for preliminary design using a simplified model. The various simplifications will be introduced when and where they are employed.

Historically hydrodynamic forces have often been split into drag and inertia related forces. Although the complex forces developed by a flow field around a body will not always align themselves with either relative acceleration or relative velocity, such a distinction is useful as it allows the comparison between different hydrodynamic models. The distinction between tangential and perpendicular forces gives itself from the geometry of real eels, which are long and slender bodies (Gillis 1998). A complete hydrodynamic solution to the problem of the eel should therefore deal with at least four hydrodynamic force components:

- Perpendicular drag
- Tangential drag
- Perpendicular inertia
- Tangential inertia

In addition to these four forces, there are numerous others of varying importance. Amongst these are lifting forces and forces due to vortex shedding. All of these forces are at least initially ignored as they are assumed to be of limited importance.

There are several hydrodynamic models for computing the four mentioned forces. The most notable of these methods are the before mentioned elongated body method developed by Lighthill (1960) for tangential and near tangential flow and the Morison Equation (Morison et al. 1950) for perpendicular and near perpendicular flow.

3.2 Two dimensional and three dimensional methods

One of the criteria used to assess hydrodynamic methods is whether they are two- or three-dimensional. In real life, most flow phenomena are three-dimensional but it is often useful to perform the analysis of slender bodies for one cross section of the

body and then integrate the solution over the length of the body. Both the Morison Equation and the Elongated Body Method normally does this.

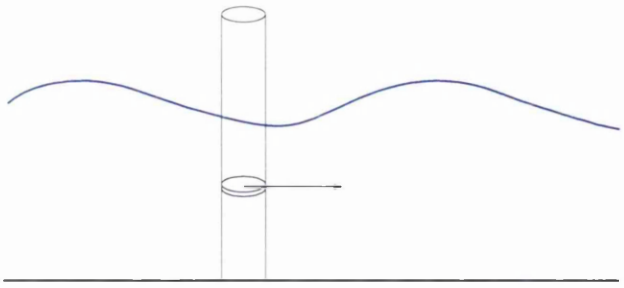

Figure 3-1: The basis for the Morison Equation

In case of the Morison Equation the flow phenomenon that it originally aimed to model is a wave flow past a vertical pile, and the total force is found by integrating the force per unit length over the length of the pile. The flow is thus three-dimensional and it is modelled as such. The force calculation is however two-dimensional. It therefore does not seem appropriate to label the original Morison Equation as either two-dimensional or three-dimensional. An exception is when the Morison Equation is verified in a U-tube, when both the flow and the force calculation is 2D.

The elongated body method was initially designed to calculate the propulsive force of anguilliform swimmers and as such, it aims to model a three-dimensional flow phenomenon.

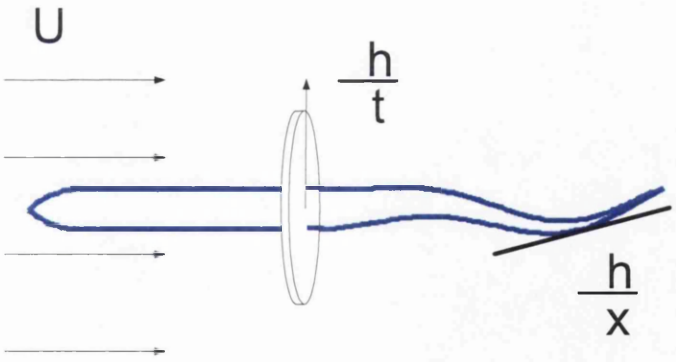

Figure 3-2: The basis for the elongated body method

To ease the computation, Lighthill assumed the fish to be stationary in a flow with velocity U. The method will be described in detail in section 3.3; however, one of the

assumptions behind the method is that the flow can be considered to be two-dimensional. In its original format the elongated body method is therefore 2D.

3.3 Elongated Body method and its expansion

Many regard the elongated body method as the standard analytical model for fishlike propulsion. This method explains how thrust is generated from added momentum acting on an undulating body as in Figure 3-2.

The method is based on slender body theory. The flow around the body is therefore assumed to be comprised of the steady flow around a similar stretched straight body and the flow due to the transverse velocity of components of the body. The theory describes how these transverse velocities will lead to an increased momentum in the fluid and thus propulsion for the swimmer. The thrust is predicted from an added mass concept and therefore only the tangential inertia forces are predicted. All other forces are assumed to be either negligible or to cancel out over a full cycle. The mean thrust is calculated from the perpendicular velocity, the span and the angle of the tip of the tail.

The Elongated Body method makes three key assumptions that cannot be fulfilled for a mechanical eel. These assumptions are:

- That the cross sectional area varies gradually in the longitudinal direction
- That the transverse velocity of the fish is small compared to its advance velocity
- That the slope that the fish makes with the x-axis is small

In order to correctly compute the flow component which is caused by the flow around the stretched straight fish the Elongated Body method requires the cross sectional area of the fish to vary gradually in the longitudinal direction. This requirement could be hard to satisfy for a mechanical eel particularly near the front end.

The Elongated Body method was intended to compute the energy used by fish swimming at a steady speed. A mechanical eel will however have to start from zero speed at which point the transverse velocity of its tail will be infinitely large

compared to its advance velocity. The mechanical eel may have trouble satisfying the second assumption even once it has reached a constant speed. This is because the relationship between the transverse velocity of the tail and the advance velocity of the eel says something about the efficiency of the swimming pattern. A real fish may be propelled quickly through the water simply by making small and slow oscillations with its tail but it is far from certain that a mechanical replica will be as efficient.

This latter point leads on to a potential desire for the mechanical eel to make large amplitude oscillations in order to generate enough thrust. If this were the case then the slope that the body makes with the x-axis would no longer be small and the third assumption could no longer be satisfied. Even if the oscillations and therefore the slope was small though it would be mathematically difficult if not intractable to use the Elongated Body method for a mechanical eel. This is because the slope of a jointed structure is not defined in the joints.

As only the movements of the tail are needed for the application of the method the problems associated with the joints were ignored and computed results from the Elongated Body method was compared to measured results from the McEel. It soon became evident however that the method was not particularly well suited to compute the forces from a mechanical eel neither in theory nor in practice.

As chapter 2 demonstrated, the segments of a mechanical eel will encounter a flow field of both velocity and acceleration at varying angles. Therefore, neither the elongated body method nor the Morison Equation is designed to calculate the forces on such a structure.

Quiggin and Carson (1994) tried to take the Elongated Body Theory and expand it to the general case to get an expression for the flow around a cylinder at any angle. In their paper, they have taken Lighthill's added momentum concept and applied it to a randomly oriented cylinder in a random flow.

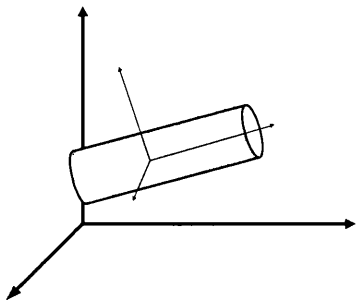

Figure 3-3: The two coordinate systems employed by Quiggin and Carson

They employ two coordinate systems in the analysis as shown in Figure 3-3. The global coordinate system is moving with the fluid and the local coordinate system is body fixed. A central concept in the derivation of this method is that the added mass for this element is a matrix of the form:

$$\mathbf{Ca} = \begin{bmatrix} ca & 0 & 0 \\ 0 & ca & 0 \\ 0 & 0 & 0 \end{bmatrix}$$

Equation 3-1

The cylinder in Figure 3-3 is considered part of a long flexible element and this means that both Equation 3-1 seems reasonable and that they avoid the problem with the slope in the joints. The cylinder would therefore have an added mass in the two transverse directions but not in the longitudinal one. For the McEel though this latter point is not necessarily the case. As the end segment of the eel has a substantial cross sectional area it would be expected to have an added mass coefficient also in the longitudinal direction.

In its original format the inertia per unit length of a cylinder subjected to a random flow is given as:

$$\begin{aligned} \mathbf{G} = {} & \mathbf{c_a \rho V}\left(\textbf{normal component of}\left(\mathbf{a_f} - \mathbf{a_v}\right)\right) \\ & + \boldsymbol{\omega}_b \times \left(\mathbf{c_a \rho V}\left(\textbf{normal component of}\left(\mathbf{v_f} - \mathbf{v_b}\right)\right)\right) \\ & + \mathbf{c_a \rho V}\left(\textbf{normal component of}\left(\mathbf{v_f} - \mathbf{v_b}\right) \times \boldsymbol{\omega}_b\right) \\ & + \mathbf{v_t}\,\partial\left(\mathbf{c_a \rho V}\left(\textbf{normal component of}\left(\mathbf{v_f} - \mathbf{v_b}\right)\right)\right)/\partial \mathbf{s} \\ & + \mathbf{c_a \rho V}\left(\textbf{normal component of}\left(\partial \mathbf{v_f}/\partial \mathbf{p}\right)\mathbf{v_b}\right) \end{aligned}$$

Equation 3-2

In Equation 3-2, V is volume of the cylinder whilst the subscript f is for the fluid and subscript b is for the body. This equation may appear to be a substantially more complex than the inertia taken from the more familiar Morison Equation. As the constants can be factorized out and the fluid can be assumed stationary Equation 3-2 reduces to:

$$\mathbf{G} = -\mathbf{c_a}\rho\mathbf{V}\left(\mathbf{a}_\perp + \omega \times \mathbf{v}_\perp + \perp(\mathbf{v} \times \omega) + \mathbf{v}_\mathbf{t}\,\partial\mathbf{v}_\perp/\partial\xi\right)$$

Equation 3-3

In this expression $\mathbf{a}_\perp$ is the normal component of the acceleration vector of the body whilst $\mathbf{v}$ is the velocity vector with subscript $\perp$ being its normal- and subscript t being its tangential-component. The symbol $\perp$ in front of the third term indicates that it is only the normal component of the vector cross product that is of interest while ω is angular velocity vector of the segment in question. The last term in the equation contains the normal velocity differentiated with respect to the segment length. This segment length is referred to as s in the original equation but as it is a local coordinate, it is referred to as ξ in Equation 3-3. In total, the inertia forces thus contain three extra terms in comparison with the more familiar Morison Equation.

Although the hydrodynamic method of Quiggin and Carson (1994) aims primarily at calculating the inertia forces of flexible risers etc. the paper, does also present a method for the calculation of the drag forces. This work is based on previous research and the drag force is divided into a normal and a tangential component:

$$F_n = \tfrac{1}{2}\rho\left|v_r\right|^2 D\left(C_d \sin^2\varphi + \pi C_n \sin\varphi\right)$$
$$F_t = \tfrac{1}{2}\rho\left|v_r\right|^2 D\left(\pi C_t \cos\varphi\right)$$

Equation 3-4

In Equation 3-4, v_r is the relative velocity between the body and the fluid or in the case of the eel the velocity of the body. The φ is the angle between the flow and the body or the angle of incidence. The equations give the force per unit length of a round cylinder of diameter D and would thus have to be modified to allow for the different wetted surface area of the eel. Cd is the drag coefficient for the calculation

of the pressure term whilst Cn is the coefficient of perpendicular skin friction. In the tangential direction, the drag is assumed to be entirely due to skin friction represented by Ct, the coefficient of tangential drag.

The method proposed by Quiggin and Carson thus allows the calculation of all the four hydrodynamic forces presented at the beginning of this chapter. No comparisons with measured data are offered though and as far as this author is aware this method for computing the hydrodynamic forces has not been used outside the OrcaFlex software package.

3.4 The Morison Equation and its expansion

The Morison Equation (Morison et al. 1950) deals specifically with flow perpendicular to the element in question. It was originally developed to estimate the forces exerted by surface waves on piles. The method calculates the forces perpendicular to the cylinder (or element) only (see Figure 3-1).

Both the horizontal velocity and the horizontal acceleration are utilized in the calculation as both perpendicular drag and perpendicular inertia forces are accounted for. The forces that the pile is subjected to are calculated for an infinitely thin disk before they are integrated over the length of the pile.

When the Morison Equation (Morison et al. 1950) was first published, it was admitted that its results were only preliminary. It was published due to there being a pressing need to calculate these types of forces. It has however found wide use since then. The original equation reads:

$$dF = \left[C_M \left(\rho \frac{\pi D^2}{4} \right) \frac{\partial u}{\partial t} \pm C_D \frac{\rho D}{2} u^2 \right] dz$$

Equation 3-5

This gives the force per unit length on the infinitely thin disk. D is the diameter of the pile whilst u is the velocity of the flow normal to the pile. The sign of the second term in the equation cannot be decided outright as the velocity term is squared. A further ambiguity is the coefficient of mass. Initially the Morison Equation was not intended to calculate forces in situations where both the fluid and the body were moving and having one term for both mass and added mass was reasonable. These days the Morison Equation is used more widely and the coefficient of added mass is

often employed. Furthermore, the initial equation applied to circular cylinders whilst today it is used for different cross sectional shapes. One therefore has to be careful when it comes to the coefficient of added mass. One common practice is to define it as the ratio of volume of water that would have to move in unison with the segments for the computed force to be the same as the one measured. An infinitely thin plate moving through the water would however have a finite volume of water moving with it and the coefficient of mass would then be infinite. In some respects, it is therefore more convenient to define it as the volume of water moving with the segment with respect to the volume of a cylinder of the same diameter as the span or height of the segment. This distance will be denoted D.

The Morison Equation would then read:

$$dF = \left[\rho \frac{\pi D^2}{4} C_a \frac{du}{dt} + \frac{1}{2} \rho \, C_D D \, |u| \, u \right] dl$$

Equation 3-6

As can be seen the normal practices is to get around the sign change on the second term by multiplying the velocity by its absolute value rather than squaring it. It has to be emphasized though that the acceleration and velocity mentioned in the Morison Equation are still those normal to the element or cylinder to which the forces apply.

Borgman (Borgman 1958) published a paper expanding upon the Morison Equation that stated that for a wave hitting a vertical pile: "The actual velocity and acceleration vectors are not necessarily horizontal and indeed achieve this condition only at the wave crest and at the trough." For the particle velocity, this is true but one must assume that Borgman was aware that the particle acceleration is 90° out of phase with this. Borgman's paper did however help introduce the idea that the acceleration and velocity vectors could be resolved in a perpendicular and a tangential component and that the first of these could be used in the Morison Equation. The Morison Equation has since found wide use even in cases of not strictly perpendicular flow.

The Morison Equation can thus be used to calculate the perpendicular drag and inertia forces experienced by a cylinder subjected to a randomly oriented flow. It is however most commonly used on perpendicular or near perpendicular flow where its

simplifications are less important. The equation has also found wide use in cases of oscillatory flow as the next chapter will demonstrate and there are numerous published experimental comparisons between the estimated data of the Morison Equation and physical measurements.

Just like the Elongated Body method, the Morison Equation was devised for a continuous body. The problem with the slope of the body in the joints of the mechanical eel is therefore still there. Unlike the Elongated Body method though, the Morison Equation is a strictly empirical method and in terms of the latter, these difficulties are therefore more akin to the lack of inclusion of end effects.

3.5 Morison's equation in oscillatory flow

One of the assumptions of the Morison equation is that a quasi-steady drag generating wake has time to build up behind the body in question. This will not necessarily be true if the motions of the body are small and fast in comparison to the size of the body itself. This was described by Keulegan and Carpenter (1958). They showed that the force could still be calculated using the Morison equation provided that the coefficients of drag (Cd) and added mass (Ca) were taken to be functions of what they termed the "period parameter", but which is now known as the Keulegan-Carpenter number. This non-dimensional number is defined as:

$$K_C = \frac{U_0 T}{D}$$

Equation 3-7

Here the U_0 would be the amplitude of the velocity of the eel in comparison to the fluid, T the period of oscillation whilst D would be the height of the eel. In the rather theoretical paper, they reported that there did not seem to be a correlation between the two coefficients and the Reynolds number. The paper does however stress that even allowing the coefficients to vary with Kc number does not ensure that the time history of the measured force throughout a cycle is modelled correctly. Only the amplitude of the measured force can be correctly predicted. The time varying difference between the computed and measured forces, they denote ΔR. This elusive time dependent discrepancy has been described by other researchers such as

Sarpkaya (1986) although no simple and reliable method appears to have been found to compute it.

For their measurements, Keulegan and Carpenter used a rectangular tank with standing waves in it and as such, the flow was 3D.

For pure sinusoidal harmonic motion, it is possible to give the Kc number in this format:

$$U_0 = \frac{2\pi A_0}{T} \Rightarrow K_C = 2\pi \frac{A_0}{D}$$

Equation 3-8

For the eel, these two definitions of the Kc number are not identical. The eel will only be in a purely sinusoidal motion when the two segments move in unison. With the introduction of a phase angle between the two, the motion of the back segment will be that of a sinusoid and one or more harmonics added to it. There is likely to be little practical difference between the two methods for calculating the Kc number but for consistency the method described in Equation 3-7 will however be used throughout.

A number of researchers have investigated the variations in Cd and Ca (or Cm) with Keulegan-Carpenter number, Reynolds number, beta number (defined as $\beta = Rn/Kc$), inclination angle, form and roughness. A good summary of many of these experiments is presented by Sundar (1998). The mentioned paper also present results for a circular inclined cylinder. Interestingly enough their method for employing the Morison equation at any angle is remarkably similar to the one represented later in this thesis but their data shows almost as much scatter for the various tests as for the various inclinations. Their tests were however performed in a wave tank, and as such, the flow will be three-dimensional.

Turgut Sarpkaya has also presented various results concerning the coefficients of drag and added mass. In 1986, he presented a paper (Sarpkaya 1986) that looked at the variation of the coefficients of drag, mass and his own total force coefficient Cf with various Kc and β numbers. The total force coefficient he defines:

$$Cf(r.m.s.) = \left(\frac{3}{8} Cd^2 + \frac{\pi^4 Cm^2}{2K^2} \right)^{\frac{1}{2}}$$

Equation 3-9

The K in Equation 3-9 is the Keulegan-Carpenter number. In the presentation of his data, the variation in the total force coefficient follows theory much better than does the values of the drag and mass coefficients. His data was all generated in a U-tube though and as such, his tests are all 2D. In his book (Sarpkaya and Isaacson 1981) though he offers a warning about the use of the Morison equation: "Morison's equation yields no information about the transverse force and seems to be adapted best to a range of Kc numbers smaller than about 8 or larger than about 25, where complex problems associated with the motion of a few vortices are not as much pronounced" (Page 123).

One of the few tests performed with a cylinder oscillating with a motion comprised of more than one sinusoid was done by Maull and Milliner (1979). They looked at the forces experienced by a cylinder as it was subjected to a sinusoidal wave and its harmonics. They found that Cd changed with a change in the relative importance of the harmonics. They also found that the force in the transverse direction or the lift could display non-harmonic nature at certain Kc numbers. Again the paper does not explain exactly how the measurements where made and it is therefore not obvious if the flow in question is 2D or 3D.

Graham (Graham 1980) has done much work on trying to predict Cd and Ca as a function of Kc. He seems to have found good agreement between a theoretical value of:

$$C_D = const.\ Kc^{-1/3}$$

Equation 3-10

and measured data for a flat plate as long as Kc<10. He also mentions previous research, which suggests $Kc^{-1/2}$ might be more appropriate but suggests that the difference between these two values of exponent would be relatively small. Using discrete vortex method and integrating over one full flow cycle, he ends up with the expression:

$$C_D = AK_c^{(3-2\lambda)/(2\lambda-1)}$$
$$C_m = C_{m0} + BK_C^{2/(2\lambda-1)}$$

Equation 3-11

In Equation 3-11, λ is dependent on the internal angle of the vortex shedding edge and would have the value of two for a flat plate or the fins of an eel. A and B are constants which, using the discrete vortex method, Graham has calculated to be 11.8 and 0.25 for a flat plate. He then estimates them to be 8.0 and 0.2 based on measurements for the same object. C_{mo} is the coefficient of mass for attached flow. Again, his tests were performed in a U-tube. Consequently, they are 2D.

In (Bearman et al. 1985) it is explained how the work of Stokes, Keulegan and Carpenter all ties in with the Morison equation. It is important to emphasize that although the Morison equation with its two terms representing the force upon a cylinder in a moving fluid is a representation of the measurable force signal, it is not a representation of what actually happens. This is explained well in this paper when the three components of the force acting on the body are presented. One component of the force is the inertial force due to accelerations of the outer flow. The second is the viscous force on the body surface, which again leads to the third component, the separation of the boundary layers leading to vortex shedding. Although it is not always clear which of these three components aligns with acceleration and which aligns with velocity squared the paper does go some way in justifying the Morison's equation separation into these two components. Either way the widespread use of the Morison's equation can be seen as an indication of the successfulness in doing so. This paper also presents tests performed in a U-tube only.

It is also stated in the same paper that sharp edged bodies, unlike their blunt counterparts, do not have a flow regime in which the flow stays attached. From this, it might be concluded that C_{mo} in Equation 3-11 should be zero for the eel. In the same paper it is also found a better agreement between measured and theoretical data for the coefficient of total force Cf(r.m.s.) than for the coefficients of mass, Cm and drag, Cd even though the definition of Cf seems to be slightly different from the one used by Sarpkaya. The paper finishes by stating that when the Kc number is larger than about 3 the drag coefficients for all sharp-edged bodies tends to be proportional to $Kc^{-1/3}$.

Prislin and others (Prislin et al. 1998) approached the problem of Cd and Ca predictions from the very practical desire to predict the behaviour of a truss spar. In their analysis, they question the validity of some of Graham's conclusions about Cd

being dependent on Kc and not Reynolds number as he kept the period of oscillation almost constant and thus locked the two in a linear relationship. The conclusion from their tests was that added mass does not vary with Reynolds number and Cd varies only insignificantly with Reynolds number above 10^5. They did however find a variation in Ca with Kc number for $0.1<Kc<1.0$, and in this range, they found that:

$$Ca = 0.642\,Kc^{\,0.0705}$$

Equation 3-12

Although this is a much narrower range than Graham's reported data there is a definite discrepancy between these two findings. This could well be due to the fact that this paper extends the Morison Equation. Instead of calculating the forces on a thin disk, the paper considers the heave plate as one element and no integration is thus performed. As such, the calculation method as well as the tests performed is 3D.

Prislin's paper is also interesting in that it uses the Morison Equation to determine the vertical loads on a floating cylinder subjected to surface waves. A floating, vertical cylinder encountering a train of surface waves will be subjected to both vertical and horizontal excitation forces very much like the McEel. The vertical forces on the floating cylinder one would assume would stem from added mass and drag effects on its bottom plate as well as skin friction terms. It is therefore interesting to note that some researchers seem to be willing to resort to the use of the Morison Equation for this vertical plate. This is particularly interesting, as the motions of this plate resemble the longitudinal accelerations experienced by the tail of the eel.

Asked in private correspondence how the vertical forces of a cylindrical buoy can be calculated Professor Nigel Barltrop (2004) explained that the added mass effects are taken account of by assuming that a volume of water similar to a semi-sphere with the same diameter as the cylinder will move in unison with the body. The drag-effects are resolved by adding a skin friction term.

3.6 Discussion

In the beginning of chapter 3, it was explained how the hydrodynamic forces encountered by the McEel can be split into a minimum of four components. It has also been shown how the normal way of calculating the perpendicular drag and inertia of the force is using the Morison Equation. Various methods of employing this equation have been explained and some of the shortcomings of it in relation to fishlike propulsion have been pointed out.

The one of the methods that the offshore industry uses to calculate tangential forces to complement the Morison Equation have also been introduced (Barltrop 2004). One potential mathematical solution to the problem of fishlike propulsion would thus be to use the Morison Equation for the perpendicular forces and an added mass coefficient and skin friction for the tangential forces.

The other possibility is a solution based on the Elongated Body method. Initially this method only considers the tangential inertia force. The expansion of the method introduced by Quiggin and Carson (1994) would however allow the calculation of all the four components of the hydrodynamic forces.

As such, two distinctly different methods for computing the forces generated by the McEel exist. Various criteria can be used to determine the most suitable method for computing the hydrodynamic forces experienced by the eel. Amongst these criteria are:

- The reliance on coefficients and where they stem from
- Consistency
- Empirical validation

This last point is by far the most important as both methods are designed to render the right result rather than model this complex flow phenomena. The Morison Equation and its additions would thus seem to be the first choice as it has been empirically validated. The normal scenario with a vertical pile hit by waves is however quite different from the scenario of the eel. Only in the case of a floating buoy does it calculate both tangential and perpendicular forces. Even then, the element considered is straight, unlike the eel, which has joints at varying angles to the general flow direction. Consequently, the empirical validation of the Morison type approach does not necessarily validate the method for the force prediction of

mechanical eels. Any empirical validation of either method for fishlike propulsion therefore has to be based on the empirical data within this study, which is too scant to render a conclusive answer.

The method suggested by Quiggin and Carson can in some ways be said to be more consistent in its attempt to compute the forces experienced by the eel than the more conventional Morison based approach. For a floating cylindrical buoy being subjected to surface waves, it may seem a fair approximation to calculate the tangential and perpendicular forces differently. The same cannot necessarily be said for a mechanical eel. The segments are shorter and experience flows of varying angle both in terms of acceleration and in terms of velocity. A uniform method for both tangential and normal forces like the one offered by Quiggin and Carson thus seems more consistent.

Whenever numeric predictions are to be compared with a limited set of measurements great caution must be shown with any method relying on too many empirical or quasi-empirical coefficients. There is always a danger that the total force predictions may come to resemble a curve fitting exercise more than a scientific comparison.

The method based on the Morison Equation utilises one coefficient for the perpendicular inertia, one for the perpendicular drag, one for the tangential inertia and one for the tangential skin friction. One might assume that at least this last coefficient might be found from published literature but again the eel is very different from other underwater bodies and this assumption is not necessarily valid. In section 2.3, it was for instance shown how sections of a stationary eel could still experience tangential velocities. Furthermore, there is anecdotal evidence that live and mechanical fish experience drag reduction whilst swimming (Gray 1936, Barrett 1996). The coefficient of tangential skin friction could therefore not necessarily be taken from published data.

The method suggested by Quiggin and Carson utilises just one coefficient for inertial forces but two for perpendicular drag and one for tangential drag. The two methods thus use the same number of coefficients. They suggest values for the three coefficients involved in the drag calculation but although these suggested values are based on previous calculations for fish and other underwater flexible bodies it is

uncertain how applicable they are to the computation of forces experienced by a jointed structure.

It is to this author not obvious which of these two approaches that is best suited to predict the forces generated by the eel. Neither is the empirical data in this thesis extensive enough to give a conclusive answer. Both methods are therefore employed and the result presented as being at least an indication of the merits of doing it either way.

4 Mathematical implementation

4.1 Introduction

The challenge of any mathematical modelling or representation is that it has to be complete enough to give meaningful results without being so complex as to be impossible to solve. In this chapter, the implementation of a mathematical modelling of a jointed eel-like structure is developed starting from a very basic model. The overall goal is to estimate the thrust developed by such a device in a range of swimming patterns, and hence calculate key design parameters such as speed, power, torque and efficiency. However, the simplest models ignoring hydrodynamic effects were also used for estimating the torque required in each joint in order to size the motors. The moment computed from the more advanced models were used to calculate the power required by the eel.

Some numerical models, which were examined but in the end proved of little relevance, are presented Appendix B.

4.2 Notation

Before the different mathematical models are presented it is useful to introduce the notation used, as this is common to all of them. A global and a local coordinate system will be used. By global in this context is understood a system, which is global for the eel itself though moving with it as the eel swims forward. A local coordinate system will be assigned to each straight segment. This local coordinate system will be presented when it is needed for the more advanced models.

The global system has its origin in the first joint and the eel is assumed to be swimming from right to left in this system. The origin is where the head segment is connected to the first moveable segment. As the eel only flexes in one plane the global coordinate system will be defined in terms of two orthogonal coordinates. The origin is therefore denoted (X_1, Y_1). An increasing number from this point can now identify the nodal points as well as the segments such that the node point (Xi, Yi) corresponds to the leftmost endpoint of the i-th segment.

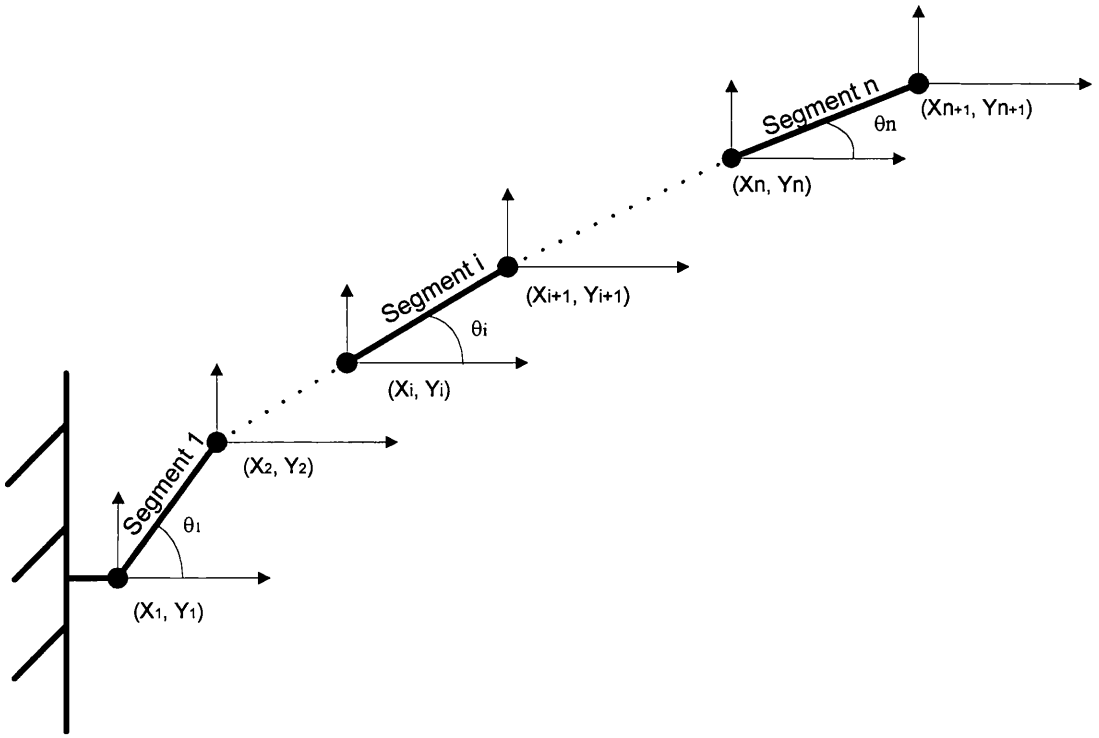

Figure 4-1: The global coordinate system of an n segment eel.

The angles that each segment makes with the global system and the length of each segment can then be denoted as θi and Li respectively, where i denotes the segment number.

The velocity of the nodal points in the x- and y-direction are denoted $\dot{X}$ and $\dot{Y}$. Similarly the acceleration of each nodal point is denoted $\ddot{X}$ and $\ddot{Y}$. The motion of the entire system is now defined.

4.3 Inertial force, lumped mass model

The simplest model for calculation of forces and moments on a jointed eel is a lumped mass model. This model ignores all hydrodynamic forces and assumes that all mass is lumped in the centre of each segment. The error of the first approximation will reduce towards zero as the segment lengths tend to zero.

The position of any nodal point can now be given in terms of the nodal point to its left and the angle of the segment to its left:

$$X_i = X_{i-1} + L_{i-1}\cos\theta_{i-1}$$
$$Y_i = Y_{i-1} + L_{i-1}\sin\theta_{i-1}$$

Equation 4-1

These displacements can in turn be differentiated with respect to time to give both velocity and acceleration of the nodal points. The velocities are:

$$\dot{X}_i = \dot{X}_{i-1} - \dot{\theta}_{i-1}L_{i-1}\sin\theta_{i-1}$$
$$\dot{Y}_i = \dot{Y}_{i-1} + \dot{\theta}_{i-1}L_{i-1}\cos\theta_{i-1}$$

Equation 4-2

Similarly the accelerations of the endpoints would be:

$$\ddot{X}_i = \ddot{X}_{i-1} - \dot{\theta}_{i-1}^{\,2}L_{i-1}\cos\theta_{i-1} - \ddot{\theta}_{i-1}L_{i-1}\sin\theta_{i-1}$$
$$\ddot{Y}_i = \ddot{Y}_{i-1} - \dot{\theta}_{i-1}^{\,2}L_{i-1}\sin\theta_{i-1} + \ddot{\theta}_{i-1}L_{i-1}\cos\theta_{i-1}$$

Equation 4-3

There is no drag when calculating the inertia forces. Only the accelerations are therefore of interest. The acceleration of each element will be the average of the acceleration of its endpoints, as the elements are assumed rigid. The forces on the i-th element are therefore:

$$F_{X,i} = \frac{m_i}{2}\left[2\ddot{X}_{i-1} - \dot{\theta}_{i-1}^{\,2}L_{i-1}\cos\theta_{i-1} - \ddot{\theta}_{i-1}L_{i-1}\sin\theta_{i-1}\right]$$
$$F_{Y,i} = \frac{m_i}{2}\left[2\ddot{Y}_{i-1} - \dot{\theta}_{i-1}^{\,2}L_{i-1}\sin\theta_{i-1} + \ddot{\theta}_{i-1}L_{i-1}\cos\theta_{i-1}\right]$$

Equation 4-4

Note that these forces are those generated by the movement of the segments. Their numbering therefore corresponds to that of the segments NOT that of the endpoints. Lower case m refers to the mass of the segment.

A simpler form of these equations would of course be:

$$F_{X,i} = m_i\left(\frac{1}{2}\ddot{X}_i + \frac{1}{2}\ddot{X}_{i+1}\right)$$
$$F_{Y,i} = m_i\left(\frac{1}{2}\ddot{Y}_i + \frac{1}{2}\ddot{Y}_{i+1}\right)$$

Equation 4-5

This is not surprising. The force developed by moving a segment with its mass concentrated at its midpoint is equal to the mass of the segment multiplied by half the sum of the accelerations of its endpoints.

By adding up the forces, acting on each element the instantaneous thrust can be calculated.

$$Thrust_{inst} = \sum_{i=1}^{n} F_{X,i}$$

Equation 4-6

The average of the instantaneous thrust over one full cycle should then be the thrust in standard naval architecture terms. This average thrust would however obviously be zero for this simple model.

Once the forces have been determined, the moment in the backmost joint can be computed:

$$M_n = F_{Y,n}\frac{L_n}{2}\cos(\theta_n) - F_{X,n}\frac{L_n}{2}\sin(\theta_n)$$

Equation 4-7

Capital M denotes the moment in the joint. Note that with this notation n corresponds to the last *joint* in an n-segment eel. The last nodal point, which would be the tip of the tail, would be n+1.

Since the mass is assumed at midpoint the lever arm is half-length multiplied by cosine and sine of the angle that the element makes with the coordinate system for the forces in the Y- and X- direction. The negative sign stems from the fact that the moment from a positive force along the X-axis yields a clockwise moment.

It must be emphasized that this moment is the only one that can be calculated on its own. To work out the moments in the other joints one must start with this and work towards the head. The expression for the moment in the i-th node is:

$$M_i = F_{Y,i}\frac{L_i}{2}\cos(\theta_i) - F_{X,i}\frac{L_i}{2}\sin(\theta_i) + M_{i+1} + F_{Y,i+1}L_i\cos(\theta_i) - F_{X,i+1}L_i\sin(\theta_i)$$

Equation 4-8

A free-body diagram may help to explain where all the terms in Equation 4-8 come from:

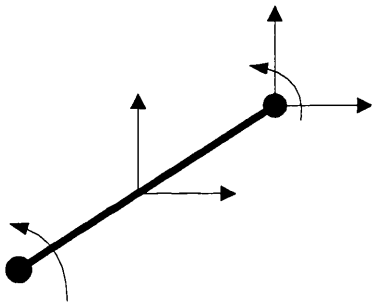

Figure 4-2: The moments in each joint

The first two terms in Equation 4-8 can be recognized from the calculation of the moment in the last joint. In addition to this, the moment in all the other joints are dependent on the moment in the joint to the right of them but also on the forces exerted on the element to its right times the length of itself.

This lumped mass model can thus be used to predict the moments required to move an n-segment eel. In this most basic form, it does not incorporate any hydrodynamic forces. When a mechanical eel moves under water there will clearly be hydrodynamic forces generated. To account for this in the simplest possible way an added mass of fluid assumed to move in unison with the elements can be employed. This is clearly not correct, as the eel would be streamlined in one direction and not the other. Simply multiplying the true mass of the elements with some (1+Ca) factor should however better the approximation of the forces and moments involved. It is important to emphasise that this crude approximation is different from the added inertia employed by the Morison Equation as the Morison Equation only deals with the perpendicular accelerations for its added mass term.

It must also be emphasised that the lumped mass approximation is a reasonable one for the numerical solution of a flexible problem. For such a scenario, the segment length can easily be reduced to a level where the solution converges towards the correct answer. In this particular case, however the segment length is fixed, as the physical model itself is discretised.

4.4 Inertial force, distributed mass model

The total mass of each of the segments of the eel clearly will not be located in its centre. A natural improvement on the model would therefore be to distribute the mass evenly along the length of the segments. For a real mechanical eel the mass probably would not be truly evenly distributed either but it can reasonably be assumed to give a better approximation.

To facilitate the distribution of mass a local coordinate system for each of the segments is required:

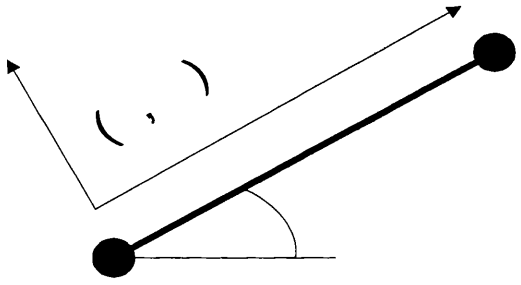

Figure 4-3: The local coordinate system

The two end-points are the nodal points of the segment. The coordinate ξ runs along the segment starting from its leftmost nodal point.

The calculation of the motions of the nodal points themselves are unaffected by the switch to a distributed mass system and it is only the forces and moments that will differ. The forces on an infinitely short element of the i-th segment would be:

$$dF_X = \frac{m_i}{L_i}\left(\ddot{X}_i + \frac{\ddot{X}_{i+1} - \ddot{X}_i}{L_i}\xi\right) d\xi$$
$$dF_Y = \frac{m_i}{L_i}\left(\ddot{Y}_i + \frac{\ddot{Y}_{i+1} - \ddot{Y}_i}{L_i}\xi\right) d\xi$$

Equation 4-9

These forces are in the global axis system. Integrating these forces along the length of each segment will give the total force for the i-th segment:

$$F_{X,i} = \int_0^{L_i} dF_X = m_i\left(\frac{1}{2}\ddot{X}_i + \frac{1}{2}\ddot{X}_{i+1}\right)$$
$$F_{Y,i} = \int_0^{L_i} dF_Y = m_i\left(\frac{1}{2}\ddot{Y}_i + \frac{1}{2}\ddot{Y}_{i+1}\right)$$

Equation 4-10

This result should not be surprising. When the mass of each segment is evenly distributed, the force of each segment in the x- and y-direction is the same as it is for the lumped mass case. All these elemental forces though do have different lever arms and the moment in the joints should therefore not be the same:

$$dM_X = -\frac{m_i}{L_i}\left(\ddot{X}_i + \frac{\ddot{X}_{i+1} - \ddot{X}_i}{L_i}\xi\right)\xi \sin\theta_i \, d\xi$$
$$dM_Y = \frac{m_i}{L_i}\left(\ddot{Y}_i + \frac{\ddot{Y}_{i+1} - \ddot{Y}_i}{L_i}\xi\right)\xi \cos\theta_i \, d\xi$$

Equation 4-11

It is important to emphasize that these elemental moments are those due to the forces in the X- and Y-direction. The negative sign in the moment due to the force in the X-direction is due to the fact that a positive force would generate a clockwise moment.

The moment in the backmost joint can now be calculated:

$$M_n = \int_0^{L_N} (dMy + dMx)$$
$$= \left(\left(\frac{1}{6}\ddot{Y}_n + \frac{1}{3}\ddot{Y}_{n+1} \right) \cos\theta_n - \left(\frac{1}{6}\ddot{X}_n + \frac{1}{3}\ddot{X}_{n+1} \right) \sin\theta_n \right) m_n L_n$$

Equation 4-12

As is the case for the lumped mass model the moments have to be resolved from the tail end. The moment in the i-th joint would be:

$$M_i = \left(\left(\frac{1}{6}\ddot{Y}_i + \frac{1}{3}\ddot{Y}_{i+1} \right) \cos\theta_i - \left(\frac{1}{6}\ddot{X}_i + \frac{1}{3}\ddot{X}_{i+1} \right) \sin\theta_i \right) m_i L_i + M_{i+1}$$

$$+ F_{Y,i+1} L_i \cos(\theta_i) - F_{X,i+1} L_i \sin(\theta_i)$$

Equation 4-13

The distributed mass model is closer to the real scenario than the lumped mass model but it still does not take into account the hydrodynamic forces. In essence it solves the problem of a mechanical eel swinging from side to side in a vacuum. As such it can be useful for verification purposes based on measurements in air, in which fluid forces can be assumed to be negligible in comparison to the real inertial forces.

4.5 Lumped mass Morison Equation

The Morison Equation deals with two sets of hydrodynamic forces, one in phase with normal acceleration, and the other in phase with normal velocity. The force calculated previously, the one due to the real inertia of the segment is also present. It cannot easily be combined with the hydrodynamic inertia force as it is in line with the acceleration, be it normal to the segment or in any other direction. A solution involving the Morison Equation should therefore contain three different forces. In the simplest version, consistent with the lumped mass approximation for the inertial forces, it can be assumed that the velocities may be calculated at the segment midpoints.

The velocities and accelerations used for the Morison forces can now be calculated. The eel is assumed to be swimming through a stationary fluid. In the case when the forward speed of the eel is zero the velocities and accelerations needed for the Morison equation will be those that the centre of each segment makes with the global coordinate system. When the eel starts to swim forward this can be accounted for by giving (X_1, Y_1) a forward velocity component. In local coordinates the velocity and acceleration with respect to the global coordinate system are:

$$v_i = \frac{1}{2}(\dot{\eta}_i + \dot{\eta}_{i+1})$$
$$a_i = \frac{1}{2}(\ddot{\eta}_i + \ddot{\eta}_{i+1})$$

Equation 4-14

The lower case η is the local transverse coordinate of the endpoints of each segment. The hydrodynamic forces on the eel can now be estimated:

$$F_i = \left[\rho \frac{\pi D_i^2}{8} C_{a_i} (\ddot{\eta}_i + \ddot{\eta}_{i+1}) + \frac{1}{4} \rho \, C_{D_i} D_i \left| (\dot{\eta}_i + \dot{\eta}_{i+1}) \right| \, (\dot{\eta}_i + \dot{\eta}_{i+1}) \right] L_i$$

Equation 4-15

It has to be emphasized that the coefficients of inertia and drag would not necessarily be uniform through out the eel and they are thus denoted Ca_i and Cd_i respectively.

Giving the hydrodynamic forces in local coordinates is not very useful. The local coordinate systems would be different for each segment and the forces can therefore not be added up. Instead, the calculation is performed using the global coordinate system. For this purpose, a unit normal vector is defined as:

$$\vec{\mathbf{N}}_i = \begin{bmatrix} -\sin\theta_i \\ \cos\theta_i \end{bmatrix}$$

Equation 4-16

This would be with the normal unit vector for the i-th segment pointing upwards. The result of the calculation would be the unchanged if the normal unit vector chosen pointed downwards.

The normal velocity of the midpoint of this i-th segment can now be calculated:

$$\vec{V}_{\perp,i} = \frac{1}{2}\left[\begin{bmatrix} \dot{X}_i + \dot{X}_{i+1} \\ \dot{Y}_i + \dot{Y}_{i+1} \end{bmatrix} \bullet \vec{N}_i \right] \vec{N}_i$$

Equation 4-17

In this expression, the scalar product of the velocity of the midpoint of each segment and the normal vector gives the magnitude of the velocity along the normal vector. This magnitude is then multiplied with the normal unity vector to render the normal velocity vector.

Similarly, the normal acceleration of the midpoint can be found:

$$\vec{A}_{\perp,i} = \frac{1}{2}\left[\begin{bmatrix} \ddot{X}_i + \ddot{X}_{i+1} \\ \ddot{Y}_i + \ddot{Y}_{i+1} \end{bmatrix} \bullet \vec{N}_i \right] \vec{N}_i$$

Equation 4-18

Written out in the X- and Y-directions these expressions would read:

$$\begin{aligned}
\dot{X}_{\perp,i} &= \frac{1}{2}\left[(\dot{X}_i + \dot{X}_{i+1})(-\sin\theta_i) + (\dot{Y}_i + \dot{Y}_{i+1})(\cos\theta_i)\right](-\sin\theta_i) \\
\dot{Y}_{\perp,i} &= \frac{1}{2}\left[(\dot{X}_i + \dot{X}_{i+1})(-\sin\theta_i) + (\dot{Y}_i + \dot{Y}_{i+1})(\cos\theta_i)\right](\cos\theta_i) \\
\ddot{X}_{\perp,i} &= \frac{1}{2}\left[(\ddot{X}_i + \ddot{X}_{i+1})(-\sin\theta_i) + (\ddot{Y}_i + \ddot{Y}_{i+1})(\cos\theta_i)\right](-\sin\theta_i) \\
\ddot{Y}_{\perp,i} &= \frac{1}{2}\left[(\ddot{X}_i + \ddot{X}_{i+1})(-\sin\theta_i) + (\ddot{Y}_i + \ddot{Y}_{i+1})(\cos\theta_i)\right](\cos\theta_i)
\end{aligned}$$

Equation 4-19

It has to be emphasized that the velocities and accelerations in Equation 4-19 are the components of the velocities and accelerations of the mid point of the segment in question that is normal to the segment itself. They thus differ from the other velocities and accelerations written with capital letters both in the fact that they refer

to the mid point rather than to the nodal points, and that they are resolved along the normal vector. This latter point is distinguished by the ⊥ symbol in their subscript.

As these expressions are for the normal component of the motions, they can be substituted directly into the Morison Equation. The hydrodynamic inertia forces according to a lumped mass Morison model would then be:

$$F_{\ddot{X},i} = \frac{\pi D_i^2}{8} C_{a_i} \rho L_i \left[(\ddot{X}_i + \ddot{X}_{i+1})(-\sin\theta_i) + (\ddot{Y}_i + \ddot{Y}_{i+1})(\cos\theta_i) \right](-\sin\theta_i)$$

$$F_{\ddot{Y},i} = \frac{\pi D_i^2}{8} C_{a_i} \rho L_i \left[(\ddot{X}_i + \ddot{X}_{i+1})(-\sin\theta_i) + (\ddot{Y}_i + \ddot{Y}_{i+1})(\cos\theta_i) \right](\cos\theta_i)$$

Equation 4-20

In calculating the hydrodynamic drag forces, it is beneficial to start by calculating the absolute value of the normal velocity vector:

$$\vec{\mathbf{V}}_{\perp,i} = \begin{bmatrix} \dot{X}_{\perp,i} \\ \dot{Y}_{\perp,i} \end{bmatrix}$$

$$\left| \vec{\mathbf{V}}_{\perp,i} \right| = \sqrt{\dot{X}_{\perp,i}^{\ 2} + \dot{Y}_{\perp,i}^{\ 2}}$$

Equation 4-21

As the normal velocity vector of the midpoint can be defined in its X- and Y-components, the magnitude of it can be found in the usual manner. The drag force can now be calculated:

$$F_{\dot{X},i} = D_i C_{D_i} \rho L_i \left(\sqrt{\dot{X}_{\perp,i}^{\ 2} + \dot{Y}_{\perp,i}^{\ 2}} \right) \dot{X}_{\perp,i}$$

$$F_{\dot{Y},i} = D_i C_{D_i} \rho L_i \left(\sqrt{\dot{X}_{\perp,i}^{\ 2} + \dot{Y}_{\perp,i}^{\ 2}} \right) \dot{Y}_{\perp,i}$$

Equation 4-22

To find the total force for each segment in the x- and y-direction the three forces simply have to be added together. This will be the addition of Equation 4-5, Equation 4-22 and Equation 4-20:

$$F_{\Sigma,X,i} = F_{X,i} + F_{\dot{X},i} + F_{\ddot{X},i}$$
$$F_{\Sigma,Y,i} = F_{Y,i} + F_{\dot{Y},i} + F_{\ddot{Y},i}$$

Equation 4-23

To find the overall forces on the eel the forces for each segment has to be added up:

$$F_X = \sum_{i=1}^{n} F_{\Sigma,X,i}$$
$$F_Y = \sum_{i=1}^{n} F_{\Sigma,Y,i}$$

Equation 4-24

To find the moments in the two joints the forces on each segment from Equation 4-23 must be multiplied with the correct lever:

$$M_n = F_{\Sigma,Y,n}\frac{L_n}{2}\cos(\theta_n) - F_{\Sigma,X,n}\frac{L_n}{2}\sin(\theta_n)$$

Equation 4-25

This again is the moment in the n-th joint. The moment in the i-th joint can be expressed as:

$$M_i = F_{\Sigma,Y,i}\frac{L_i}{2}\cos(\theta_i) - F_{\Sigma,X,i}\frac{L_i}{2}\sin(\theta_i) + M_{i+1}$$
$$+F_{\Sigma,Y,i+1}L_i\cos(\theta_i) - F_{\Sigma,X,i+1}L_i\sin(\theta_i)$$

Equation 4-26

These last two equations are quite similar to Equation 4-7 and Equation 4-8. This is to be expected, as it is only the method of calculation of the forces that varies between the two equations.

4.6 The distributed Morison model

The previous model assumed that all points along each segment move at uniform velocity and acceleration. This is clearly not true and since the drag-force is dependent on the square of the velocity, it leads to both an incorrect force and moment being calculated. To better these estimates the correct velocities and accelerations for each part of each segment should be used. It can be argued that this is consistent with the assumptions of the distributed mass model in section 4.4.

This can be done using either analytical or numeric integration. Although the analytical solution would produce the most accurate result, it has certain important limitations. Firstly, it is not as flexible when it comes to altering the physical set up of the eel and it is not as suitable for computer calculation. The numeric solution should also render a highly accurate result if each segment is sufficiently subdivided. The numeric solution has therefore been chosen for the calculation of the distributed Morison model.

Each segment therefore has to be separated into k parts.

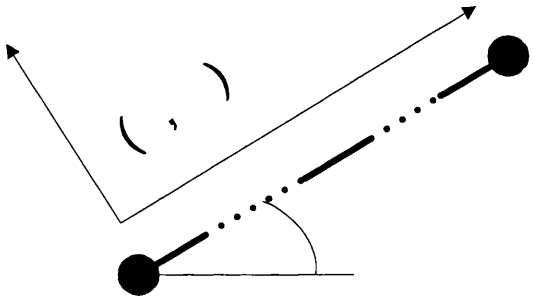

Figure 4-4: The parts of each segment

The parts of each segment are termed elements. Each element would be assumed moving in unison and it is therefore the position, velocity and acceleration of the mid-point of each element that is of interest. These points along each segment are denoted in lower case. This means that $(x_{j,i}, y_{j,i})$ is the midpoint of the j-th element of the i-th segment. The positions of these midpoints in global coordinates are:

$$x_{j,i} = X_i + \frac{X_{i-1} - X_i}{2k} + (j-1)\frac{X_{i-1} - X_i}{k}$$
$$y_{j,i} = Y_i + \frac{Y_{i-1} - Y_i}{2k} + (j-1)\frac{Y_{i-1} - Y_i}{k}$$

Equation 4-27

The position of the midpoint of the elements is given by the coordinate of the segment's leftmost endpoint and half the displacement of one element and the displacement of one element multiplied by its element number minus one. As this expression is differentiable finding the velocities and accelerations of the midpoints is trivial:

$$\dot{x}_{j,i} = \dot{X}_i + \frac{\dot{X}_{i-1} - \dot{X}_i}{2k} + (j-1)\frac{\dot{X}_{i-1} - \dot{X}_i}{k}$$
$$\dot{y}_{j,i} = \dot{Y}_i + \frac{\dot{Y}_{i-1} - \dot{Y}_i}{2k} + (j-1)\frac{\dot{Y}_{i-1} - \dot{Y}_i}{k}$$

Equation 4-28

Similarly the accelerations:

$$\ddot{x}_{j,i} = \ddot{X}_i + \frac{\ddot{X}_{i-1} - \ddot{X}_i}{2k} + (j-1)\frac{\ddot{X}_{i-1} - \ddot{X}_i}{k}$$
$$\ddot{y}_{j,i} = \ddot{Y}_i + \frac{\ddot{Y}_{i-1} - \ddot{Y}_i}{2k} + (j-1)\frac{\ddot{Y}_{i-1} - \ddot{Y}_i}{k}$$

Equation 4-29

Before the computation of the hydrodynamic forces is attempted it is important to emphasize that the real inertia forces of the eel itself can still be computed using Equation 4-10. It is however beneficial to recalculate these forces for each of the elements rather than use the result calculated for the segment as a whole. This will be done when computing the total force on each element in Equation 4-35.

In order to calculate the hydrodynamic forces the normal vector of Equation 4-16 is used. The normal velocity of the midpoint of each element will be:

$$\vec{v}_{N,j,i} = \left[\begin{bmatrix} \dot{x}_{j,i} \\ \dot{y}_{j,i} \end{bmatrix} \bullet \vec{N}_i \right] \vec{N}_i$$

Equation 4-30

The vector is given in lower case to differentiate it from the normal velocities of the midpoints of the segments. Note that the angle is constant throughout the segment and the normal unity vector therefore is the same for all elements of each segment.

Similarly, the normal acceleration of the elements midpoints can be found:

$$\vec{a}_{N,j,i} = \left[\begin{bmatrix} \ddot{x}_{j,i} \\ \ddot{y}_{j,i} \end{bmatrix} \bullet \vec{N}_i \right] \vec{N}_i$$

Equation 4-31

Written out in the x- and y-directions these expressions would read:

$$\begin{aligned}
\dot{x}_{\perp,j,i} &= \left[\dot{x}_{j,i}(-\sin\theta_i) + \dot{y}_{j,i}(\cos\theta_i) \right](-\sin\theta_i) \\
\dot{y}_{\perp,j,i} &= \left[\dot{x}_{j,i}(-\sin\theta_i) + \dot{y}_{j,i}(\cos\theta_i) \right](\cos\theta_i) \\
\ddot{x}_{\perp,j,i} &= \left[\ddot{x}_{j,i}(-\sin\theta_i) + \ddot{y}_{j,i}(\cos\theta_i) \right](-\sin\theta_i) \\
\ddot{y}_{\perp,j,i} &= \left[\ddot{x}_{j,i}(-\sin\theta_i) + \ddot{y}_{j,i}(\cos\theta_i) \right](\cos\theta_i)
\end{aligned}$$

Equation 4-32

As these expressions again are for the normal part of the motions, they can be substituted directly into the Morison Equation.

The hydrodynamic inertia forces of each element along the segment according to a discretely distributed Morison model would then be:

$$\begin{aligned}
f_{\ddot{x},j,i} &= \frac{\pi D_{j,i}^{\ 2}}{8} C_{a_{j,i}} \rho \frac{L_i}{k} \left[\ddot{x}_{j,i}(-\sin\theta_i) + \ddot{y}_{j,i}(\cos\theta_i) \right](-\sin\theta_i) \\
f_{\ddot{y},j,i} &= \frac{\pi D_{j,i}^{\ 2}}{8} C_{a_{j,i}} \rho \frac{L_i}{k} \left[\ddot{x}_{j,i}(-\sin\theta_i) + \ddot{y}_{j,i}(\cos\theta_i) \right](\cos\theta_i)
\end{aligned}$$

Equation 4-33

Similarly, the drag force for each element can be calculated with the help of Equation 4-21:

$$f_{\dot{x},j,i} = D_{j,i} C_{D_{j,i}} \rho \frac{L_i}{k} \left(\sqrt{\dot{x}_{\perp,j,i}^{\ 2} + \dot{y}_{\perp,j,i}^{\ 2}} \right) \dot{x}_{\perp,j,i}$$
$$f_{\dot{y},j,i} = D_{j,i} C_{D_{j,i}} \rho \frac{L_i}{k} \left(\sqrt{\dot{x}_{\perp,j,i}^{\ 2} + \dot{y}_{\perp,j,i}^{\ 2}} \right) \dot{y}_{\perp,j,i}$$

Equation 4-34

Again, these forces are given in lower case, as they are for a single element of a single segment only. Asides from that this equation is very similar to Equation 4-22, as would be expected.

The overall forces acting on this individual element can now be computed:

$$f_{\Sigma,x,j,i} = \frac{m_i}{k} \ddot{x}_{j,i} + f_{\dot{x},j,i} + f_{\dot{x},j,i}$$
$$f_{\Sigma,y,j,i} = \frac{m_i}{k} \ddot{y}_{j,i} + f_{\ddot{y},j,i} + f_{\dot{y},j,i}$$

Equation 4-35

The real mass is assumed uniformly distributed throughout the segment and the real inertia forces are therefore computed from the real mass divided by the number of elements multiplied by the acceleration. This acceleration would be taken from Equation 4-29.

The instantaneous thrust can now be calculated:

$$Thrust_{inst} = \sum_{i=1}^{n} \sum_{j=1}^{k} f_{\Sigma,x,j,i}$$

Equation 4-36

Again, this instantaneous thrust would have to be averaged over a whole cycle to give the more conventional figure for thrust.

The moment in the backmost joint can be found by multiplying the forces of each element with their corresponding lever arm:

$$M_n = \sum_{j=1}^{k}\left(f_{\Sigma,y,j,n}\left(x_{j,n} - X_n\right) - f_{\Sigma,x,j,n}\left(y_{j,n} - Y_n\right)\right)$$

Equation 4-37

This moment is again required to calculate all the other moments, as they are dependent on the moment to the right of them.

$$M_i = \sum_{j=1}^{k}\left(f_{\Sigma,y,j,i}\left(x_{j,i} - X_i\right) - f_{\Sigma,x,j,i}\left(y_{j,i} - X_i\right)\right) + M_{i+1}$$
$$+\sum_{j=1}^{k}(f_{\Sigma,y,j,i+1})L_i\cos(\theta_i) - \sum_{j=1}^{k}(f_{\Sigma,x,j,i+1})L_i\sin(\theta_i)$$

Equation 4-38

This moment in the i-th joint consists of the moment the segment generates itself, the moment in the joint to its right and the moment from the resultant forces in the joint to its right.

4.7 Comparisons

A comparison of the predicted moment in the first joint for the McEel as well as the over all predicted thrust for the 30-40-60 scenario is presented here. This not intended as an exhaustive comparison but rather as an indication of how the predictions from the different numerical methods vary for a device like the McEel. The eel is therefore assumed to have two moving segments and the values used for this comparison are:

Ca	1.0
Cd	1.2
mass (per seg.)	2 kg
Length (of seg.)	0.2 m
Breadth (of seg.)	0.1 m
Depth	0.2 m
centroid	0.1 m

Table 4.7-1: The basis for the comparison

The predicted moment in the front joint is presented in Figure 4-5.

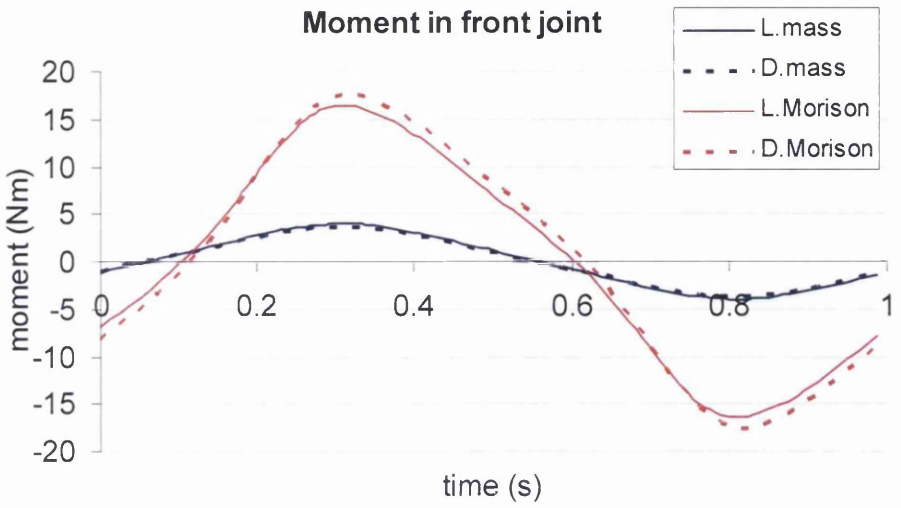

Figure 4-5: Comparison of the predicted moment in the front joint

In this graph, the moment in the front joint required to oscillate the McEel in a 30-40-60 pattern at 1 Hz at zero forward speed is predicted using the four different theoretical models. As can be seen the methods including hydrodynamic forces are substantially larger than the ones limited to solid inertia effects. This is not surprising as the tested eel has a substantial projected area compared to its mass. It can also be seen that the effect of computing distributed forces as opposed to lumped ones has a limited impact in this case.

The similarly predicted over-all longitudinal forces would be:

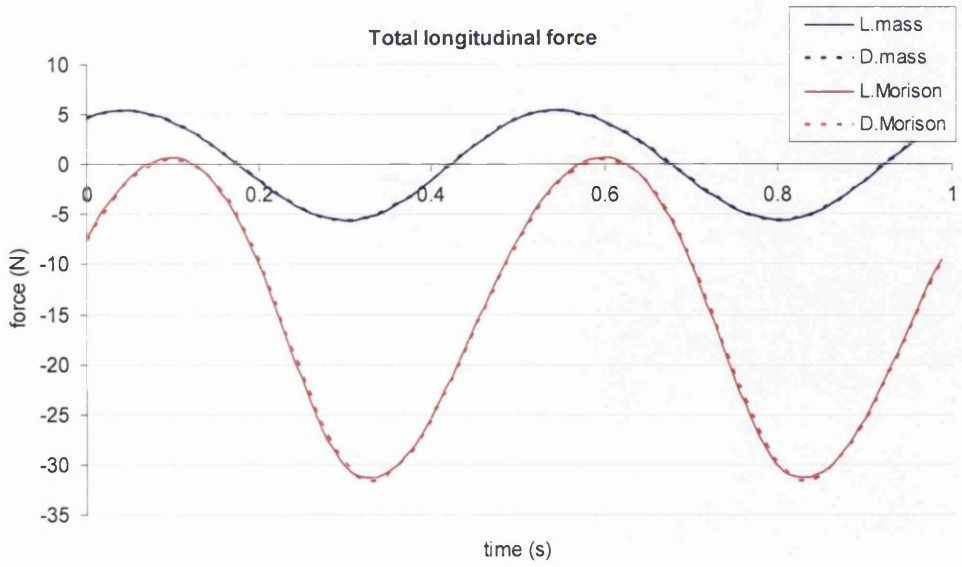

Figure 4-6: Comparison of the predicted longitudinal force

In this graph, the two predicted forces containing only real inertia effects are identical, as one would expect. The two forces including hydrodynamic effects are also virtually identical. This could reasonably be expected with an eel with such short segments.

It should also be emphasised that the models with only real inertia forces predict zero mean forward thrust as one would expect. The models based on the Morison Equation do however predict a mean forward thrust. This is reassuring and can be seen as an indication that the Morison Equation can be used as the basis for computing fishlike propulsion.

It is therefore of interest to see which of the three force components it is that generates the forward thrust:

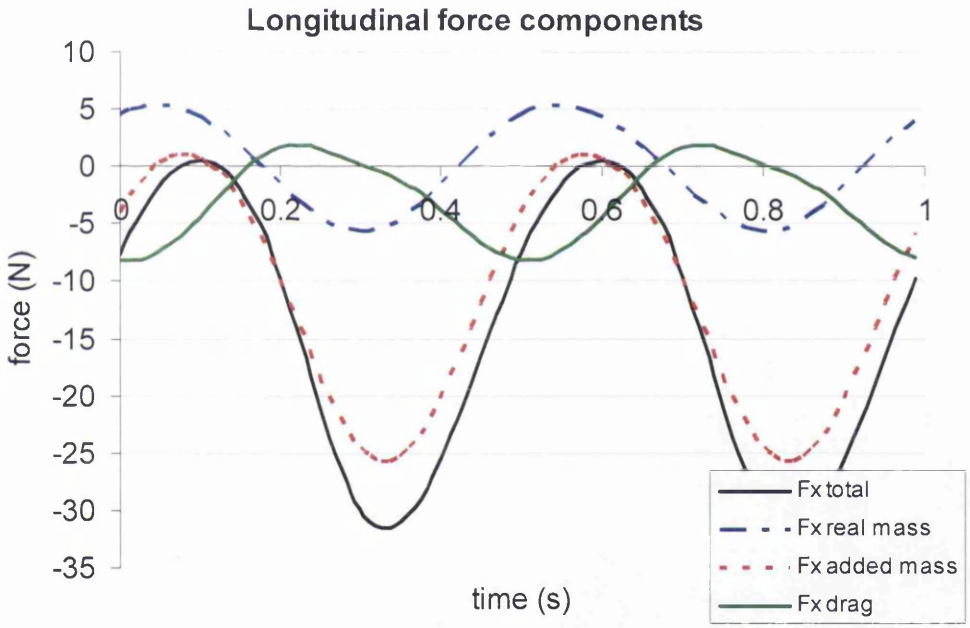

Figure 4-7: The components of the longitudinal force

In Figure 4-7, it can be seen that the total forward force resembles the force coming from the added mass forces. The real mass inertia effects and the drag forces seem to modify the force signal from added mass effects rather than alter it completely.

A comparison of the mean values of the various components does however reveal some important points:

Component	Mean force (N)
Real mass	0.0
Added mass	-11.6
Drag	-2.9

Total	-14.5

Table 4.7-2: The time dependent average of the force components

Although the drag force has a small amplitude its mean is substantial. This example therefore indicates that both inertia- and drag-effects need to be taken account of when the mean forward thrust of a fishlike propulsion device is to be calculated.

5 Model design

5.1 Introduction

The only way to establish which if any of the numeric models are up to the task of predicting the forces on an eel-like structure is to compare their predictions with measured data. Measuring the forces on an eel-like structure is however far from a trivial endeavour. To begin with, a real eel, like the AUV that tries to imitate it, is a free-swimming body. Therefore, the forces between the body and the water cannot be easily measured. In addition, it would be very complex to make a truly autonomous vehicle. Even just keeping the eel at a constant depth below the surface cannot be achieved without some sort of control system. In addition, scientific accuracy on any measurement of a mechanical fish can be better achieved if one is certain that it swims in a straight line. These factors quickly led to the decision of attaching the mechanical eel to the end of a sting and towing it in a towing tank.

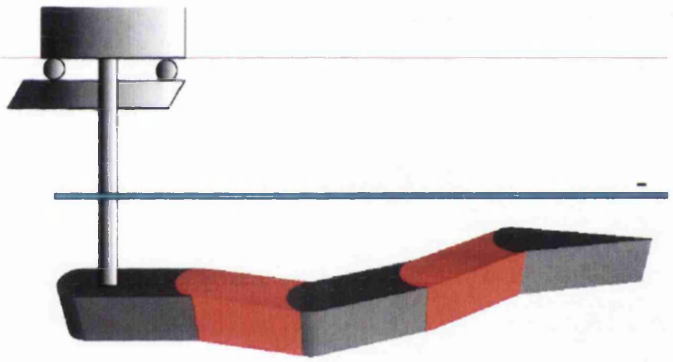

Figure 5-1: A jointed structure on a sting

5.2 The first plan

In order to be able to optimize the motions of the eel each joint has to be able to operate independently. Initially the plan was to achieve this by having one motor in each segment and a wire and worm wheel system to pull the joint from side to side. To make it all waterproof the plan was to lead the wires through flexible rubber hoses making a watertight connection from one carriage to the next.

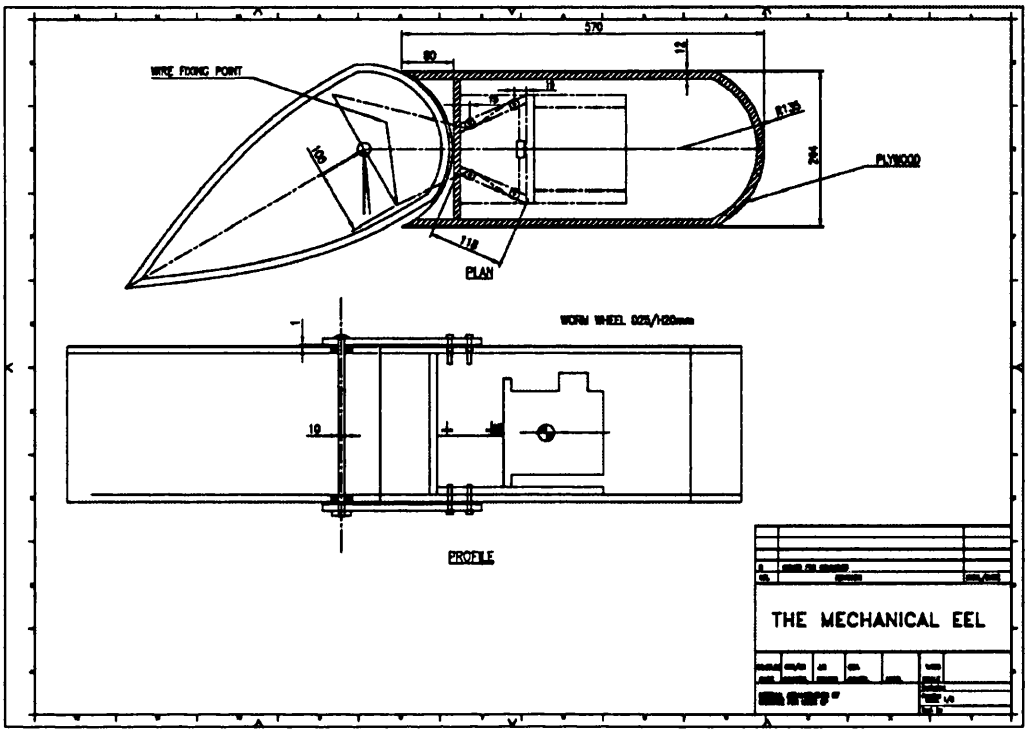

Figure 5-2: The first plan for the McEel

The main challenges of this proposal were the trouble of waterproofing it and the size of the motors. As the motors were meant to go inside the segments this would have meant that the each segment would have had to be roughly 250*250*600 mm. This would then have lead to a big moment being required in the joints and the possibility that the motors would run out of torque. The obvious solution of coupling the motors to gearboxes was beyond the budget constraints.

5.3 The first build – Mk1

For these reasons, it was decided to put the motors outside the model and have a wire drive system running through the sting to change the angle of the joints. Having the wire system turning the first joint was straightforward, as the wire could simply be attached to a pulley wheel that was attached to the moving segment. The difficult bit was however to transfer a turning moment to the second joint. It seems that the Robotuna avoided this problem by not having the segments truly independent (Barrett 1996). This makes sense as the intention was trying to duplicate a

carangiform swimmer, which makes only half a wavelength undulations. For the current study, it was desired to be able to emulate all swimming styles.

The solution to the problem was found by having a double pulley free to rotate around the axis making up the first joint. This pulley then had the drive wire coming from the sting to rotate it and these rotations would then be transferred to the drive pulley at the second joint by a new wire. The global angle of the second segment would then be independent of the global angle of the first segment. Only the position of the second segment would change with an angular change in the first joint. This system is similar to the one that was previously used in dentist's drills. This system is depicted below:

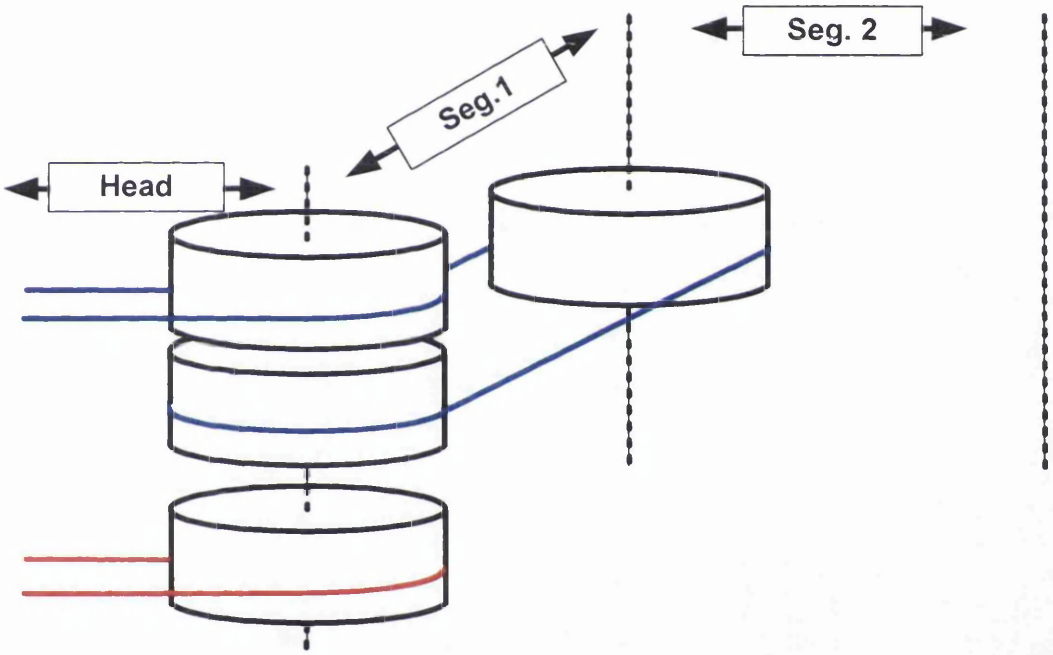

Figure 5-3: The system of freewheels which allowed the joints to operate independently.

In Figure 5-3, the bottom pulley with the red line around it is fastened to the first segment and is used to control its rotation. The double pulley above it is the freewheel and the blue lines are thus used to control the tail segment.

In conjunction with the building and testing of Mk1 the general test set up also had to be decided and it was soon evident that testing the forces involved in the propulsion of a mechanical eel is more complex task than one might first envisage. One of the main obstacles is the undesirable interaction between the sting and the model. To minimize this interaction the sting has to be slender but to avoid excessive bending the sting has to be bulky. Furthermore, the longer the sting gets the longer the drive

wires or drive shafts would have to be which would lead to a less precise drive system. However if the sting is too short the model will experience free surface effects. It therefore became apparent that a suitable sting would have to be found before the rest of the drive system could be designed.

In his book "Fluid - Dynamic Drag" Sighard Hoerner (1958) suggests that the free surface effects are negligible for submarines at a depth to centreline of more than 5 times their diameter. Although the submariners might be more concerned about being spotted than undesirable flow effects in their own right this figure was used as a first estimate. This would have made the sting for Mk1 585 mm from the waterline and down to the top of the model. In order to verify this value a simple experiment was conducted in the Denny Tank in which a 130*130*200 mm box with 65 mm pyramidal fairings front and back was towed through the water below a 20*50 mm steel bar with wedge shaped fairings 30 mm long. The model was towed at various speeds with wool tufts attached so that the flow around it could be visualised. It turned out that a submersion of the centre of the box of 400 mm was more than sufficient for there to be no visible interaction between the surface and the box even when the box was towed at 2 m/s.

After deciding the size of the sting, the way of measuring the forces on the eel had to be decided. The intention was to have the eel swim in such a way that it used the minimal amount of energy to overcome its resistance. The self-propulsion speed of the eel had to be determined in order to calculate the transport efficiency. The initial aim was to do this with strain gauges measuring the bending in the sting. The challenge was however to decouple the forces acting on the model from the forces acting on the sting. Various designs were proposed ranging from an elongation of the sting inside the model to having two strain gauges at different vertical positions on the dry part of the sting. This problem was solved by utilising a waterproof load cell inside the eel.

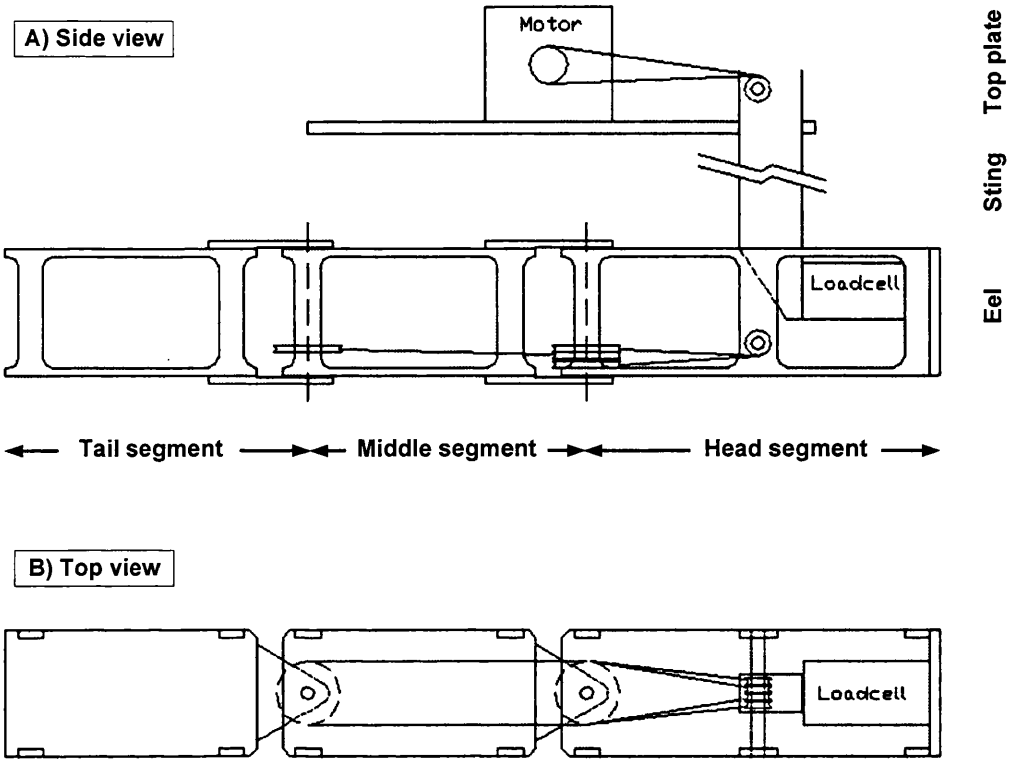

Figure 5-4: The Mk1 top- and side-elevation

Figure 5-4 A) shows the side elevation whilst Figure 5-4 B) shows the top elevation of this system. The drawing shows the aluminium skeleton and the working components of the design. The intention was to get the model working first and then fair it off with foam panels and weights to make it neutrally buoyant and ready to swim. This eel was at no time intended to be watertight.

As indicated, the motors were attached to a steel plate, fastened to the carriage. The wires ran around a worm wheel and then over a direction changing pulley and down through the sting. Once inside the fish the wires were again run around a direction-changing pulley before one of them ran around the drive pulley for the first joint and the other ran around the afore mentioned double pulley wheel.

Each joint of the model was required to be able to swing up to 45 degrees from side to side. This amplitude of oscillation is larger than what is observed in nature (Gillis 1998) and it was chosen to allow experiments with novel swimming styles.

The pulley wheels which drove the joints where approximately 50 mm in diameter. The worm wheel at the motor end was 25 mm in diameter. This meant that the motor made maximum undulations of 90 degrees. Although this was less than ideal

conditions for a servomotor (Printed Motors GR12M4CH9T729) with a maximum rotational speed of 3000 rpm the model was built.

Immediately during testing though it became apparent that the system was not behaving as desired as the eel moved in a jerky and uneven manner. After a lengthy debate and several calculations it was postulated that the reason for the faulty movements was a lack of torque in the motors. The motors were rated at 1.33 Nm maximum and as seen in section 4.7, this figure would not necessarily be enough even with the 2:1 gearing.

5.4 The second build – Mk2

To remedy the lack of torque it was decided to make a gearbox at the top end of the sting. Due to a lack of funds, this had to be designed and made in-house. The gearbox was therefore made of a pulley and timing belt arrangement. Calculations indicated that the rotations of the motor could be geared by 16 times without losing the ability to undulate at 2 Hz. As it was decided that it was desirable to be able to make undulations up to this frequency the gearbox was designed as two stages of 1:4.

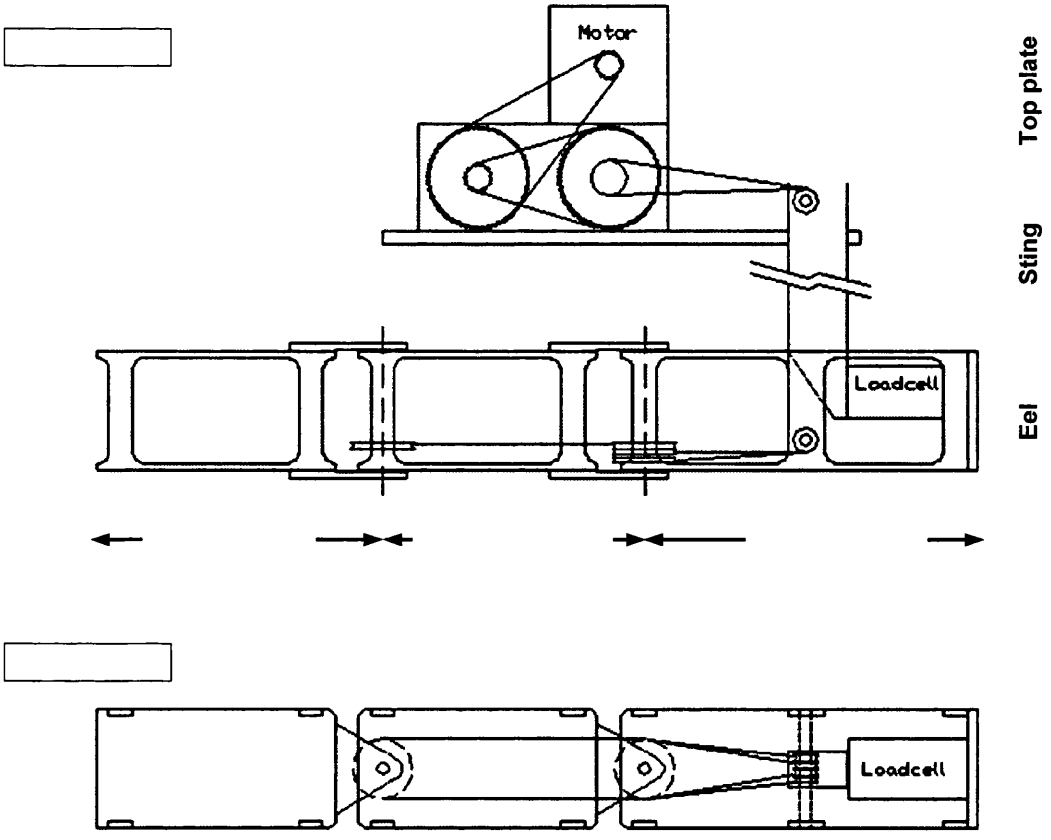

Figure 5-5: The Mk2 side- and top-elevation

As can be seen from the drawing the Mk2 was very similar to Mk1. The only changes were the addition of the gearbox and an increase in the diameter of the wires. In the Mk1, the wires were 1 mm diameter stainless steel wire, whilst this was changed to 2.3 mm for Mk2.

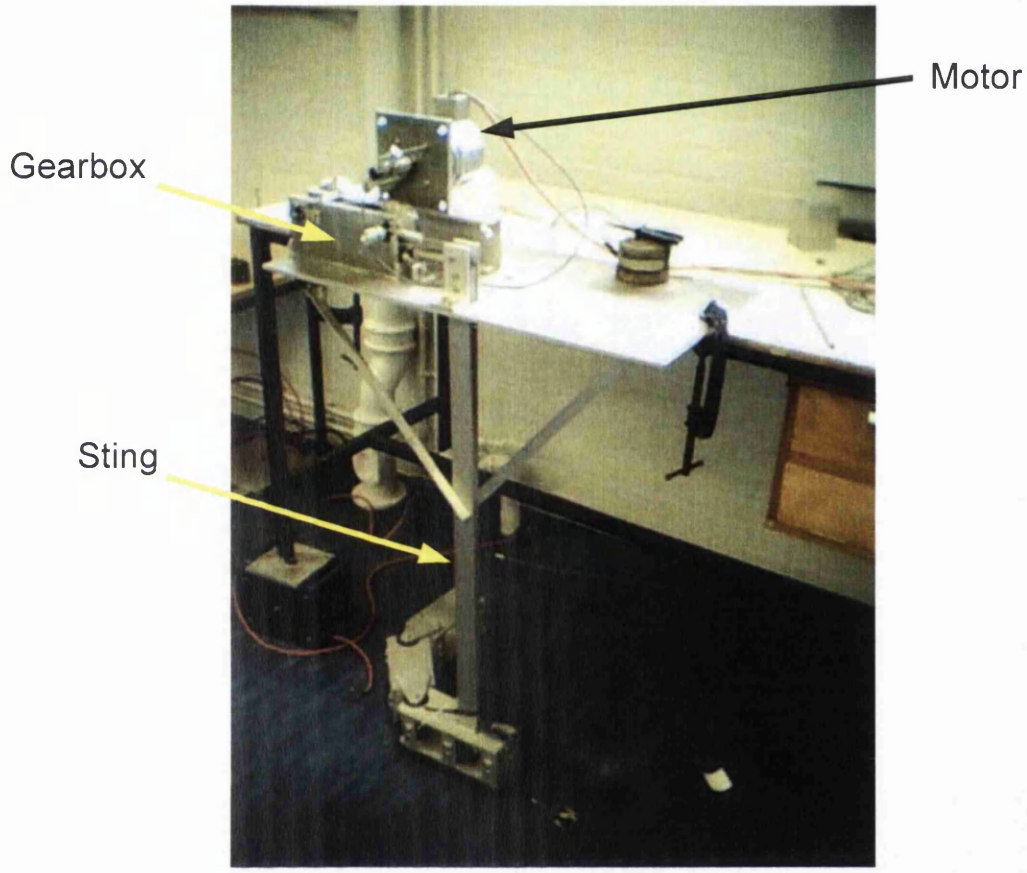

Figure 5-6: The Mk2 as built

Because of the previous failure, only one gearbox was initially built.

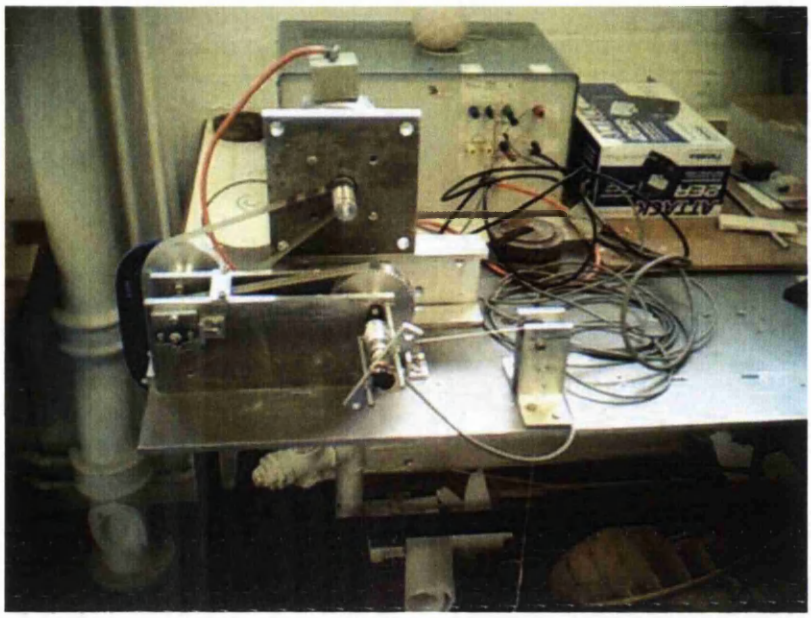

Figure 5-7: The gearbox of Mk2.

Although the Mk2 worked better than the Mk1, its motions were still uneven. This was not anticipated and for a while, the old wave-maker motors at the core of both Mk1 and Mk2 were suspected of being faulty. A closer inspection of the wire drive however came up with some startling results. The overall length of the primary wire drive was close to 2 m. The full undulating motion the wire was set to control was 50 mm * π / 4 =39.3 mm. The wire stretching about 4% could therefore accomplish a full swing from one side to the other. The torque of the motor was therefore being challenged not so much by the forces of the undulations of the model as by those involved in overcoming the friction due to the pre-tensioning.

An Mk3 in which the second stage of the gearbox was moved inside the eel was suggested but rejected because enough time had now been wasted on trying to get a wire drive system to work.

5.5 Mk3 - the final solution.

To get rid of the problem of the stretching of the wires a system with drive shafts running through the sting was selected. Initially this idea had been rejected due to fear that the sting might bend and that the shafts themselves might start to vibrate. The first problem was overcome by making the sting substantially bigger than first

planned. The sting for Mk1 and Mk2 was 50 mm long and 20 mm wide whilst the sting for Mk3 is 102 mm (4") long and 51 mm (2") wide. This extra bulkiness was also required to house the two drive shafts. This construction meant that the sting had to be firmly attached to the eel. It was therefore impossible to decouple the drag of the sting from that of the eel and all force measurements are consequently for the over all system of the eel and its sting.

The problem of the shaft instability was overcome partly by their sheer size (12 mm diameter) and partly by the fact that the gearing on the top end slows them down.

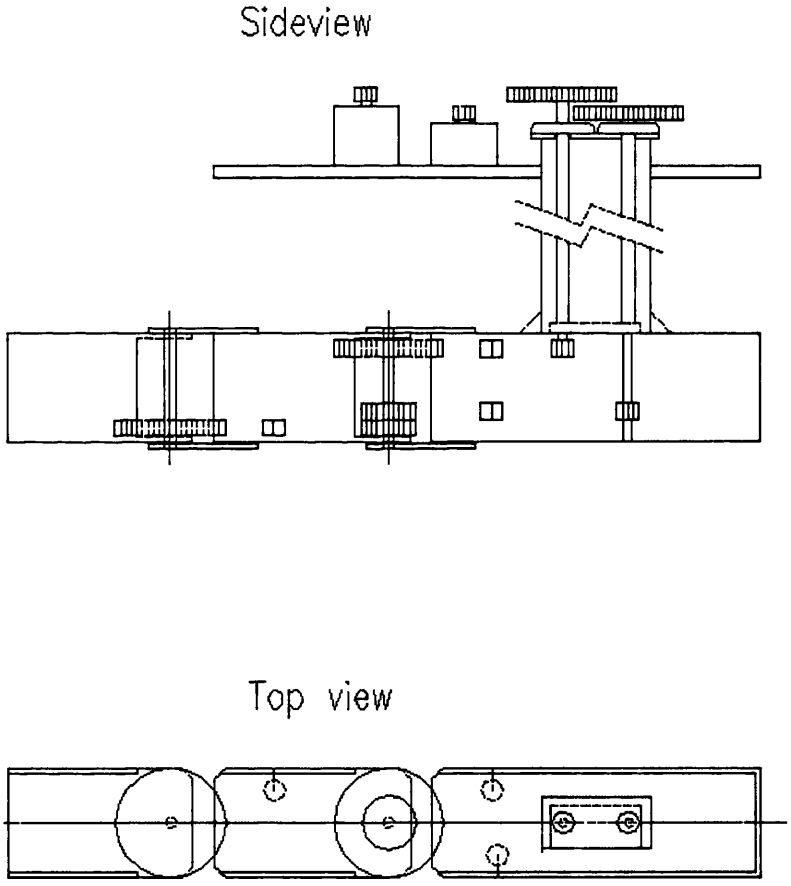

Figure 5-8: The Mk3 top- and side-elevation

As can be seen from this drawing the idea of having a free-running double pulley to transmit the forces to the backmost joint was retained. The timing belts needed to be individually tightened. For this purpose, three idle wheels were added. Asides from that this design is quite similar to the Mk1 and Mk2.

Due to caution and budgetary constraints, Mk3 was first made with only one segment. This was deemed a complex enough model to validate the general design.

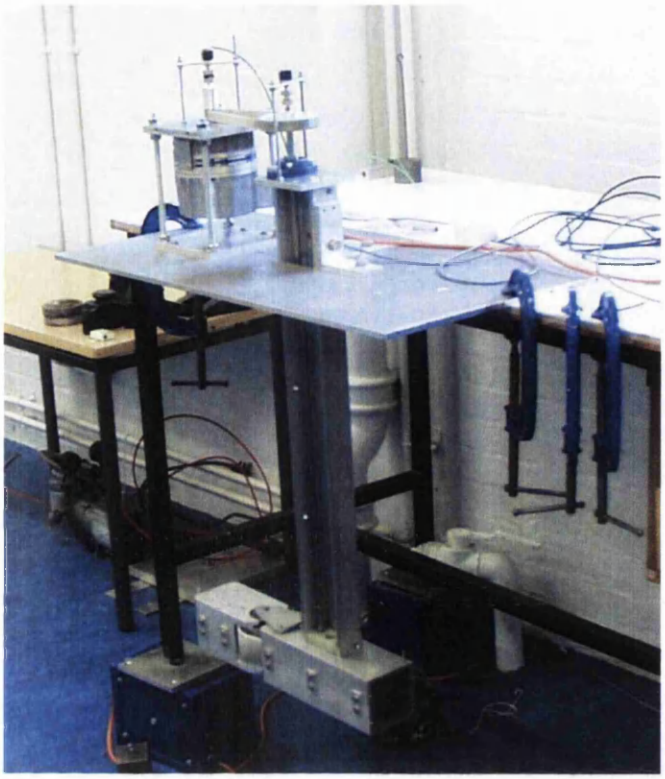

Figure 5-9: Mk3 as built with one joint.

This set up was tested and found to be a major improvement from the two previous designs. The joint, and later the two joints, could now be moved in a smooth and controlled manner as desired.

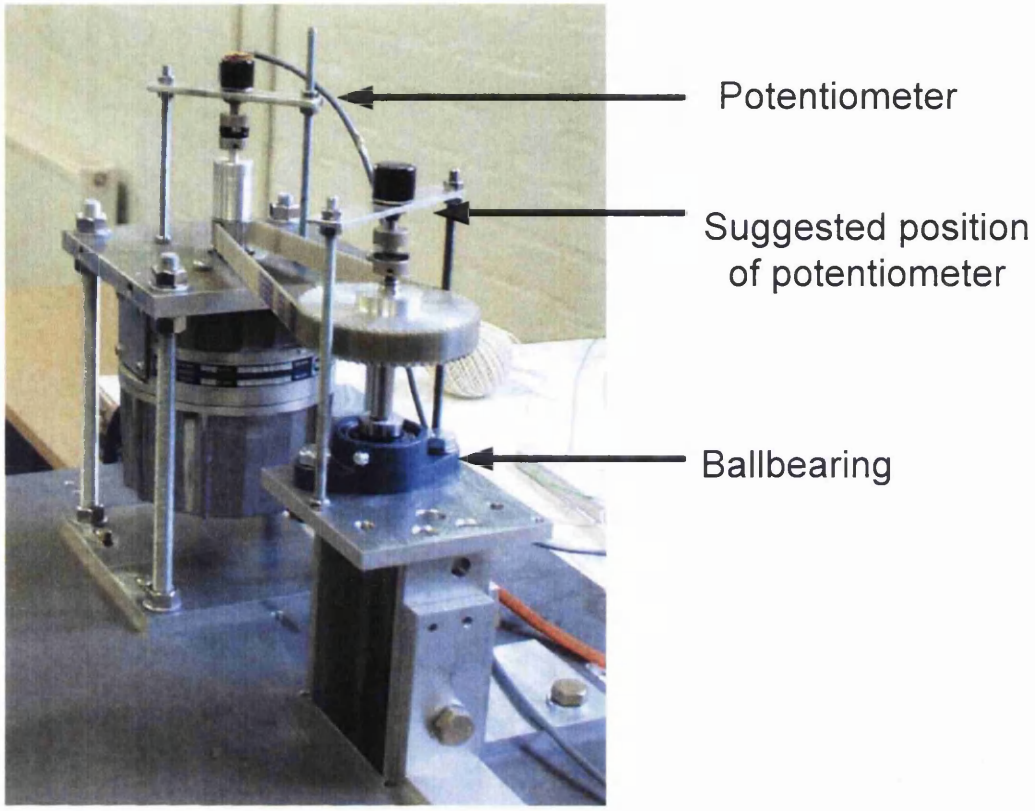

Figure 5-10: Mk3 – the gearbox

In Figure 5-10, it can be seen how the drive shaft is kept in place by a bearing at the top end. The full weight of the shaft rests on this bearing.

A potentiometer was used to infer the angular position of each of the joints. The two potentiometers in the picture are due to an initial uncertainty about its ideal position. This dispute was quickly resolved and the potentiometers were mounted on the motor shaft. This increases the sensitivity of the system at the expense of adding one more flexible belt between the real angle of the joint and the position at which it is measured.

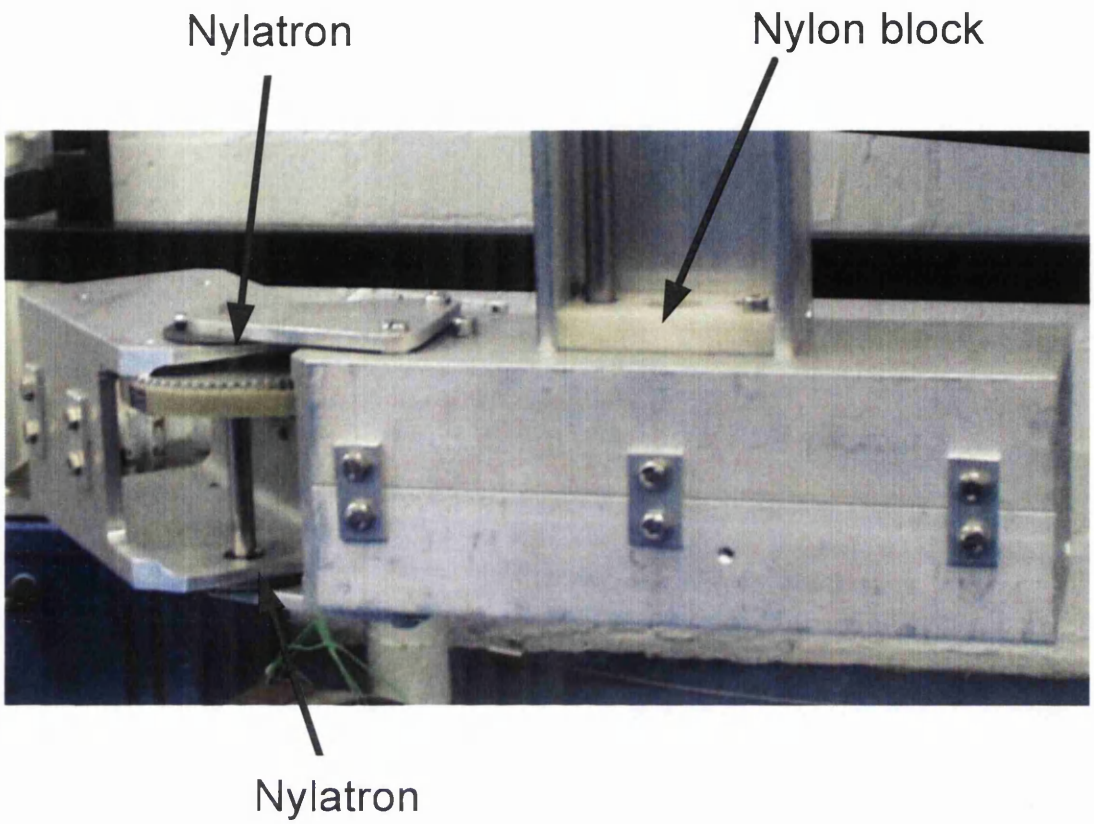

Figure 5-11: The joint of the Mk3

At the lower end, the shafts run through a nylon block. This is lubricated by water when the model is operating. The joint itself rests on two pieces of Nylatron GSM™, which also lubricates in water. These black Nylatron washers can be seen on the top and bottom of the tail segment to the left in Figure 5-11.

As can be seen from Figure 5-8 the idea of having a load cell inside the eel was abandoned with the Mk3. As the sting and the eel was now one unit, the forces experienced by it had to be measured for the system as one. A six-component load cell was therefore mounted at the top of the whole apparatus linking this to the towing tank carriage.

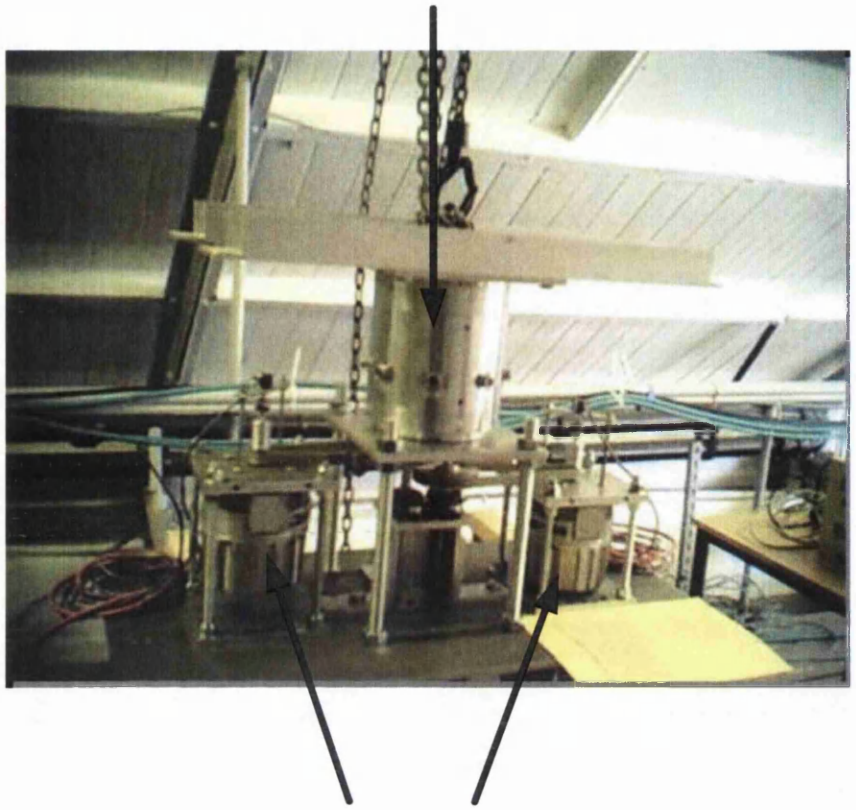

Figure 5-12: The top plate with the load cell

Figure 5-12 shows the top plate of the model with the top of the sting in the middle. The two motors are mounted on either side and the load cell is the metal cylinder mounted above the timing belts. The cross beams on top of the load cell would then be clamped to the towing tank carriage.

The Mk3 was slightly modified at a later stage, which will be explained in detail in chapter 6.3. The working parts of the model were un-changed though and this model generated all subsequent test data for the McEel.

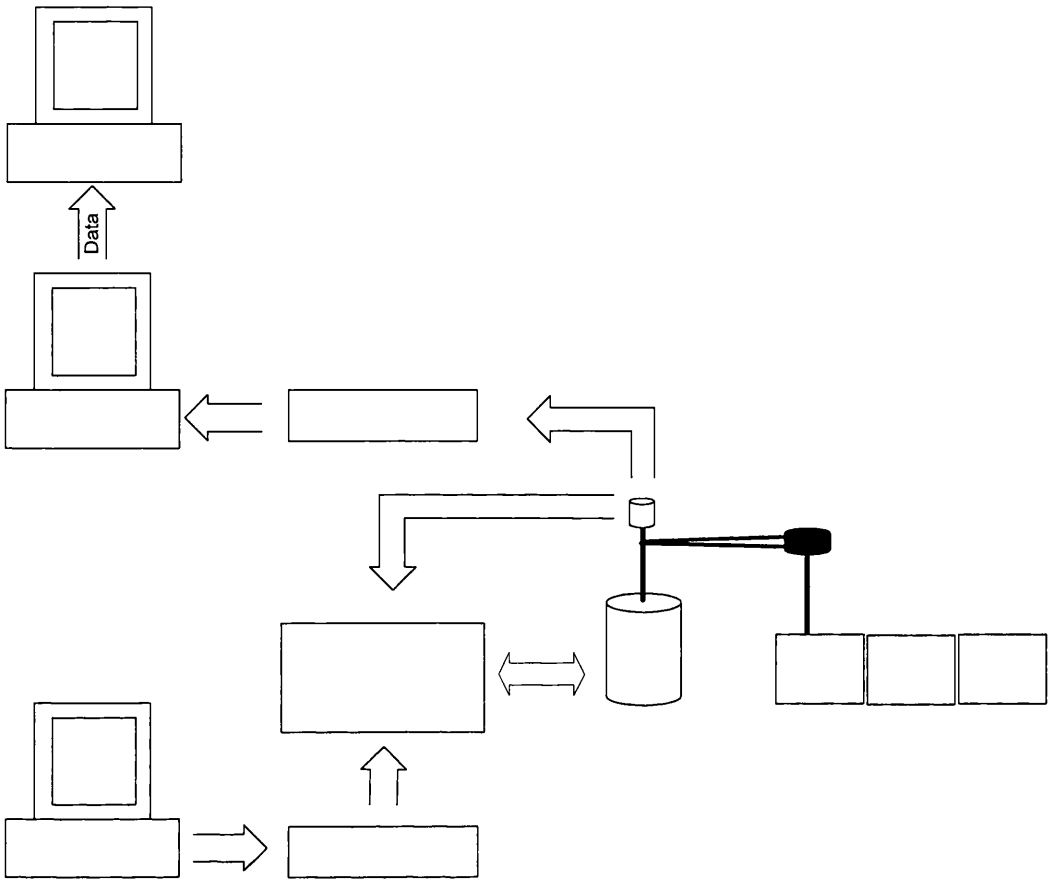

Figure 5-13: Block diagram of the signal routing from the McEel

Figure 5-13 shows schematically the setup adopted during testing. To the left of the drawing three computers are indicated. The lower one was used to generate the drive signal. This was transformed in a D/A converter before being transmitted to the power amplifier. The tacho signal coming from the servomotors was then employed by the power amplifiers together with the signals coming from the potentiometers mounted on the motors to ensure that the motors behaved as required:

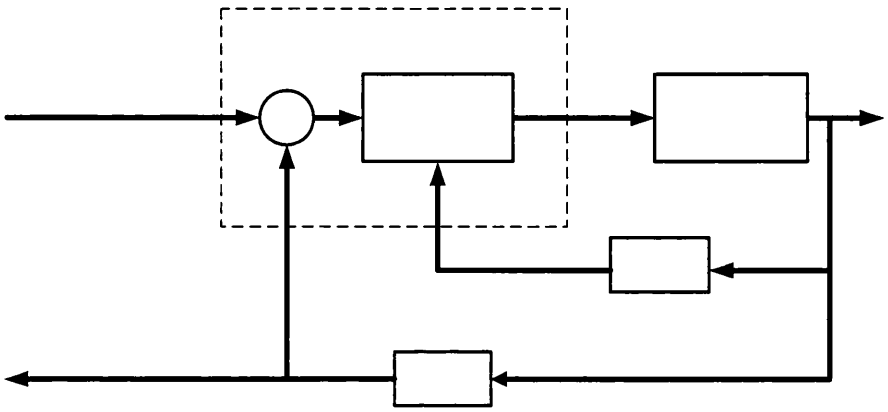

Figure 5-14: Block diagram of the control system

As can be seen in Figure 5-14, only one potentiometer is used to control the angle in the joint and measure the angle of the same joint. This may be an unusual design but it was calibrated against manual measurements and it seemed to work.

The measured values of transverse and longitudinal force, carriage speed and the angular orientation of the segments were initially sent through a 12-bit A/D converter and into the program Chart running on the middle PC in Figure 5-13. In the later tests, a 16-bit A/D converter was used in conjunction with the program VI Logger. In both cases the data files were then taken to the top computer for data analysis using the MatLab software suite.

One weakness with this set up is that the system measures the angular orientation of the motor to infer the angular orientation of the two segments below the water. This is a set up dictated by financial constraints and although it was easy to verify that, it worked statically, it was harder to verify that elongation of the belts or other mechanical errors did not lead to dynamic errors in the angular measurements. To quantify these errors the McEel was set to oscillate in the dry condition. Assuming then that the real force signal created by the McEel's motions in air could be predicted this could then be compared to what was measured. A phase correction could then be added to the angles measured by the potentiometers in such a way that the error between the computed signal and the measured one in the longitudinal and transverse direction was minimised:

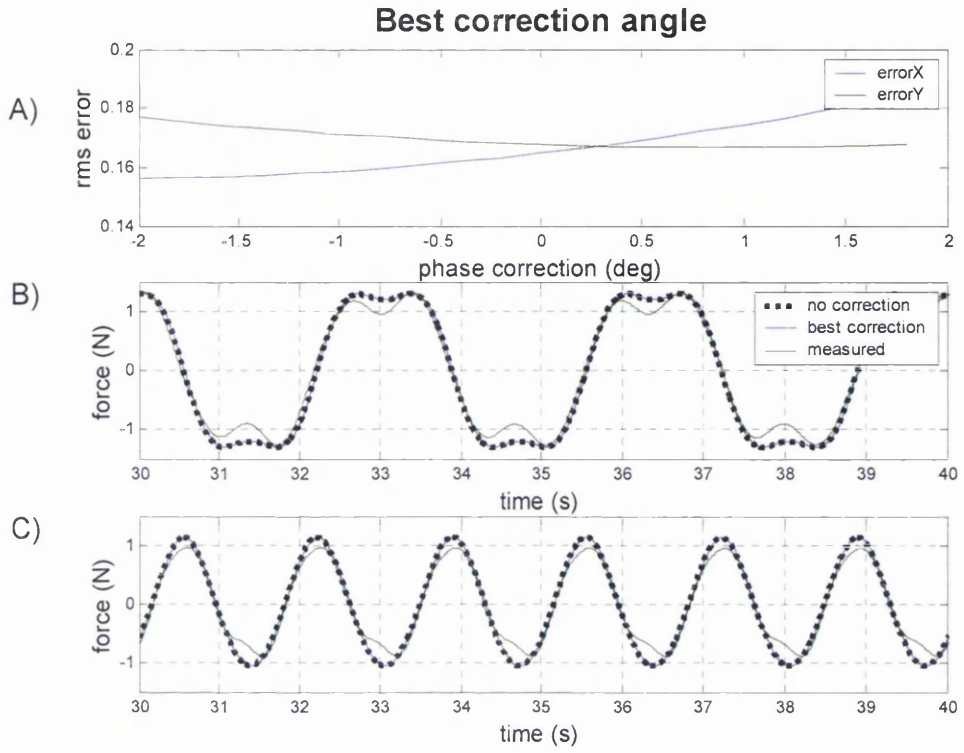

Figure 5-15: The measured angle correction

Part A) of Figure 5-15 show how the r.m.s errors in the longitudinal and transverse direction change as various corrections to the measured angle are applied. Part B) and part C) show three signals for each of the two directions. The black dotted signals in both graphs depict the computed signal with no correction of the measured angle. As can be seen this overlaps the blue lines, which depict the computed signals with the best correction to the measured angle. The green lines, which differ from the other two, depict the measured signals.

The run, depicted in Figure 5-15, is a 40-40-0 run with an overall excitation frequency of 0.3 Hz. In this example, the ideal dynamic phase angle correction is -1 degree, which explains why the signals without any correction virtually overlap the signals with the ideal correction. The ideal correction is the one in which the sum of the r.m.s. errors in the longitudinal and transverse directions is at a minimum. For all of the runs that were tested this angle correction was negative, meaning that the motions of the physical McEel seemed to be trailing the measured angle. This correction angle seemed to grow bigger as the frequency of the overall excitations increased as well as when the amplitude of the overall excitations decreased. For none of the runs tested was however this correction angle greater in magnitude than

3.6 degrees. Although the forces experienced by the physical McEel would be greater when submerged in water this was seen as justification for measuring the angle of the joints at the motor end as opposed to in the joints themselves.

6 Experiment programme

6.1 Introduction

In this chapter it will be shown how the raw data used later on in this thesis was obtained. As none of the persons involved had any previous experience with the testing of an eel-like structure several errors were made along the way and numerous important lessons were learned.

At the end of this chapter it will also be shown what conclusions could be drawn from the initial data itself. The full set of test data is presented along with its analysis in chapters 8 and 9.

In comparing the numeric model with physical tests, two potential un-knowns are compared to each other. Any disagreement between the two might be caused by inaccuracies in the physical tests, or by a faulty numeric method or indeed by one or several errors in both of them. It was therefore considered vitally important to build up confidence by testing the simplest scenarios first in which the results can be predicted with a high degree of accuracy. For this reason, the tests were done in four stages.

Initially the McEel was tested in air. This was done to ensure that the mechanical drive system and the data acquisition system both behaved as they should. These tests were used for verification purposes and only the one in Figure 5-15 is presented in this text.

Once consistent results had been obtained in air, the test program advanced to zero forward speed runs with the two segments moving in unison, the so-called single flapper bollard-pull tests. These were the most basic hydrodynamic tests and they will be presented both in section 6.8.1 and chapter 8 as several important lessons were learned from them.

The next set of tests was the bollard-pull runs with a phase angle between the joints. These runs were a logical step from the single flapper tests towards the forward speed runs but they were also used to answer several questions regarding the phase angle. Among these were: does the thrust vary with phase angle and is the Morison Equation equally suited for different phase angles?

The last set of tests was the forward speed ones. These tests were central to this project and they will be examined both in sections 6.8.2 and 9.3.

All the tests presented in the main text of this thesis date from March 2005. Many tests had been performed before this date but except for the ones performed in air, these tests were used to build up experience and gain confidence rather than to gather data. Consequently, none of these previous tests is reported in this thesis.

For all physical measurements and numerical processes, it is important to evaluate the accuracy attained. For this study, this is described in Appendix C and Appendix D.

6.2 Towing tank and blockage

Once a McEel model had been built that could perform the desired motions the difficult process of getting meaningful results from it commenced. Initially it was tested in the Denny tank. All the initial tests in air were performed there with satisfactory results. The bollard pull tests that were performed in this tank did however contain a high level of electrical noise and once the towing tank carriage was started up to perform tests with forward speed the level of electrical noise rendered the resulting data useless. A considerable amount of time was spent on trying to verify where the noise was coming from as well as trying to get rid of it. In the end it was however decided that the tests should be conducted at the Acre Road Hydrodynamics Laboratory.

The Acre Road tank is 70 meters long and has a cross section as depicted in Figure 6-1.

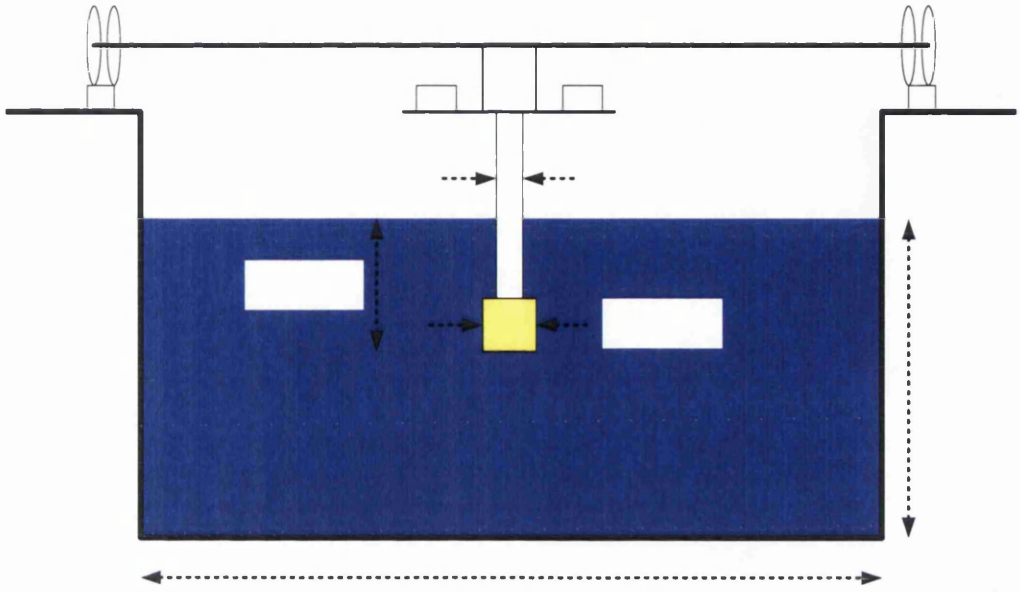

Figure 6-1: The towing tank blockage effect

The tank has a maximum water depth of 2.4 meters but it was not full at the time of the final testing. The cross sectional area of the sting and the eel in a stretched straight position is 0.02 m^2 which is about 0.02 % of the cross sectional area of the tank. No blockage effects are therefore considered when the eel is in this position. Once the eel starts to oscillate, it will at times represent a much larger area to the oncoming flow. However, the combined cross sectional area of the sting and the eel swung out to its most extreme position never exceeds 0.5 % of the area of the tank and therefore no blockage effect is considered for any of the tests.

6.3 Model modifications

This section explains the modifications that were done to the McEel after its initial testing. These modifications were done to address two main concerns that had become apparent during the initial testing in the Denny Tank. These concerns were:

- The forces that were generated were quite small
- No good methods for quantifying the end effects at the tail were available

The fact that the McEel was generating small forces was not a problem in its own right but it was made so by the fact that the LMC-6524-1000N load cell had to be

used. This particular load cell had to be used as it was the only suitable multiple-axis load cell available. As the name implies this load cell is rated up to 1000 N. The fear was therefore that the measurements would become inaccurate if the loads that were measured were too small.

The difficulty with measuring the small forces led to the idea of attaching fins to the McEel. The fins were to run along the top and bottom of the McEel from the back end of the sting and to the tip of the tail. Two sets of fins were produced, one protruding 50 mm from the central body and one set protruding 25 mm from the body. In the end only the 50 mm fins were employed though as this turned out to generate forces that were still within the limits of the physical set up.

As none of the numeric models described in chapter 4 take account of end effects and as one of the reasons for trying to model the McEel's swimming style on anguilliform locomotion was the desire to avoid the large foil tail it was decided to taper the tail of the McEel. The final version of the McEel, the one that was tested, therefore looked like this:

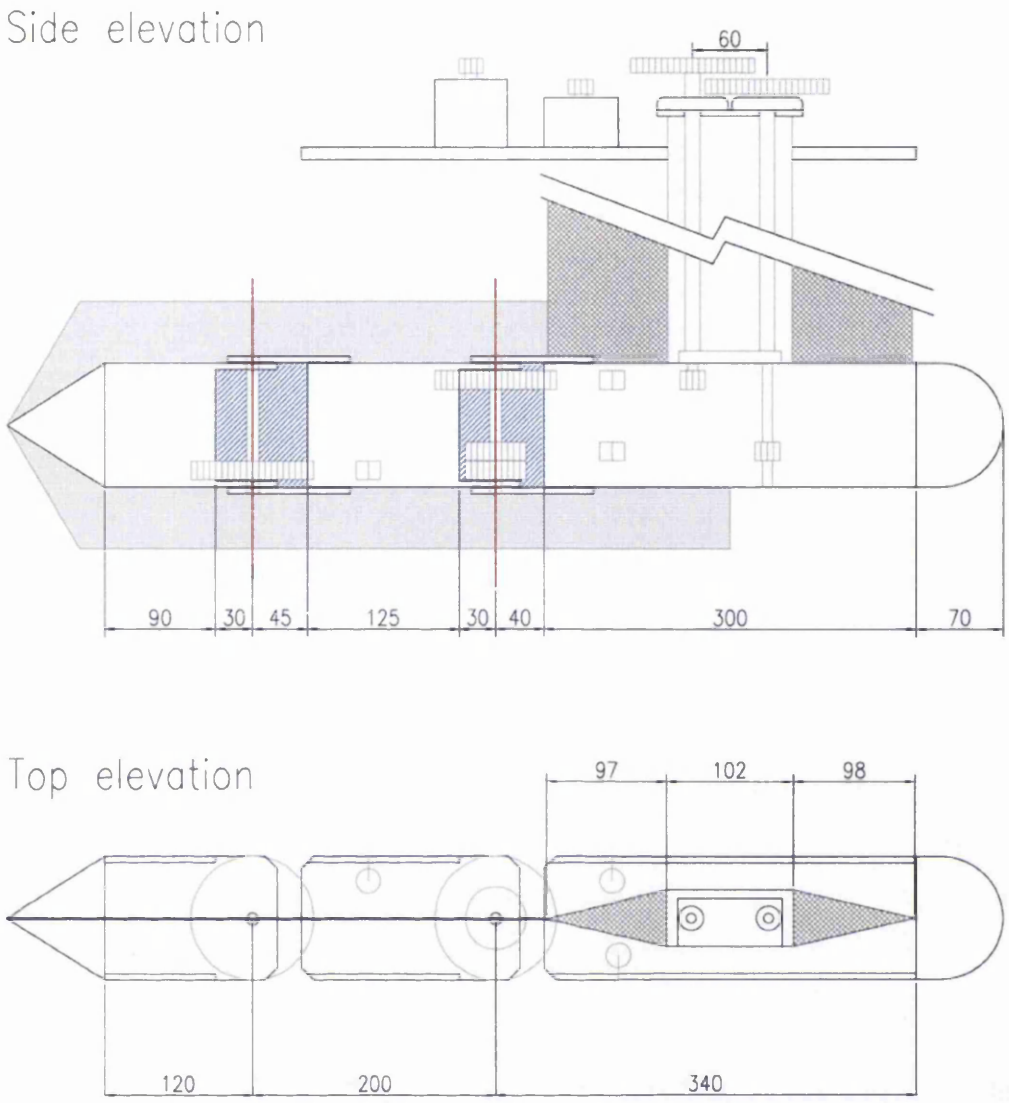

Figure 6-2. The modified Mk3 with fins and a tapered tail.

The tapering of the tail started 120 mm behind the tail joint whilst the tapering of the fins started 140 mm behind the same joint. The sting had triangular fairings front and back making it a total of 297 mm in the longitudinal direction. The areas where water could flow through the model are marked with blue diagonal hatching on the side elevation of Figure 6-2. These holes were an unfortunate result of the construction and the effect of them had to be estimated through a relatively crude test.

6.4 The effect of the holes

The holes were positioned at each joint and were needed for the belts to be able to operate. The undesired side effect was that water could flow through the eel as well.

The addition of the fins minimised the importance of this phenomena but did not remove it. In order to try to establish the effects of the holes the one in the last joint was sealed with adhesive tape for two single flapper tests. The forces measured for the test of 30-degree amplitude and 0.3 Hz excitation frequency are displayed below:

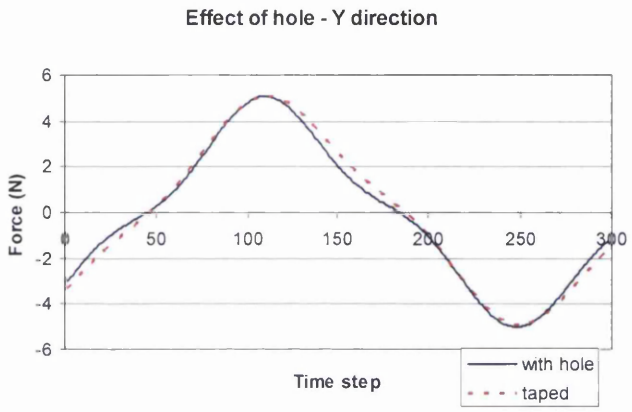

Figure 6-3: The effect of the hole on the force in the transverse direction

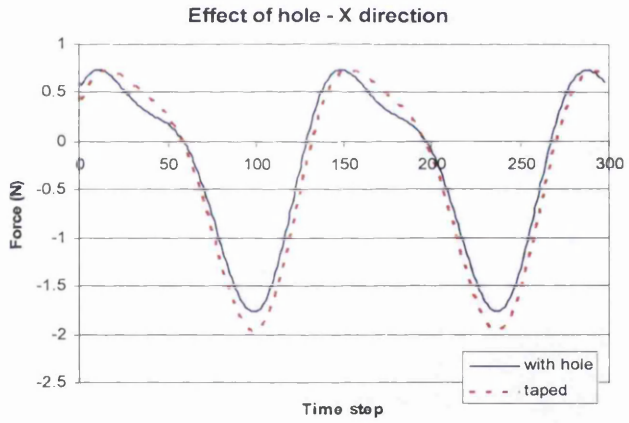

Figure 6-4: The effect of the hole on the force in the longitudinal direction

As can be seen in Figure 6-3 and Figure 6-4 the two tests show perhaps surprisingly good agreement throughout most of the cycle. The two points at which the two disagree in the Y-direction is as the flow is about to turn at the extremities of the pendulum motion. As the angular velocity of the eel increases, the hole loses its importance for the transverse force. In the longitudinal direction, the two graphs also differ as the velocity of the pendulum is at a maximum and in general, the hole seems to make more of a difference in this direction. The mean forward force was 19 % less with the hole present than with it taped over.

Ideally, the holes should not be there, and Figure 6-3 shows that they do make a difference at certain points of the cycle but there was no obvious way of getting rid of them within the constraints of the budget.

6.5 The resistance of the sting and the resistance of the eel

Once the McEel starts to move forward it is subject to numerous forces and one has to be careful to ensure that the ones that are measured are the ones of interest:

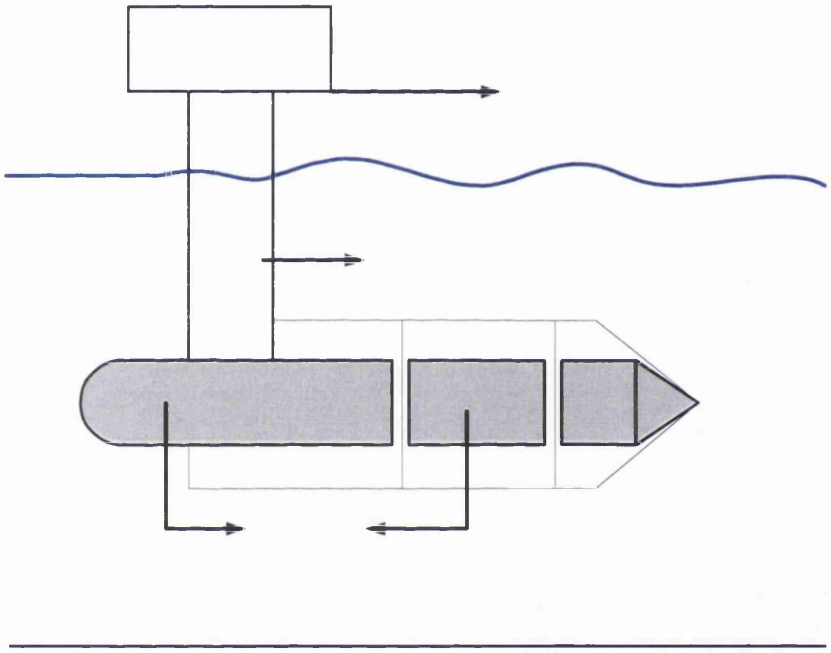

Figure 6-5: The forces present when swimming

In Figure 6-5, the forces experienced by the McEel are presented. The reason why the resistance of the eel is denoted the "true resistance of eel" is that various other researchers have assumed that the resistance of an actively swimming eel is the same as the stretched straight resistance of the same animal (Barrett 1996, Gray 1936 see chapter 1.1 for more). In the tests presented in this thesis, the net forces in the longitudinal direction are measured by the load cell and the forces due to swimming are sought to be predicted by the Morison Equation and other methods. There are thus two un-known forces namely the resistance of the sting and the true resistance of the McEel.

In addition to the forces presented in Figure 6-5 there will be interaction effects between the sting and the eel. These effects are unfortunate as they are very hard to

quantify with any level of accuracy. The area where the sting attaches to the eel is less than 1% of the total wetted surface area of the entire eel. It is however important to emphasise that this area is calculated twice. The following figure may help explain this:

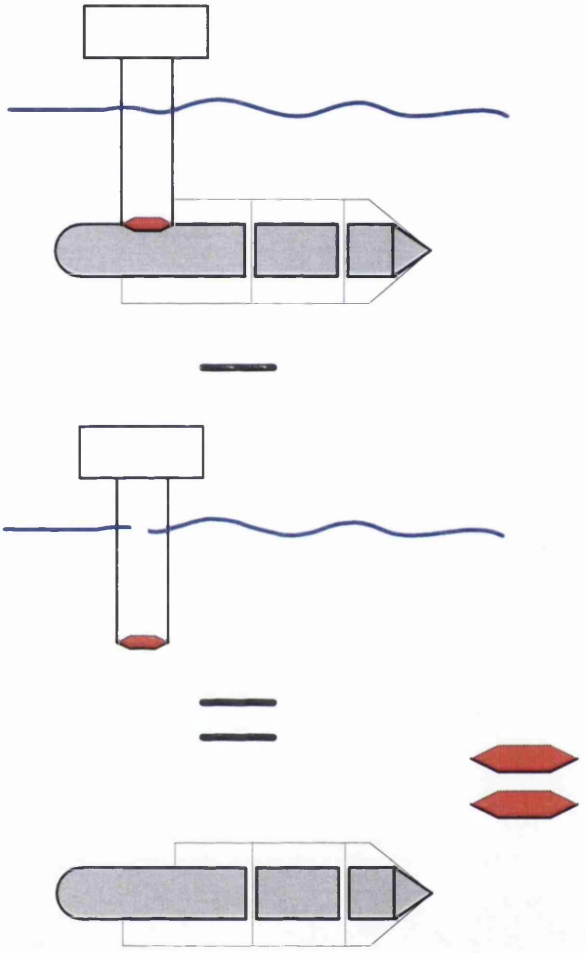

Figure 6-6: The error of the wetted surface area

In Figure 6-6, it is shown how the resistance of sting is subtracted from the resistance of the eel in the stretched straight position to find the stretched straight resistance of the eel on its own. The resistance of the eel and the sting will however not include the wetted surface area indicated in red, which would be there if the eel were on its own. Additionally the same red area is measured for the sting on its own whilst it would not be there when the eel is attached to it. The error involved with this area is thus included twice.

If the resistance of the eel and the sting had been computed based on wetted surface area this area could have been subtracted. As the resistance estimates are purely

empirical there is however no easy way of doing this and the error introduced by this area and other interaction effects have to be accepted.

It was thought that the resistance of the sting would be straightforward to quantify. An exact replica of the sting was therefore built and attached to the same load cell that was used for the McEel. This dummy sting was then towed at various speeds to generate a resistance curve. Unfortunately, the forces generated by the sting were small and the electrical noise present on the carriage was considerable even at the Acre Road site. The resistance curve for the sting therefore took more time to construct and became less accurate than anticipated:

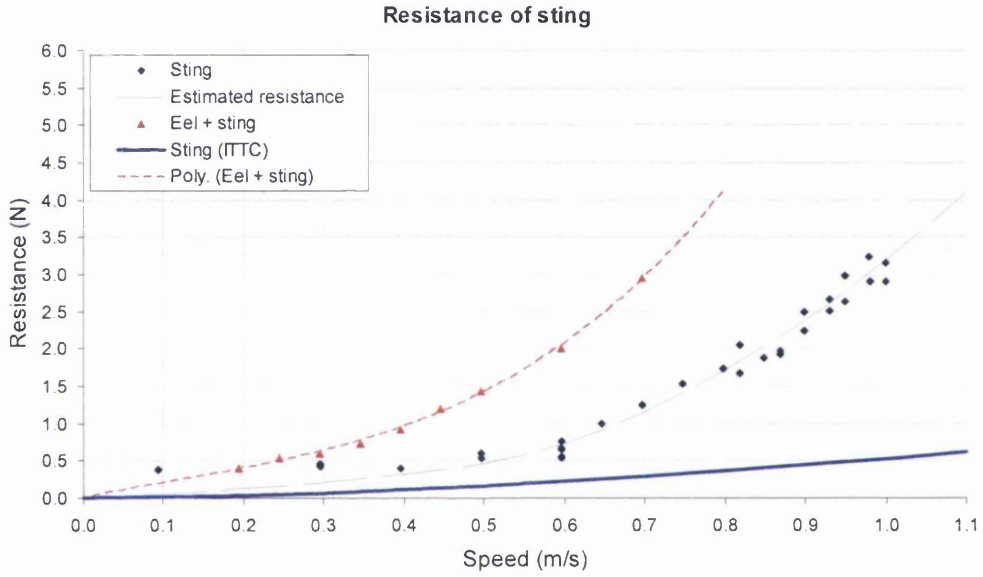

Figure 6-7: The resistance of the sting

In Figure 6-7 the estimated resistance of the sting on its own is presented as a dashed blue line together with the data points on which the estimate is based. The accompanying red dashed line is the resistance of the sting and the eel when the eel is in its stretched straight position. The solid blue line is the 1957 ITTC line for the sting and is presented as reference. The sting did not produce substantial waves below 0.5 m/s and it is therefore surprising to find that its measured resistance varies considerably from the ITTC line even below this speed. A picture of the waves generated by the dummy sting at 0.5 m/s may help to explain this:

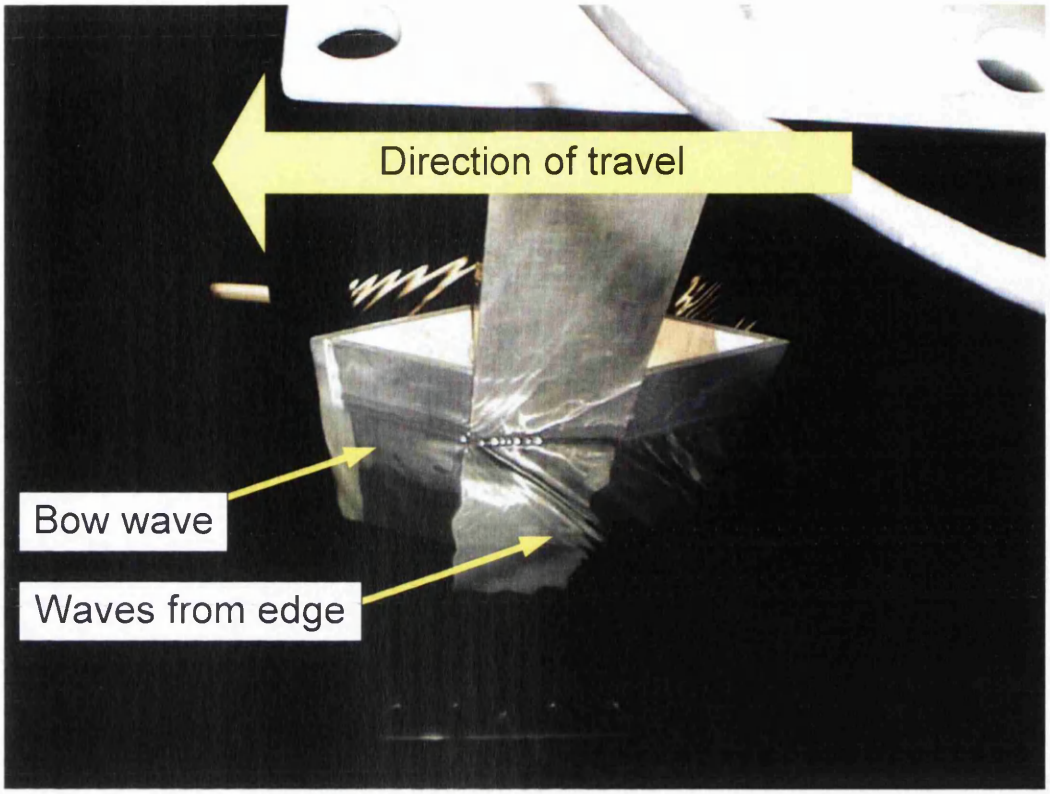

Figure 6-8. The wave profile of the sting at 0.5 m/s

As can be seen in Figure 6-8 the sharp edges on the sting generated substantial waves and one can therefore only assume that the under water turbulence caused by the same edge is equally important. The fairing that was chosen for the sting was thus not ideal.

Any AUV or similar craft based on the McEel concept has to overcome the true resistance it generates. In the case of this thesis this force has to be estimated to allow any comparison between the predicted thrust generated by the eel and the total force as measured by the load cell.

Estimating the true resistance of any swimming body is difficult and this probably explains why other researchers have assumed this to be the same as the stretched straight resistance (Barrett 1996, Gray 1936). It is however important to emphasize that employing this simplification can lead to some startling results. In his PhD thesis Barrett employs a thrust power ratio to quantify the efficiency of the Robotuna. This ratio is defined as:

$$ThrustPowerRatio = \frac{\left(\bar{D}rag + \bar{F}_{sled}\right)U_{sled}}{TotalPowerIn}$$

Equation 6-1

In this equation $\bar{D}rag$ is the drag of the stretched straight fish, $\bar{F}_{sled}$ is the force measured between the towing tank carriage and the fish, U_{sled} is the velocity of the towing tank carriage and *TotalPowerIn* is the power delivered through the tendons pulling the fish from side to side. This thrust power ratio of the Robotuna was estimated to be more than 100 % in some cases (Barrett 1996) indicating that the true resistance of an actively swimming apparatus can be smaller than its stretched straight resistance.

The separation of forces into thrust and drag is essentially an artificial one when it comes to the eel. It is difficult to determine where one begins and the other one ends. The stretched straight resistance of the eel is however, an appropriate bench mark for the true swimming resistance which is useful for comparison purposes. For this reason the true resistance of the McEel will be estimated as the difference between the dashed red and the dashed blue lines in Figure 6-7.

6.6 Procedure and observations

When the McEel was ready to be tested a considerable effort was spent on ensuring that it was straight, level and at the right immersion depth. The top plate of the dummy sting varied in dimensions from the top plate of the McEel as the latter had to accommodate motors and running gear. The McEel was therefore seated on several aluminum beams to get it to the right height.

The first tests that were performed on the McEel were bollard pull tests. In these tests the towing tank carriage was positioned at the end of the tank next to the beach with the McEel swimming away from it. It was assumed that any waves, if generated by the McEel, would propagate backwards and thus be dampened by the beach.

In the forward speed tests the model was towed from the beach end of the tank towards the wave maker. Once the towing tank carriage had reached a constant speed the McEel was set in motion. The forces in the longitudinal and transverse direction were monitored and a mean value for overall longitudinal thrust could be measured. The same test was the repeated for various speeds.

It turned out that the McEel generated substantial waves during the higher (>0.4 Hz) frequency runs. These waves propagated in all directions and they seemed to come

form the vibrations of the sting rather than from the motions of the McEel itself. During the forward speed runs these waves would progress down the tank faster than the speed with which the model was towed. This meant that the McEel was in effect generating waves which propagated forward. This was both worrying in that it indicated a loss in efficiency and puzzling in that initially it could not be worked out were these forward moving waves came from. A closer examination of the two directions in which the sting could vibrate helped explain the phenomena:

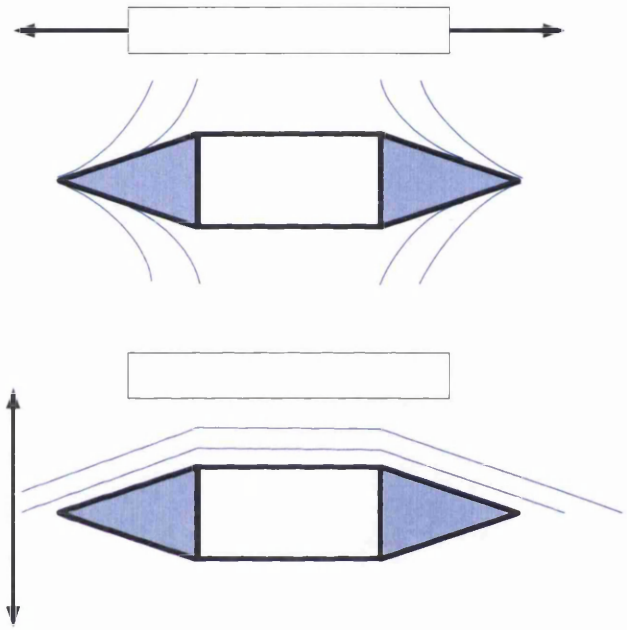

Figure 6-9: The waves generated by sting vibrations

As can be seen the cross sectional shape of the sting leads it to act as a wave maker when it is oscillated in the transverse direction. This direction is also the less stiff of the two and the one in which the amplitude of the generated forces is the biggest. It is also important to emphasize that this wave generation could affect the mean forward thrust measurements. This problem arises once the eel starts moving forward at which point the drag term on the sting will no longer average out.

The waves propagating from the sting were thus an unfortunate result of the test setup. As no simple solution could be found to get rid of these waves and as it was not clear that they had a measurable impact on the tests no action was taken to alleviate this problem.

The transverse vibrations of the sting were particularly noticeable during the testing of the 30-40-30 pattern at 0.8 Hz and 0.1 m/s. During this test vortex shedding was clearly visible from the aft end of the sting.

Vortex shedding from the McEel itself was also evident at the higher frequency tests (<0.3 Hz). These vortices were visible on the surface but did not seem to break the surface and thus cause waves even at the highest frequency (1 Hz).

At the particular frequency of 0.4 Hz the floor of the carriage vibrated with the motion of the eel. Examination of decaying oscillations of the McEel indicated that its natural frequency was in the region of 4-8 Hz depending on the direction of interest and forward speed of the carriage.

6.7 The effect of noise on average measurements

The mean forward thrust produced by the McEel was one of the values that were of particular interest during testing. In all the tests presented in this thesis this figure is computed directly from the raw data.

All the tests presented in this text are performed with a uniform excitation frequency for the two joints. At the beginning of each test the McEel was slowly swung out to the starting position where the angle in the front joint was at its maximum. This was done to minimize the jerk experienced as the motions started and thus the noise generated. To further reduce the importance of any transients the time history of the forces for each test was visually inspected and an area of near constant oscillations was selected for analysis.

Even so a fair amount of mechanical noise in the form of vibrations was present in all the tests (see Figure 7-1) and extracting the mean value of the forward force requires a high level of accuracy. The force signal that the McEel generated was generally characterized by large amplitude oscillations and small mean values. An exact number of periods therefore had to be analyzed to get the right result. The signal from the front joint was therefore analyzed and the zero upward crossings were identified. There was virtually no noise in the angular measurements and the upward crossings are generally more exact than for instance the extreme points. Due to the large variations in the forward force signal an exact integer number of oscillations of the McEel were required. However even if this exact integer was found the mean measurements could still be affected by the non-integer number of

noise wavelengths. For this reason it may be of interest to see how the mean thrust varied depending on which complete cycle it was based on.

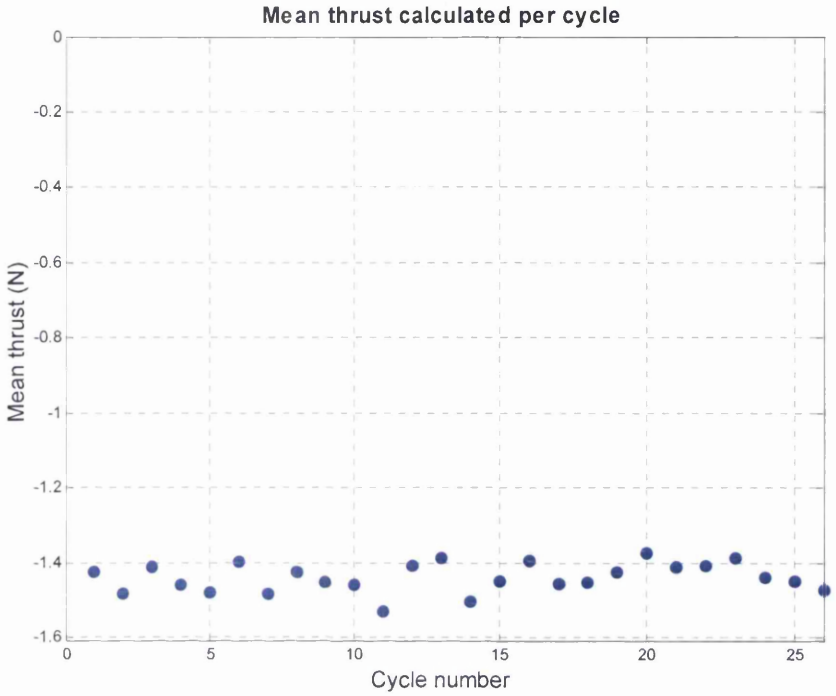

Figure 6-10: The mean thrust for 30-30-0, 0.6 Hz

In Figure 6-10 it can be seen how the mean force varies from cycle to cycle. This variation seems randomly distributed around some mean value and it is tempting to classify it as noise. The test depicted in Figure 6-10 is the 30-30-0 performed at 0.55 Hz and as such it is one of the higher frequency ones. These tests all showed a similar picture to the one depicted in Figure 6-10. Some of the lower frequency runs also converged:

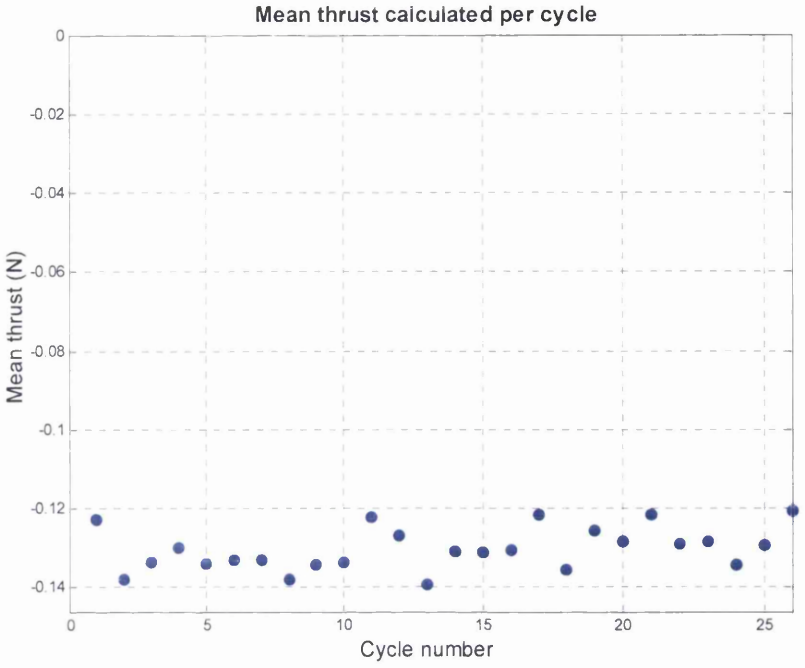

Figure 6-11: The mean thrust for 30-30-10, 0.2 Hz

Figure 6-11 shows one of the runs with the lowest frequency, and thus lowest mean thrust. This mean thrust still seems to vary by only a small amount around some mean value. However, some low frequency runs did not seem to converge at all:

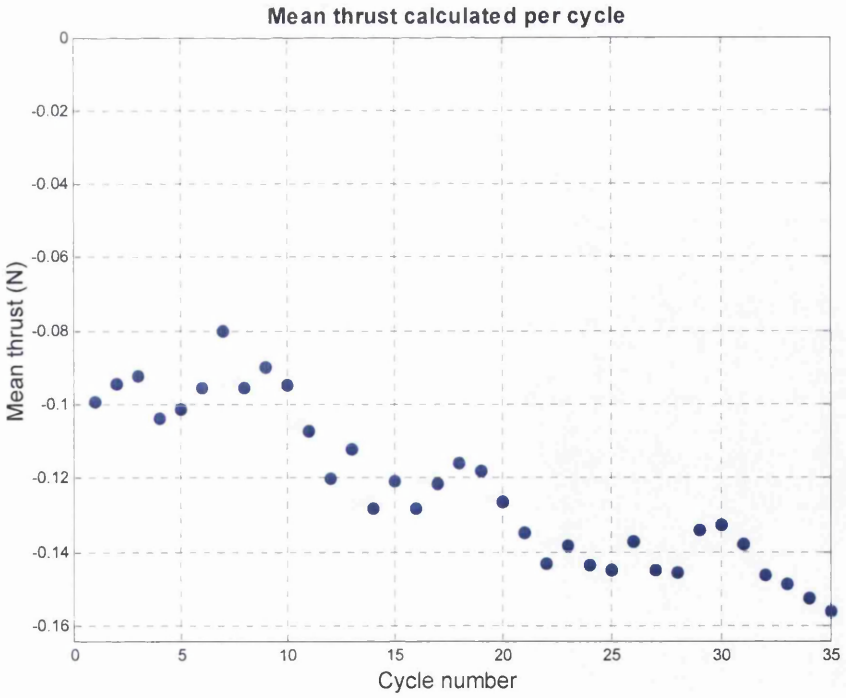

Figure 6-12: The mean thrust for 30-30-0, 0.2 Hz

Figure 6-12 depicts the 30-30-0 scenario at 0.2 Hz in the bollard pull condition. The value for the mean forward thrust varies considerably depending on which oscillations its measurement is based on. Furthermore, it does not seem as if the variation is leveling of. This prompted a re-test of the same condition but with a much higher number of oscillations:

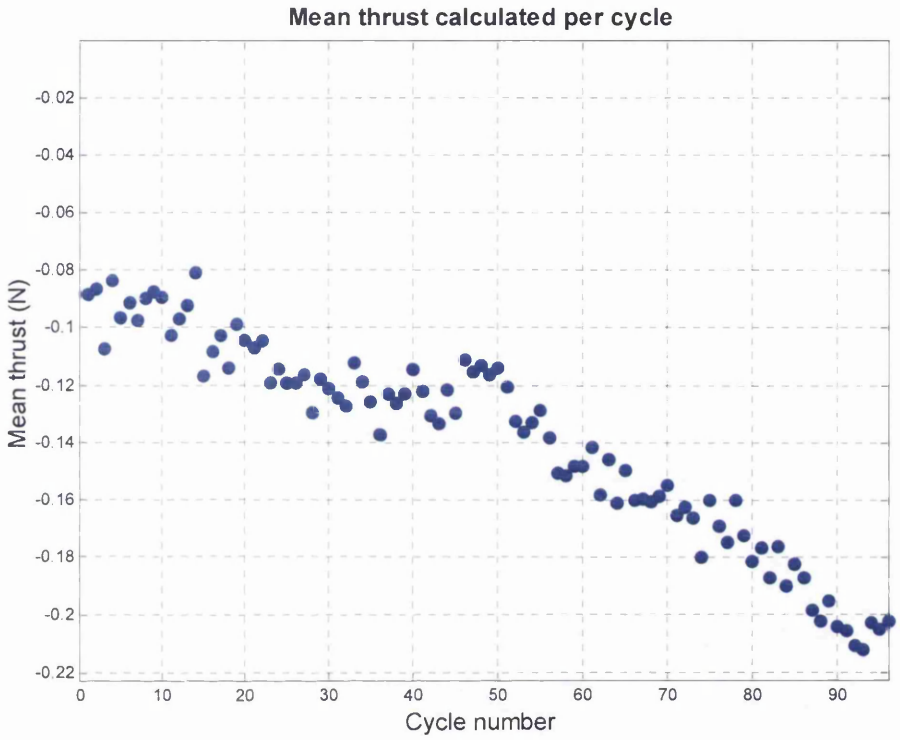

Figure 6-13: The 30-30-0, 0.2 Hz with many cycles

In Figure 6-13, it can be seen that the measured mean thrust does not reach a steady mean value even when more than 90 oscillations are compared. As the period of oscillation in this test is 5 seconds it took a considerable time to generate this data and it was not considered feasible to measure this many oscillations for each run. Especially during the forward speed ones in which the length of the tank would become an issue.

This result therefore caused a considerable amount of uncertainty. For a while, the drift was thought to be due to thermal effects in the data acquisition system but as the equipment had been given ample time to heat up, this was quickly ruled out. It was also considered that the McEel could be setting up a current in the tank. This would have been good news for the eel as a propulsive device but highly unlikely considering the minute forces measured and the substantial size of the tank.

When considering this drift in the mean thrust measurements there are some important facts to consider:

- Both the instantaneous and mean forces that are being measured are small and they are at the lower end of what the data acquisitioning system is capable of measuring.
- The tests depicted in Figure 6-12 and Figure 6-13 are both 0.2 Hz tests, the lowest frequency that was tested with the correspondingly lowest mean thrust generated.

The question therefore becomes is there an excitation frequency above which the mean thrust start to converge towards a reliable value. This frequency, below which the mean force measurements were hard to obtain, seemed to vary between the tests. In case of the single flapper, the lowest frequency run that converges is the one at 0.3 Hz. Some of the other tests converged at a lower frequency as Figure 6-11 indicates.

In the end, it was therefore decided to perform all tests with 30 oscillations and a graph like the ones in Figure 6-10 to Figure 6-13 were closely examined for each test run to ensure that the effect of the noise was limited.

6.8 Initial results

In this section the preliminary results will be presented. This was before any frequency domain filtering or comparison with numerical methods had been done. Further results from the tests that became apparent only once the filtering and comparison had been done will be presented in the next chapters as this data might be considered more open to dispute.

The different tests done for this thesis can be divided in three. Eleven single flapper bollard pull runs were done before any of the other tests were performed. After confidence had been gained with this set of motions the bollard pull runs with a phase angle between the joints were commenced. Only after most of these runs had been completed did the forward speed runs begin as these were seen as the most complicated ones. In total 54 bollard pull runs with a phase angle were performed. These tests were done with oscillations of 30 or 40 degrees in the joints as earlier trials had shown smaller oscillations to be too jerky to render meaningful results. A

total of 53 tests were done with forward speed. These tests were done with 8 different motion patterns at various speeds.

6.8.1 Bollard pull (zero forward speed)

Ten different frequencies were performed of the 30-30-0 motion pattern to ensure that the generated thrust varied smoothly with excitation frequency. Results are shown in Figure 6-14. Note that negative thrust indicates forward force.

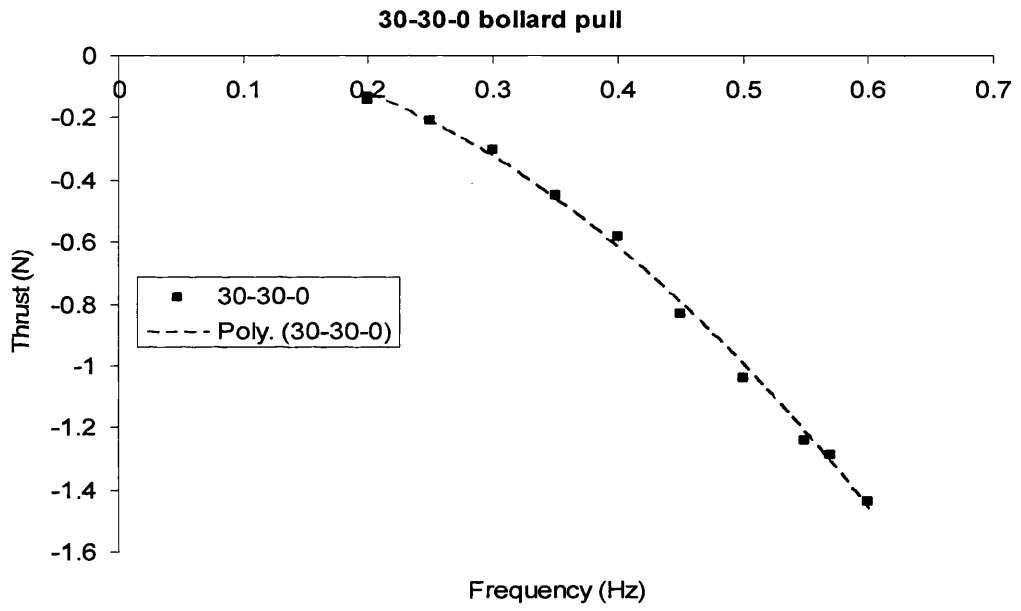

Figure 6-14: The variation in mean thrust with frequency for the single flapper

A similar set of tests were performed for the 30-40-60 motion pattern and for this pattern as well the bollard pull seemed to vary with a quadratic relationship of the excitation frequency. It might be less apparent from Figure 6-14 that the thrust for 0.2 Hz was tested twice. This was done partly to ensure repeatability and partially to investigate how low frequency noise components affected the lower frequency runs as discussed in section 6.7. The fact that the two data points appear as one in Figure 6-14 is a good indication of the limited influence of the noise on the average measurements.

An important input parameter to the design of an AUV based on the McEel concept is how many joints it requires. As a free swimming McEel would need to minimize the moment around its vertical axis it would probably need to make oscillations of at least one full wavelength. This means that the number of joints would be dictated by

the ideal phase angle between them. The larger the ideal phase angle between the joints the fewer joints would be required to make at least a full wavelength and the less complex the vehicle would be.

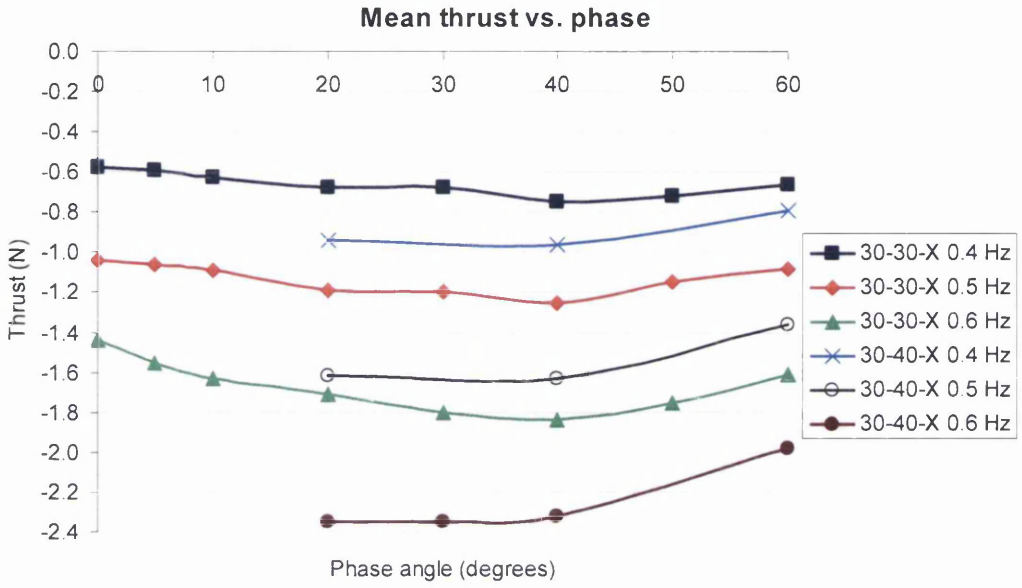

Figure 6-15: The thrust as a function of phase angle

Figure 6-15 shows how the mean thrust in the bollard pull condition varies as a function of the phase angle between the two joints for various excitation frequencies and motion patterns. Although the variations in thrust are mostly small, a phase angle of 30-40 degrees seems to produce the largest thrust for all of them. If this were the case also for eel-like structures with more than two joints, it would mean that a free-swimming mechanical eel would need 9-12 joints to produce maximum thrust in the bollard pull condition.

6.8.2 Forward speed

All the eight swimming patterns that were tested in forward speed had first been tested in the bollard pull condition. A value for the thrust with a forward speed of 0 m/s had thus been obtained. For each swimming pattern, 4-10 different forward speeds were then tested. The increasing speeds were selected to include some data for when the eel was held back by the towing tank carriage as well as some data for when the carriage was towing the eel.

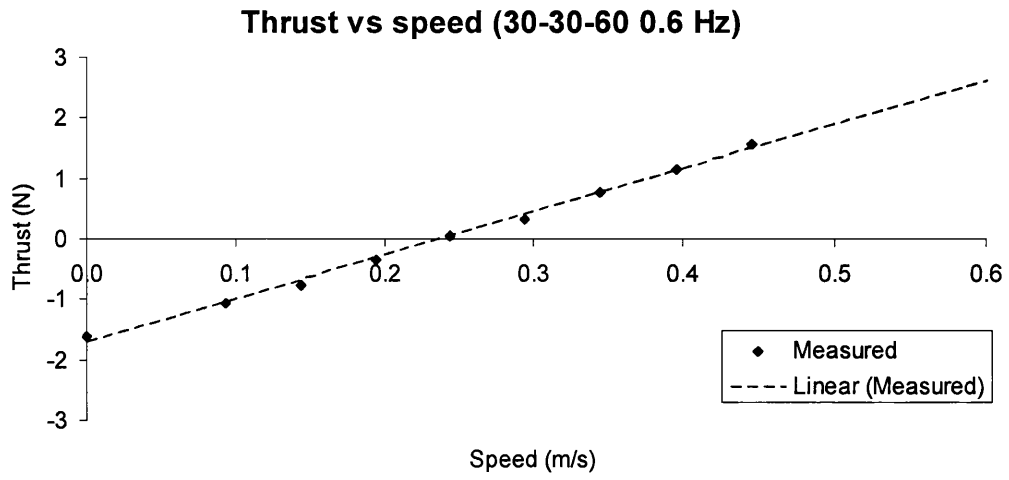

Figure 6-16: The measured thrust for various speeds for 30-30-60 0.6 Hz

In Figure 6-16, the measured thrust is plotted for various speeds. The linear approximation is plotted as a dashed line. The fact that the linear approximation is so close to the measured values is important, as the self-propulsion speed is one of the quantities of interest and as this is unlikely to coincide with a measured speed.

When examining the raw data from the forward speed runs with the McEel it is however important to remember that the self-propulsion speed is not the speed at which the mean total forward force is zero. This is due to the resistance of the sting and is depicted in Figure 6-5. A comparison of the different zero force speeds is however still of interest as it gives an indication as to which swimming style is the most efficient.

A plot like the one in Figure 6-16 was produced for each of the eight swimming scenarios and all the linear approximations fitted the data points well. The worst fit was for the lowest frequency tested. This was the 30-40-60 tested at 0.4 Hz:

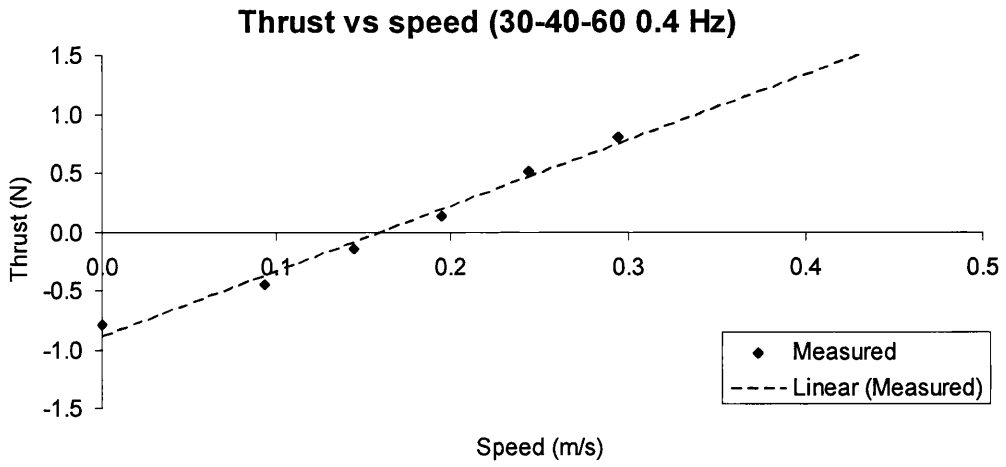

Figure 6-17: The measured thrust for various speeds for 30-40-60 0.4 Hz

Figure 6-17 shows the largest deviation from the linear approximation and has a Pearson product moment correlation coefficient squared of 0.984. The Pearson product moment correlation coefficient between an array x and array y is defined as:

$$R^2 = \left(\frac{\sum (x-\bar{x})(y-\bar{y})}{\sqrt{\sum (x-\bar{x})^2 \sum (y-\bar{y})^2}} \right)^2$$

Equation 6-2

As the measured data correlated quite well with their linear approximations, a comparison between the various computed zero forward force speeds could be shown. These speeds will be the ones where the linear approximation crosses the X-axis. The speeds at which the mean forward force was found to be zero are shown in Table 6.8-1:

Motion	Frequency (Hz)	U (m/s) when Fx=0
30-40-30	0.6	0.24
30-40-60	0.6	0.25
30-30-60	0.6	0.24
30-30-30	0.6	0.23
30-40-60	0.8	0.38
30-40-30	0.8	0.33

30-40-60	0.4	0.16
30-40-60	1.0	0.53

Table 6.8-1: The speeds at which the total mean forward force is zero

It is important to remember that each of the zero forward force speeds are computed on the basis of 5-10 test runs. Although there are differences between the different swimming styles, the zero total forward force speeds seems to be dependent primarily on over all excitation frequency.

7 Signal conditioning

7.1 Introduction

As mentioned in chapter 6 the raw data collected for the McEel contain a lot of noise. This noise seemed to be of both electrical and mechanical origin. Numerous attempts were made at minimizing these sources but in the end it had to be accepted that the poor signal to noise ratio was the best that could be obtained with the equipment available. Filtering and filter design therefore became an important part of this study.

This chapter therefore aims to explain the choices that were made regarding the filtering of the raw data. Amongst these choices were the decision to use a frequency domain filter, how many harmonics to allow through this filter, the decision to use a second pre-filter and the decisions regarding the implementation of this process of signal conditioning.

7.2 Frequency domain filtering

Initially it was attempted to filter the time dependent force signals with a higher order Butterworth filter. However, it soon became apparent that this would be impossible as the forces could be oscillating with a frequency as high as 4 Hz in extreme cases and the noise started around 3 Hz. Filtering in the time domain would thus be unable to discriminate between the noise and the signal. A plot of the frequencies present in the longitudinal force in an air test demonstrates this:

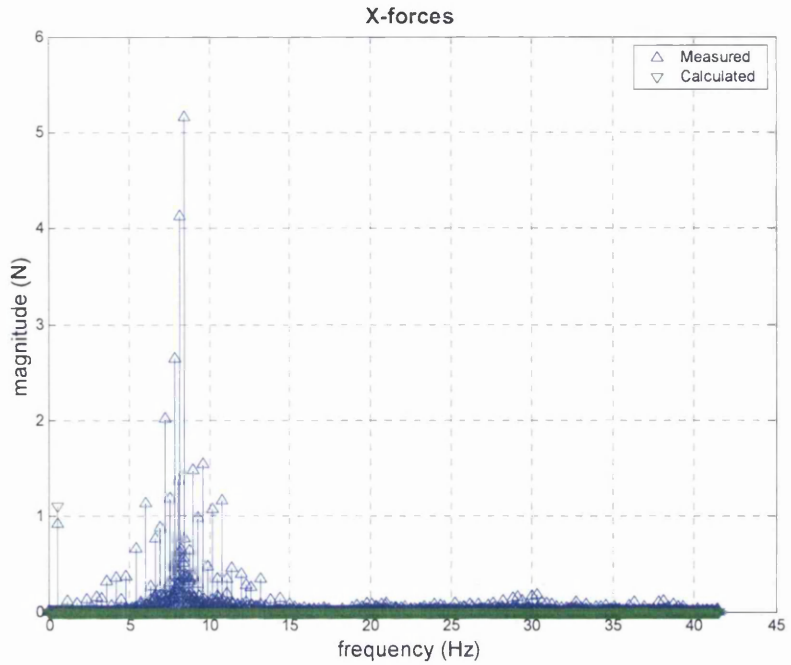

Figure 7-1: The signal to noise ratio for 40-40-0 0.3 Hz in air

Figure 7-1 is the frequency spectrum for the 40-40-0 0.3 Hz test in air. The blue stems with the upward triangles represent the measured signal whilst the green stems with the downward triangles represent the force calculated by the use of Newton's laws of motion.

The sampling frequency in Figure 7-1 is 83 Hz as it was in the earlier tests. This frequency was chosen as it is of sufficient size to give accuracy in the time domain without being so large as to render the data files unwieldy. This frequency is also a prime number and this should limit any interference from the mains frequency or other known noise. The tests performed in air as well as the earlier tests were sampled at this frequency. As fast Fourier analysis became an ever more integral part of this study though a higher sampling frequency and thus higher resolution was desired. In practical terms, a new data collection system allowing the use of a USB memory stick for data transfer rather than 3.5" floppy disks made the resultant bigger data files less of an issue. All the hydrodynamic tests presented in this study were therefore sampled at 213 Hz. This number was considered big enough to limit the effect of it not being a prime number.

Two conclusions can be drawn from Figure 7-1: there is a need for heavy filtering but the risk of aliasing is negligible as the data that is of interest is located far below

the Nyquist frequency. It was therefore decided to filter the forces in the frequency domain by the use of fast Fourier analysis.

7.3 Choice of harmonics to be included

As with all kinds of filtering, the outmost care has to be shown when employing frequency domain filtering so that the filter does not filter out something that is actually part of the signal. This is doubly true when filtering in the frequency domain as the whole process pre-supposes that the exact frequencies of interest are known a priori. In terms of the eel though it is fair to assume that the over-all force in the transverse direction will oscillate either at the same frequency as the over all excitations of the eel or at higher harmonics of this frequency. This is because an eel swinging towards the left should develop an equal but opposite transverse force to an eel swinging to the right. The opposite is true in the longitudinal direction. An eel swinging to the right should develop the same force in the X-direction as one swinging to the left. The force signal in the X-direction should therefore consist of oscillations at twice the frequency of the over-all excitations and higher harmonics of this frequency. In addition, the signal in the X-direction should contain a component at 0 Hz if the eel actually swims.

The question therefore becomes how many harmonics should be allowed to pass through the frequency domain filter. In answering this, it may be helpful to remember the physical set up of the McEel experiments:

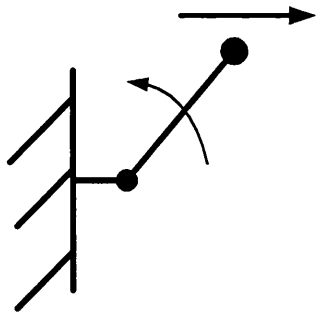

Figure 7-2: Determining how many harmonics to include

In Figure 7-2, it is shown how the over all excitations of the total system relate to the measured forces in the longitudinal direction. Shown here is a scenario with just one segment or with the two segments moving in unison. The angle in the joint would be:

$$\theta = A\sin(2\pi f t)$$

Equation 7-1

In this equation A would be the amplitude of oscillation, f the frequency of oscillation and t the time. From Equation 4-3 the acceleration in the longitudinal direction of any point along the segment can then be found:

$$\ddot{x} = Al4\pi^2 f^2\left(\sin(2\pi f t)\sin\left(A\sin(2\pi f t)\right) - A\cos^2(2\pi f t)\cos\left(A\sin(2\pi f t)\right)\right)$$

Equation 7-2

In this equation l is the length from the joint to the point on the segment that is of interest. This equation is for the acceleration of a point along the single segment in the longitudinal direction and as such, it dictates which harmonics should be present in the force signal when the McEel oscillates without a phase difference between the joints in air. Equation 7-2 consists of many elements and it is not immediately obvious how many harmonics would be present in the resulting force signal. Closer inspection using fast Fourier transformation reveals that the resultant force can be represented with only two frequencies.

If the McEel was tested in air with a phase angle between the two joints, the resultant force in the longitudinal direction should still contain only two frequencies. Once submerged, this can no longer be easily ascertained. The shape of the curve of the time history of the hydrodynamic forces that the McEel will develop is one of the fundamental questions that this thesis aims to answer and before good measurements are obtained it can not be decided how many harmonics should be present in the measured signal. This is presents a dilemma, as until it can be decided how many harmonics should be present in the measured signal good measurements cannot be obtained. If the Morison Equation is assumed to represent the true forces generated by the McEel's motions it can be shown that the longitudinal force should contain two harmonics and a signal at 0 Hz. Under the same assumptions, the transverse force should contain three harmonics.

As Figure 7-1 indicates, the measured signal in both directions, both in air and in water, did display several harmonics as well as 0 Hz values. In air, the general acceptance of Newton's laws of motion allows a decision to be made about which part of the signal to include whilst in water this is not the case. The higher harmonics can just as well be due to some hydrodynamic phenomena as noises in the test rig and the 0 Hz signal in the transverse direction can be due to the McEel being less than perfectly symmetrical. Unfortunately, the higher harmonics are not always smaller than the lower ones. There is thus a real danger that limiting the analysis to lower harmonics and the 0 Hz signal will exclude certain hydrodynamic effects. On the other hand, the poor signal to noise ratio dictates frequency domain filtering and as the third harmonic proved dubious even in air, it was decided to include just the first two harmonics and the 0 Hz signal for both directions for all tests in this thesis.

This means that if the McEel was tested at 0.3 Hz, it is assumed that the measured force in the transverse direction could at the most contain three signals at 0, 0.3 and 0.9 Hz. In the same test, the longitudinal force could at the most contain signals at 0, 0.6 and 1.2 Hz. A zero Hz signal in the transverse direction would equate to the McEel swimming sideways. It was allowed to pass through the filter, as anything bigger than a miniscule value in this signal would act as a warning.

7.4 The addition of a pre-filter

During testing the LMC-6524-1000N load cell was connected to a set of DSA-100 bridge amplifiers (for data sheets see Appendix E). Figure 7-3 shows how the measured signals were routed through the data acquisition system.

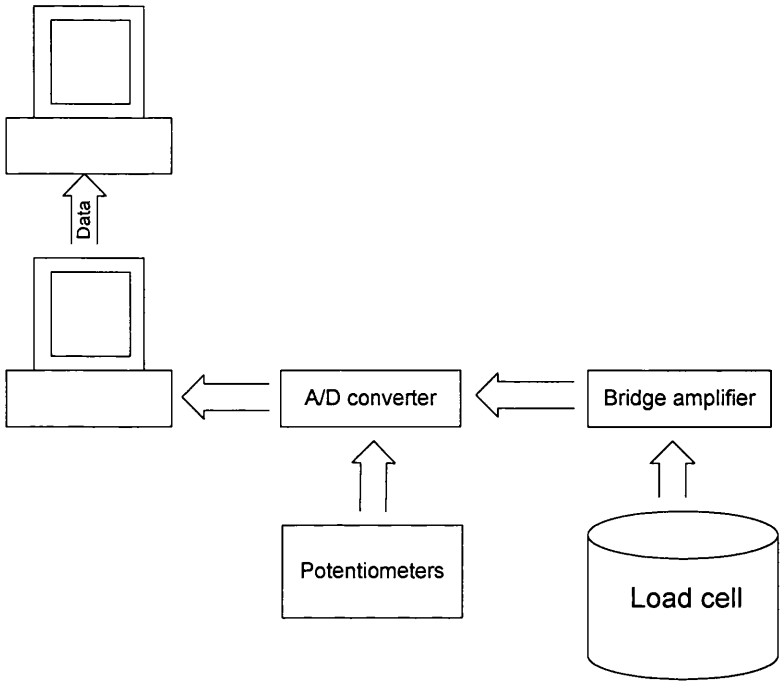

Figure 7-3: Block diagram of the routing of the measured data

These bridge amplifiers are fitted with filters with various settings. As the measured signal contained a lot of high frequency noise it was decided to eliminate some of this with the filters in the bridge amplifiers. As Figure 7-3 indicates this presents a new problem as angular position signals from the potentiometers did not pass through the bridge amplifier. The phase and amplitude shift through the filters therefore had to be quantified and either subtracted from the filtered signal or added to the signal from the potentiometers. In the literature accompanying the DSA-100 the filters are described as second order "vessel" filters. It was assumed that this was a typing or translating error and that the filters were Bessel filters. The filters were set for a cut off frequency of 10 Hz. The comparison with a second order theoretical Bessel filter with this cut off frequency is therefore presented in Figure 7-4 and Figure 7-5.

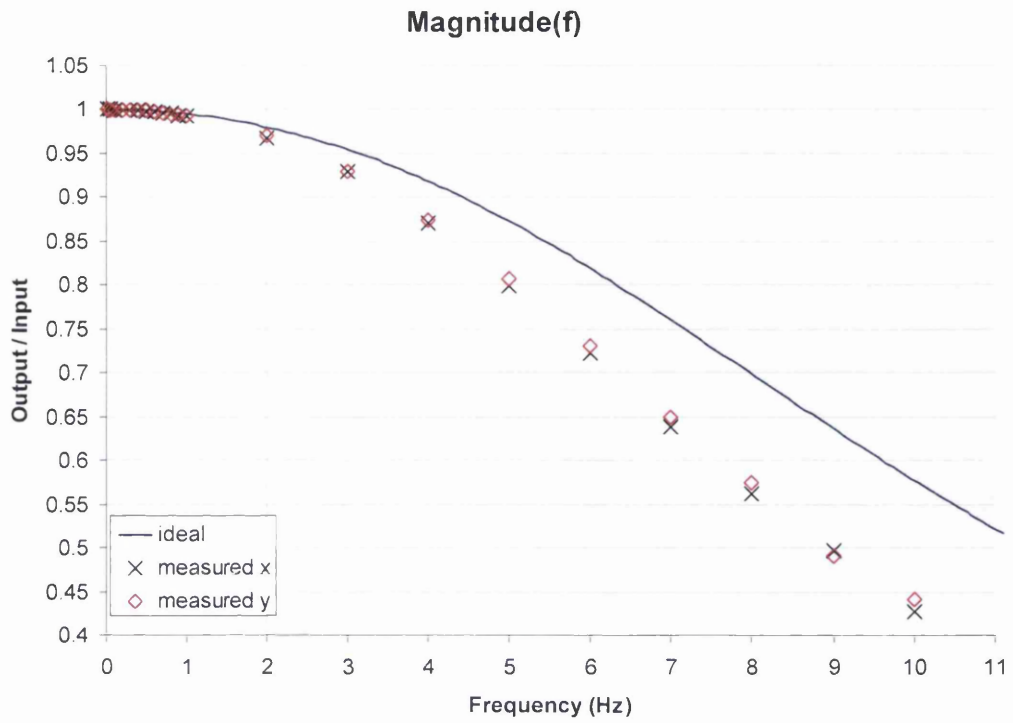

Figure 7-4: The magnitude response of the bridge amplifiers

The theoretical Bessel filter is indicated with a solid blue line.

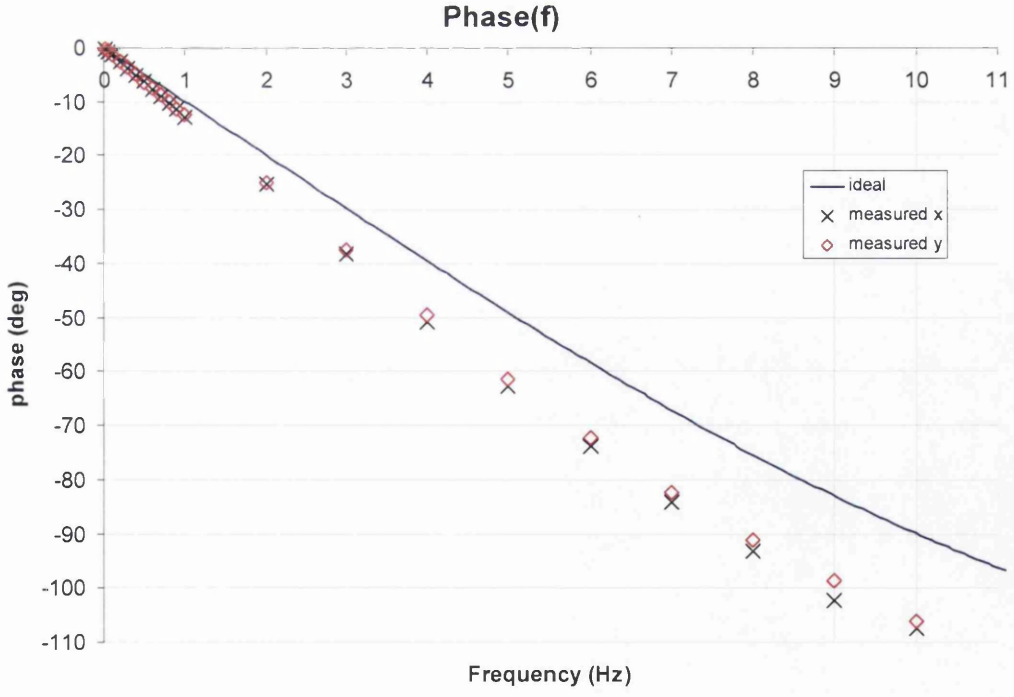

Figure 7-5: The phase response of the bridge amplifiers

As can be seen from these graphs the filter for the X-direction had a fairly similar response to the one for the Y-direction. They both varied considerably from the theoretical value though. In fact they were similar to a second order Bessel filter with a cut off frequency closer to 8 Hz.

Once the characteristics of the filters had been established it had to be decided whether the angular measurements should be modified in a similar way or whether these effects should be subtracted from the force measurements. In the end it was decided to do the latter as it was decided that this would relate the experiments better to real effects like the resistance of the eel and the sting.

7.5 Filter implementation

It was always intended to do as much of the analysis on the raw data as possible and only use the filtered data for comparisons with computed results. The original data processing model is shown in Figure 7-6

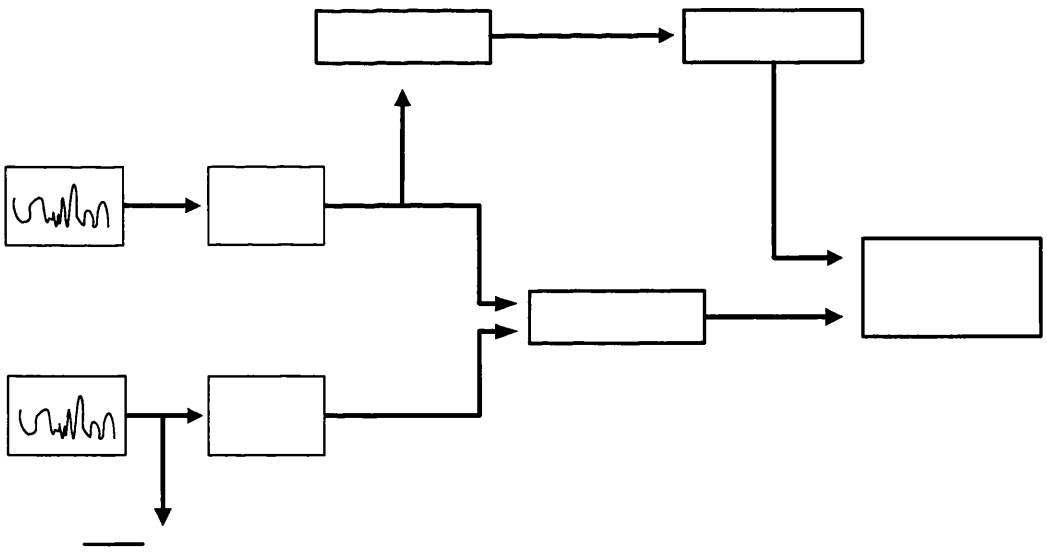

Figure 7-6: Block diagram illustrating the initial process of analysis

This figure shows how the raw data was processed whilst the old data acquisition system was still being used. Figure 7-6 is a representation of how this was done using the transverse forces to evaluate the force coefficients. This latter point will be discussed in section 8.5.

This method of processing the raw data would have meant that both the mean forward thrust and the computed force coefficients would have been un-affected by the frequency domain filtering. With the addition of the pre-filter, the phase and magnitude shift introduced by this filter meant that this no longer could be achieved. A modified model is illustrated in Figure 7-7.

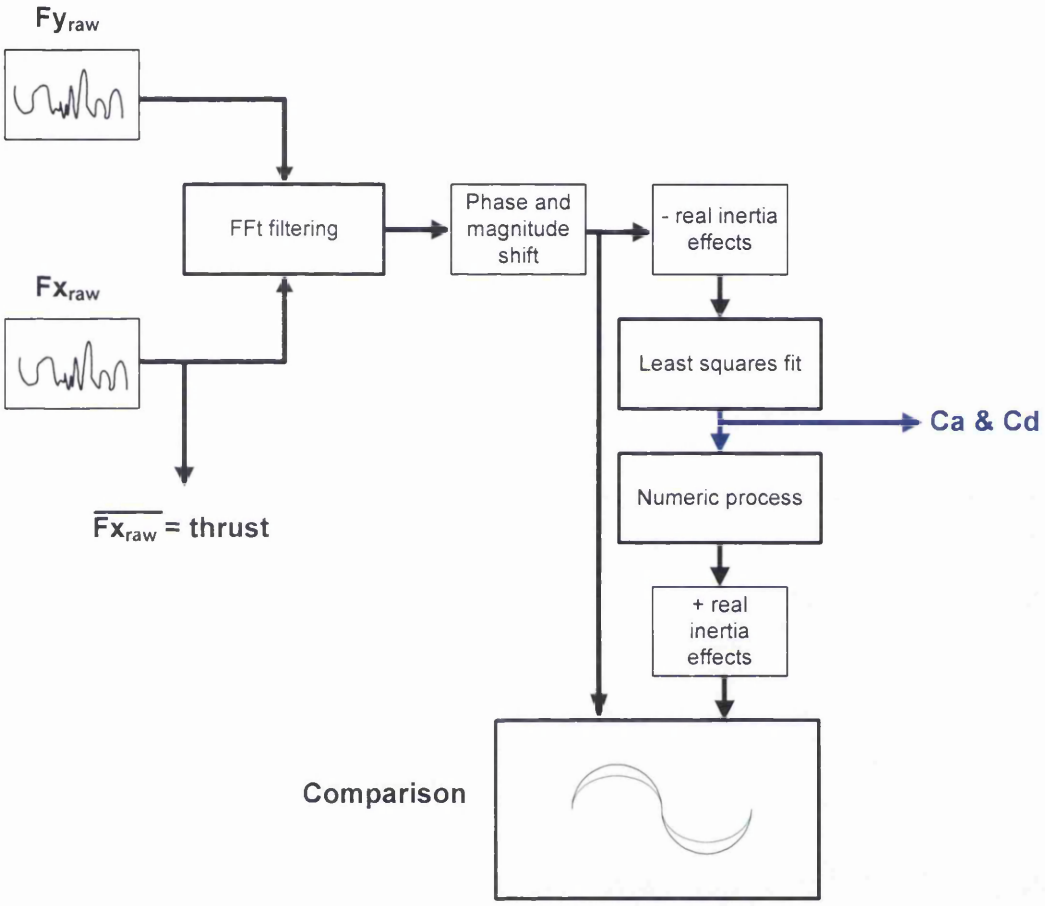

Figure 7-7: Block diagram illustrating the final process of analysis

In this figure, the force signals that are denoted as Fy_{raw} and Fx_{raw} are the ones coming from the pre-filter. Although this new method of signal processing adds several processes and thus several potential sources of error compared to the one described in Figure 7-6 it does also offer one major advantage. Without the pre-filter, the raw data measured bore little resemblance to the frequency-filtered data. Visual checks for obvious errors like sign convention were therefore impossible. The new "raw data", as shown in Figure 7-8, does however indicate that no such errors exist.

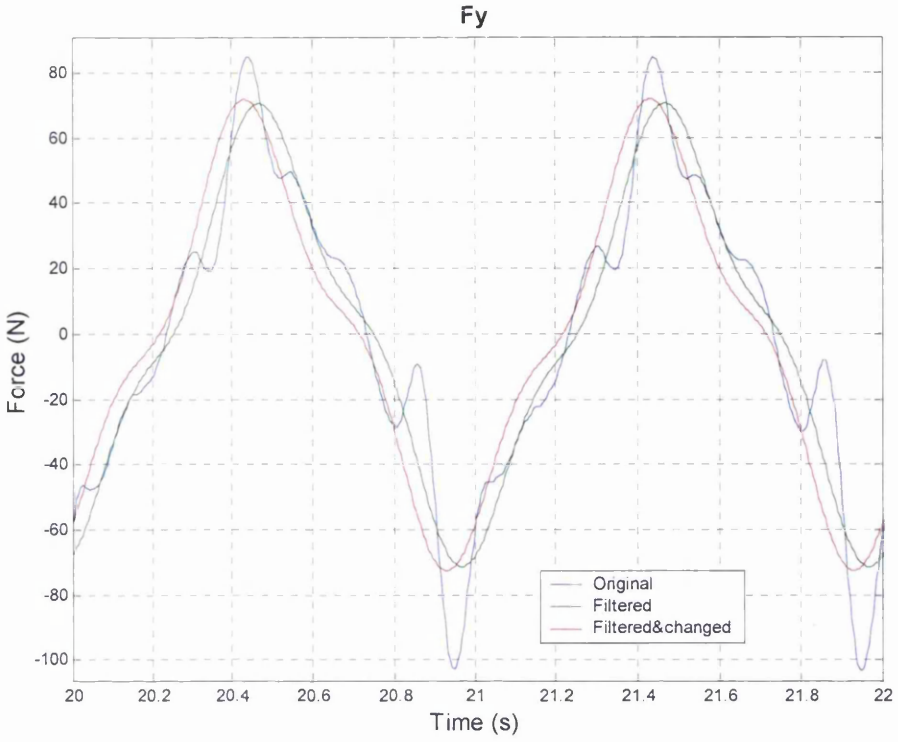

Figure 7-8: The phase and amplitude change caused by the filters in the transverse direction

In this graph, three force plots are shown relating to the transverse force for the 30-40-60 bollard pull condition with an excitation frequency of 1 Hz. The blue line is the raw data from the pre-filter. The green line is the frequency-filtered version of this signal. The slightly bigger and slightly earlier red line indicates the signal once the effects of the pre-filter have been removed.

The similar graph for the longitudinal direction, shown in Figure 7-9 is noisier.

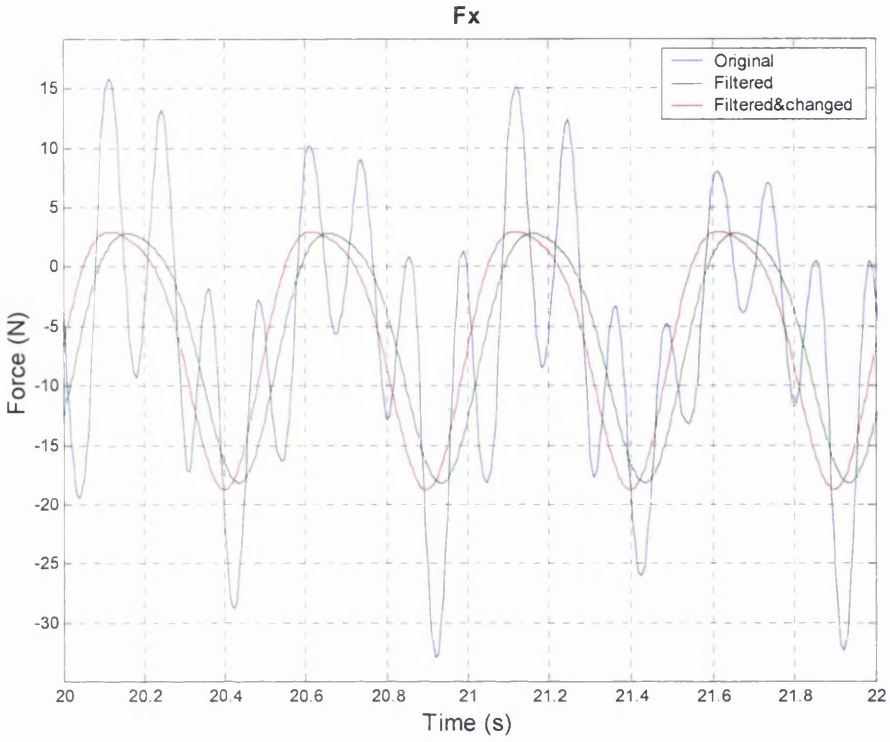

Figure 7-9: The phase and amplitude change caused by the filters in the longitudinal direction

As the generated forces in the longitudinal direction are of smaller amplitude, the noise is more distorting. The frequency-filtered signals still resemble the signal coming from the pre-filter though. The term noise is therefore used to describe both mechanical vibrations and electrical noise.

Once the process for filtering the signals had been established the measured forces could be compared to the computed forces. This will be shown in chapter 8 and 9.

8 The single flapper bollard pull tests

8.1 Introduction

As described in section 2.2 the scenarios in which the two segments move in unison are referred to as single flapper scenarios. Only eleven of these tests were performed as they had been found to match the theories well during preliminary tests in 2003 and 2004. All the single flapper tests reported in this text are of the 30-30-0 variety. This was done to ensure that any variation in force was smooth with increasing frequency.

These were the most basic hydrodynamic tests and as such, they were used to gain confidence in the experimental method as well as answer some of the fundamental questions. The questions that these tests were specifically used to answer was:

- How important is the tangential added mass force?
- To which force(s) should the least squares fit be applied and how should it be applied?
- Is the measured data best replicated with constant or varying force coefficients (see section 3.5)?

Before these questions can be answered, the application of the Morison Equation to a single flapper has to be examined. The physical aspects of the McEel that only became important during testing also have to be explored.

8.2 The Morison Equation for a single flapper

The Morison equation deals with cross flow and although it is often used for non-perpendicular flow there seems to be no general agreement about the exact angle at which its predictions become inaccurate. The decision to start testing the McEel as a single flapper was therefore influenced by the notion that such a set up would render a pure cross flow. The limitations of the Morison Equation were therefore believed to be less important in this scenario than in others and it was considered as a natural first step towards a simple numeric method for a free-swimming eel.

It was thus hoped that the flow encountered in the single flapper, zero forward speed scenario would align itself with the normal vector from Equation 4-16. As seen in section 2.2 this was not the case. In mathematical terms, this would have meant that:

$$\vec{V}_i = const.\vec{N}_i$$

Equation 8-1

Equally:

$$\vec{A}_i = const.\vec{N}_i$$

Equation 8-2

These two equations would have to hold true for all points along the single flapper at any time for this to be a pure cross flow problem. For the velocity vector, this is not a problem as:

$$\vec{\mathbf{V}}_i = l\left(-\dot{\theta}\sin\theta, \dot{\theta}\cos\theta\right)$$

Equation 8-3

This expression comes from Equation 4-2. l is the length along the eel from the pivot point and although the angular velocity is a function of time, it can be factored out of the expression satisfying Equation 8-1 at any given time. The similar expression for the acceleration vector would be:

$$\vec{\mathbf{A}}_i = l\left(-\ddot{\theta}\sin\theta - \dot{\theta}^2\cos\theta, \ddot{\theta}\cos\theta - \dot{\theta}^2\sin\theta\right)$$

Equation 8-4

It is clear from the equation that even a single flapper with zero forward speed does not encounter pure cross flow as far as the inertia forces are concerned. It is however important to emphasise that the only way of getting closer to a perpendicular flow would be to have non-harmonic over-all excitations of the eel.

The idea of testing single sections of the McEel in a pure cross flow was considered for a while. This would have been more consistent with the theory behind the Morison Equation and would have provided coefficients for the McEel that would have been comparable to published data. In the end, it was still decided to start the

testing with the zero forward speed single flapper though as initial tests proved this to be a flow regime sufficiently close to a pure cross flow for the Morison Equation to work.

8.3 Physical data of the McEel model

Most of the physical data relating to the McEel has already been quantified, as they were easily measurable. There were however some quantities that could only be estimated. This section therefore explains how the real mass of each segment was measured and how this relates to the water ballast of each of the segments.

To enable an accurate prediction of the real mass effects of the McEel it was disassembled and the masses of the two moving segments were accurately weighed. The centre of gravity was then found by balancing each segment on a metal edge:

Segment	Real mass (kg)	Centroid (m)
Mid	2.177	0.082
Tail	1.775	0.054

Table 8.3-1: The mass and centre of gravity of each segment

In Table 8.3-1, the centroids are measured from the front joint of the segment in question. Included in the real mass are the pulley wheels including the free wheel in the mid segment as depicted in Figure 5-8 but not the masses of the timing belts as this was considered negligible. One additional question considered was whether the rotational inertia of the pulley wheel would have to be included in addition to its translational inertia. Looking back to Figure 5-3 again and remembering that it is the force measured by the load cell located above the motors that is of interest, it is apparent that no such rotational effects should be included. To justify this, Figure 8-1 is presented:

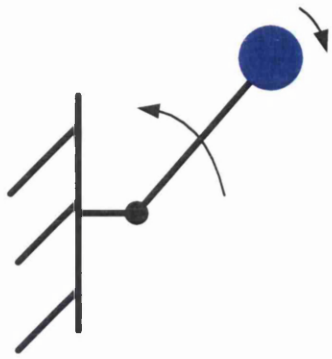

Figure 8-1: The effect of the pulley wheel on the force measurements

In this figure, the pulley wheel is depicted in blue at the tail end of the segment. The angular motions of the segment are denoted A and the rotational motion of the free wheel is denoted B. From this figure, it should be evident that independent on how the motions of A are, any motions in B will contribute or counteract the motions in A depending on which way the two bodies rotate. It should however also be evident that the forces generated by the rotational motions B should not contribute to global translational forces in point C as long as the free wheel is symmetric. The rotations of the free wheel are thus of importance when calculating the power that goes into the system of the McEel but are irrelevant when the overall forces in the global X- and Y-direction are to be computed.

The central piece of each of the McEel's segments was made up of two pieces of channel sections making a 102*102 mm (4"*4") square cross section. Unfortunately, there were substantial void spaces inside this box that filled up with water and acted as ballast tanks as the eel was submerged. At the same time, the timing belts that were moving the McEel needed these void spaces. The real inertia forces of the entire system had to be subtracted from the measured forces before the hydrodynamic forces from the numeric model could be compared to the measured ones. The mass and centre of gravity of this ballast water therefore had to be estimated:

Segment	Ballast (kg)	Centroid (m)
Mid	0.734	0.09
Tail	0.490	0.07

Table 8.3-2: The mass and centre of gravity of the ballast water

As can be seen the mass of this ballast water was about a third of the real mass of each of the two moving segments (see Table 8.3-1). Ideally, the McEel should have been filled up with some sort of solid material to avoid having to estimate this ballast water. No practical solution to this problem was found within the budgetary constraints though.

8.4 The tangential added mass force

Although the single flapper tests contained tangential acceleration vectors, they contained no tangential velocity vectors. These tests were thus perfectly suited to evaluate the importance of the tangential added mass forces. To examine the importance of the tangential added mass forces a typical plot of the time history of a single flapper test is depicted below:

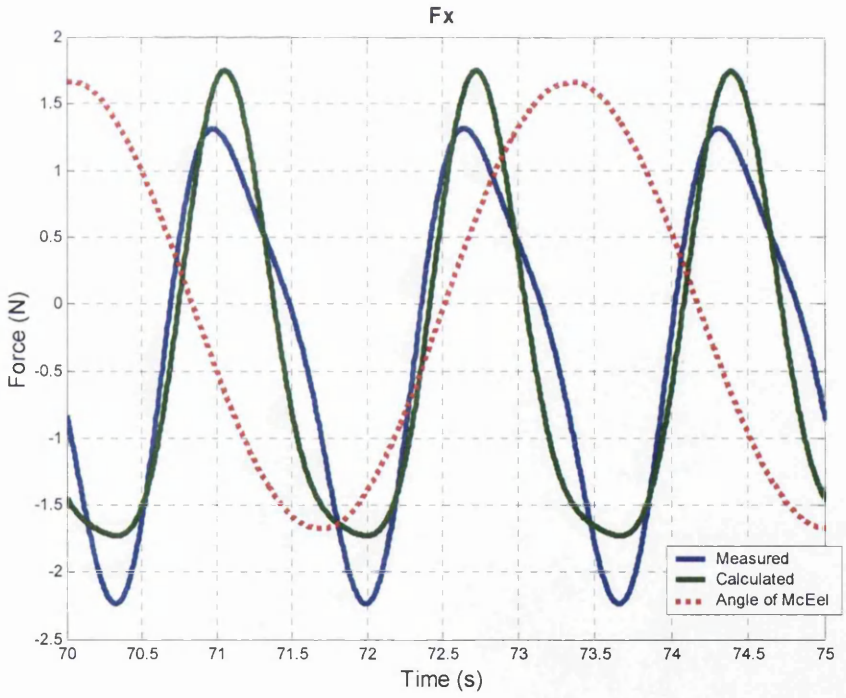

Figure 8-2: A typical force plot, longitudinal direction

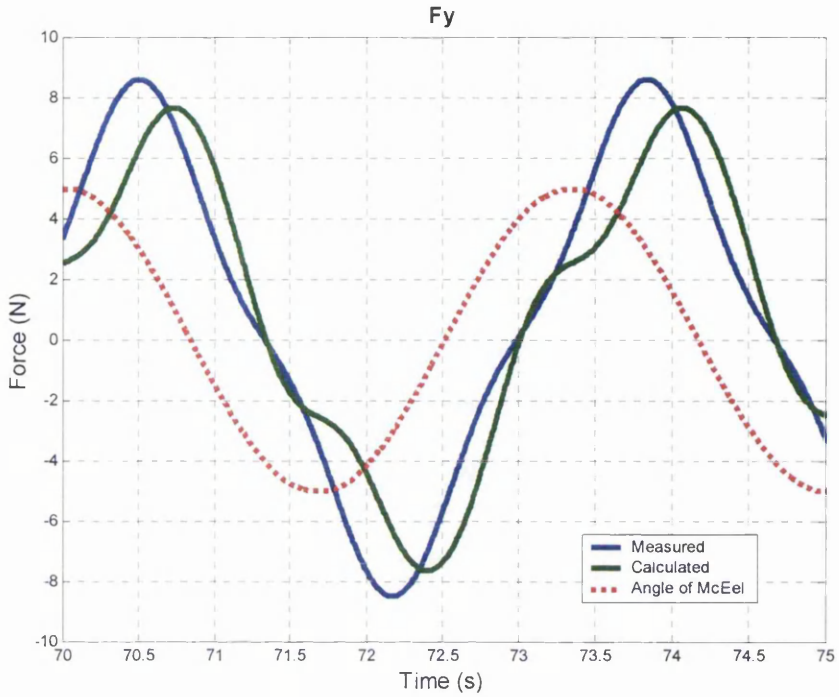

Figure 8-3: A typical force plot, transverse direction

This is the test with a 0.3 Hz over all excitation frequency and 30 degrees amplitude in both joints. The red dashed line represents the angle of the first joint to give some indication as to where in the cycle the thrust is produced. It is important to emphasize though that this angle is drawn to an independent scale to fit the same graph better. The data for the computed solution are as follows:

		Mean Fx	
Ca	Cd	Computed (N)	Measured (N)
0.37	**4.45**	**-0.4**	**-0.3**

Table 8.4-1: The values from Figure 8-2 and Figure 8-3

These force coefficients were typical values as will be shown in section 8.5.

Figure 8-3 is mainly presented for reference purposes but Figure 8-2 shows several important points. In it can be seen how the time histories differ in several aspects. The amplitudes of the oscillating force and the predicted force are not that different but the shape of the signal is. It would be tempting to postulate that this is due to the tangential inertia forces not being included but Figure 8-2 does not support this. As can be seen the two signals are the most similar when the eel passes through zero

degrees and they differ the most when the eel is at its extreme angle. This would indicate that the tangential added mass effects are negligible. The idea of including a tangential added mass effect using a tangential added mass coefficient was therefore abandoned. It would be tempting though, to suggest that what the Morison Equation lacks in its attempt to predict this flow phenomenon is a term dealing with vortex shedding. This is also supported by the observation of surface vortices during this experiment.

8.5 The calculation of the Morison Equation coefficients

As mentioned in chapter 1 the nature of study presented in this thesis is more complicated than the comparison of a measured result with a predicted one. This is because the numeric methods all depend on various force coefficients that are not known in advance. The plan was therefore to measure the forces from the physical tests and calculate force coefficients from this set of data. The obvious question therefore becomes why bother to construct a numeric method to compute forces that have already been measured? The answer to this is that through this thesis it is hoped that force coefficients, which will be applicable also to other, untested motions or indeed other eel-like propulsion devices, can be found. It is thus of interest to see how the force coefficients vary from test to test. Consequently, it is necessary to establish a suitable procedure for evaluating these force coefficients. Two issues have to be resolved to do this. It has to be decided whether longitudinal, transverse or both sets of forces should be used, and it has to be decided if the force coefficients should be fitted for all the tests together or whether an average value of coefficients obtained from separate tests should be used.

8.5.1 Selection of forces for least squares fit

The forces generated by the eel are measured in both the longitudinal and transverse direction as described in chapter 5.5. For each test, there are therefore in essence two sets of results. The eel will be at varying angles to the global coordinate system at different times throughout its cycle and this will be reflected in the measured force in the global X- and Y-direction. The coefficients of drag and added mass should

however be the same whether they contribute to a force in the global X- or the global Y-direction. If not the concepts behind them would be faulty. Inherent in these tests there is thus a possibility to use the calculated force coefficients from one direction to verify the measured force in the other. Three alternatives thus exist:

- Computing the coefficients from the transverse force and verifying it against the longitudinal force
- Computing the coefficients from the longitudinal force and verifying it against the transverse force
- Computing the coefficients on the basis of both the longitudinal and transverse force measurements and verifying it against both of them

As the overall thrust of the eel is the one of primary concern it might be tempting to use the X-direction to calculate the coefficients as one would assume that this would lead to a higher level of accuracy in the X-direction. At the same time though the forces in the Y-direction are bigger and thus contribute more to the moment required in the joints and is therefore more important for the estimation of power required to move the eel. The force in the Y-direction is also substantially larger than the force in the X-direction and minor errors in measurement are thus less important. Closer inspection of initial tests also showed that the force predictions were more accurate in the Y-direction in air. The argument about greater overall forces in this direction also holds true in air but the deviation could also be due to different stiffness of the test rig in the two directions and other challenges associated with the test set up.

When attempting to minimise the error between a measured and a computed force signal by adjusting the force coefficients it is common to use the method of least squares fit. If the Morison equation is assumed the hydrodynamic force in either direction can be expressed as:

$$f = AC_a + BC_D$$

Equation 8-5

In this expression A and B can be seen as constants for determining the force coefficients of the Morison Equation. The square of the error between the measured force (fm) and this computed force can now be expressed as:

$$e^2 = (fm - f(A,B))^2$$

Equation 8-6

To find the minimal error this expression can be differentiated, leading to:

$$\frac{\partial e^2}{\partial C_a} = 2Afm - 2A^2C_a - 2ABC_D = 0$$
$$\frac{\partial e^2}{\partial C_D} = 2Bfm - 2ABC_a - 2B^2C_D = 0$$
$$\Downarrow$$
$$\begin{bmatrix} A^2 & AB \\ AB & B^2 \end{bmatrix}\begin{bmatrix} C_a \\ C_D \end{bmatrix} = \begin{bmatrix} Afm \\ Bfm \end{bmatrix}$$

Equation 8-7

This expression is easily solvable and it should give the right result even with a noisy signal, as the noise will be randomly distributed. This is of course only strictly true if the signal is infinitely long. For this reason, Ca and Cd were evaluated over the entire length of the test data. It is important to emphasize that although this was shown for the normal Morison equation it would be equally true if Ca and Cd were dependent on Kc. The Ca and Cd in the formulae would then simply represent the constant coefficient of these two force coefficients.

This method of least squares fit assigns the same significance to data points for which the measured value is close to zero as it does to data points with a larger absolute value. From an engineering point of view, this might not be ideal, as the percentage error is the one of interest. Sarpkaya (Sarpkaya and Isacson 1981) has therefore suggested this form of error function:

$$e^2 = fm^2(fm - f(A,B))^2$$

Equation 8-8

This method is not ideal for a noisy signal though as it gives higher importance to data points that might only have a high absolute value due to noise. One way of getting around this problem would be to filter the signal first. The problem involved with all filtering though is that one has to be certain what part of the measured signal is meant to be there and what part is just noise. Despite these challenges Sarpkaya's method for minimizing the error was tried but was found to yield a higher r.m.s. error between the measured and calculated signals and the original least squares fit method was therefore preferred when trying to extract the hydrodynamic force coefficients.

If the forces in both the longitudinal and transverse direction were to be used for the evaluation of the hydrodynamic force coefficients Equation 8-6 would become:

$$\sum e^2 = k(fxm - fx(A,B))^2 + (fym - fy(C,D))^2$$

Equation 8-9

This is an expression of a combined error in both the X- and Y-direction. The magnitude of the forces in the two directions are however very different and if errors in both of them are to be assigned the same importance a constant k needs to be employed. This k therefore represents the amplitude of oscillations in the measured Y-force divided by the amplitude of oscillations in the measured X-force all squared. If no such constant were included in Equation 8-9 the coefficients would be computed based on the forces in the transverse direction only as these forces are so much larger. To find the minimal error Equation 8-9 can also be differentiated, leading to:

$$\frac{\partial \sum e^2}{\partial C_a} = 2Akfxm - 2A^2kC_a - 2ABkC_D + 2Cfym - 2C^2C_a - 2CDC_D = 0$$

$$\frac{\partial \sum e^2}{\partial C_D} = 2Bkfxm - 2ABkC_a - 2B^2kC_D + 2Dfym - 2CDC_a - 2D^2C_D = 0$$

$$\Downarrow$$

$$\begin{bmatrix} A^2k + C^2 & ABk + CD \\ ABk + CD & B^2k + D^2 \end{bmatrix} \begin{bmatrix} C_a \\ C_D \end{bmatrix} = \begin{bmatrix} Akfxm + Cfym \\ Bkfxm + Dfym \end{bmatrix}$$

Equation 8-10

This matrix expression is more complex in its components but can be solved just as easily as the one in Equation 8-7.

8.5.2 Fitting of multiple data sets

Now that the direction to be used for the least squares fit has been discussed the issue of whether to compute the force coefficients as an average or in one process can be examined. The two methods can be described as follows:

- Use the least squares fit on the individual runs and thus calculate force coefficients for each of them. Obtain the average value (in some appropriate sense) of these separate force coefficients and then use this value when computing the numeric force signals.
- Combine all the runs into one long time series and compute the least squares fit for this data finding the coefficients directly.

Both of these methods have advantages and disadvantages. The main advantage of the method using average values of coefficients fitted separately for each run is that this method is less computational intensive as the computations are split up. This method is also more flexible in that new measurements can be added to the existing ones without having to recalculate the least squares fit. The method in which one least squares fit is computed for the entire data set should however produce a better over-all fit. As mentioned in section 7.2, all hydrodynamic tests in this study were measured with a sampling rate of 213 Hz. For the bollard pull tests the physical McEel was set to perform 30 oscillations for all but one test run (the one exception was performed to verify that 30 oscillations was adequate, see section 6.7). The lower frequency runs thus contain more data points than the higher frequency ones. In the computation of one least squares fit for all the runs higher significance will therefore be assigned to these low frequency runs, which could skew the result. This problem could be addressed by a weighting technique.

8.5.3 The force coefficients matrix

There is thus a 2 by 3 matrix of ways to compute the force coefficients. The single flapper bollard pull tests are well suited to determine which one of these options produce the best result as section 8.4 showed that there are only two force coefficients that need to be determined.

However, various criteria can be used in determining which computational method produces the best overall solution. The first one is the r.m.s. error in both x- and y-direction. The aim of this study is to predict the forces on a jointed oscillating structure. The time histories of the generated forces in both directions should therefore ideally be exact and the r.m.s. errors in both directions should be zero. The magnitude of these errors is therefore an indication as to how well the various methods can do this. The r.m.s errors can therefore be computed using the final (fitted) values of Ca and Cd.

The second criterion is the prediction of average thrust compared to the measured value. This can in some regards be seen as the most important criterion, as the initial desire was to predict the swimming speed of the mechanical eel.

The values for the added mass coefficient fitted for the various directions are presented in Table 8.5-1.

	Direction		
Method	X	Y	Both
Average	**0.28**	**0.88**	**0.38**
All in one	**0.27**	**0.87**	**0.37**

Table 8.5-1: The values for the added mass coefficient fitted for different directions

Similarly, the values for the drag coefficient fitted for the various directions are presented in Table 8.5-2.

	Direction		
Method	X	Y	Both

Average	**4.37**	**4.19**	**4.28**
All in one	**4.59**	**4.30**	**4.45**

Table 8.5-2: The values for the drag coefficient fitted for different directions

Table 8.5-1 show just how important the choice of method can be. The fact that simply applying different computational techniques to the same set of empirical data will yield different answers is an indication of the complexity of the problem. It is however important to emphasise that the fitting of the force coefficients is done under the assumption that the hydrodynamic forces can be predicted using the Morison Equation. It is however, a well-known fact that this formula omits several forces (see section 3.5).

Using the computed values of Cd and Ca the time histories of the longitudinal and transverse forces could be computed. These time histories could then be compared to the measured forces. This was done by calculating the r.m.s. difference between the measured and the computed signals. As the transverse forces were much larger in amplitude than the longitudinal ones this r.m.s error was divided by the r.m.s. of the measured signal so that the two directions could be compared to each other. These r.m.s. errors as proportions of the r.m.s. of the measured signals are presented in Table 8.5-3 and Table 8.5-4.

	Direction		
Method	X	Y	Both
Average	**0.37**	**0.67**	**0.39**
All in one	**0.38**	**0.66**	**0.38**

Table 8.5-3: The RMS error as proportion of RMS of measured signal in the longitudinal direction

	Direction		
Method	X	Y	Both
Average	**0.37**	**0.26**	**0.34**
All in one	**0.38**	**0.26**	**0.35**

Table 8.5-4: The RMS error as proportion of RMS of measured signal in the transverse direction

As can be expected the method calculating the coefficients using the transverse force produce a better fit in the transverse direction and vice versa. The method using both directions to estimate the coefficients also ends up between the two, as one would expect. The fact that the methods based on the longitudinal force seems to make equally good predictions in both directions is peculiar. No reason for this was found and it was considered a coincidence.

All the errors presented in Table 8.5-3 and Table 8.5-4 are large and this indicates that the Morison Equation is not particularly well suited to predict the instantaneous forces generated by the McEel. It is however important to emphasise that for initial design purposes the mean thrust is far more important than the instantaneous values.

When the mean predicted thrust was to be compared, the average force coefficients were used for the method based on the longitudinal force whilst the unified values were used for the force coefficients based on the other two. This was done as these three methods yielded the best predictions.

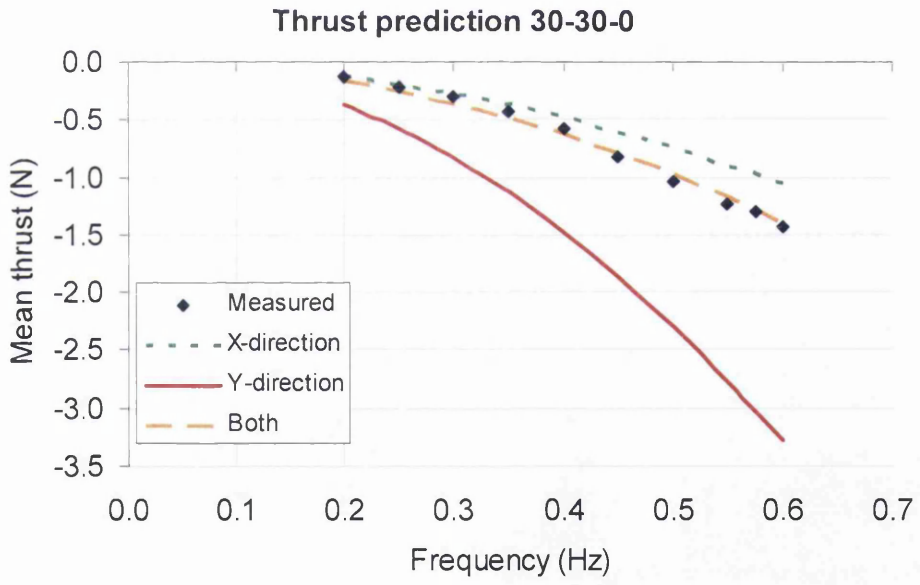

Figure 8-4: The mean thrust predictions for 30-30-0 for various frequencies

Figure 8-4 shows the measured and predicted mean thrust for the eleven 30-30-0 tests. Several key points can be deducted from this graph. Firstly the two methods employing only forces in one direction either consistently over-predict the mean thrust (for fitting based on Y-direction forces) or consistently under predict it (for fitting based on X-direction forces). This graph, Table 8.5-3 and Table 8.5-4 indicate that the forces in both directions should be taken into account when determining the

coefficients. When this approach is taken the accuracy of the fit to the mean thrust is far superior to the accuracy of fit of the instantaneous forces.

Furthermore, the expected trend that the mean thrust produced increases with the excitation frequency when the amplitude of the oscillations is kept constant is demonstrated for both measurements and predictions. This last point is only to be expected for these low frequencies but it is reassuring to see intuition confirmed by measured data.

In Table 8.5-3 and Table 8.5-4, it was shown how time histories based on the measured force in the transverse direction was marginally better in the Y-direction though substantially worse in the X-direction than those based on both sets of forces were. This coupled with the superior mean thrust predictions based on the two forces means that this method is preferred to the one based on transverse forces only. If one method had predicted the forces well in one direction and the other had predicted them well in the other this might not had been as obvious. Making an estimation of the power that goes into the system, both according to the numeric model and according to the measured forces is therefore an important comparison

The mean thrust generated by the eel is the output of this system. For design purposes it is however equally important to know the input, or power requirement of the system. Measuring the required power was not easy however as it was hard to quantify the mechanical losses with the available equipment. The overall forces in both directions were however known but the force distribution along the length of the eel was not. The moment in the joints could therefore not be computed outright. If however it was assumed that the force distribution from the Morison Equation was correct, even though the total force was not, then the moments in the joints and therefore the power requirement could be computed. This power is therefore based on measured forces but on computed distributions of force and as such, it will be denoted inferred power. This method of estimating the power input is less than ideal but the best one available. The power estimates will however mainly be used as a comparison between the different numeric models and the errors involved should be of similar order for all of them.

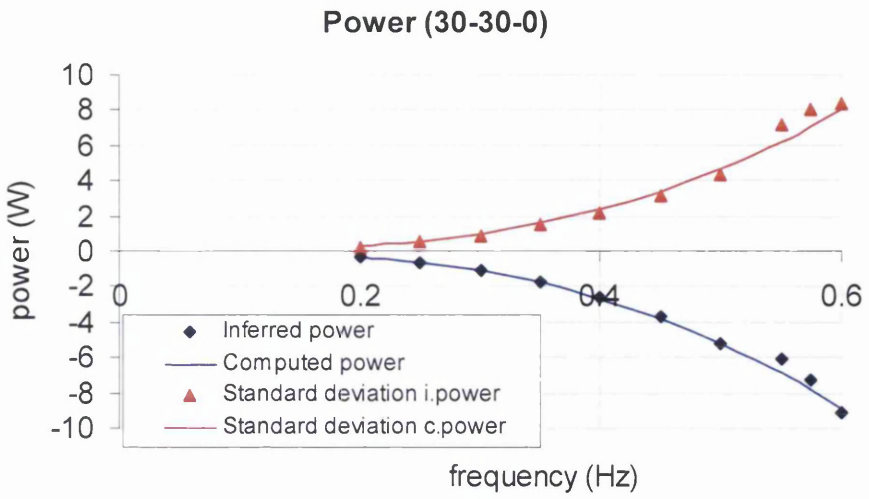

Figure 8-5: The power requirement, mean and standard deviation

Figure 8-5 depicts how the mean and the standard deviation of the power requirement vary with frequency. Power required to rotate the joints is defined as negative. This may go against the common convention but as a force moving the eel forward is defined as negative, it seems reasonable to follow the same convention. The close correlation between the measured and the computed values may be surprising. It indicates that the substantial errors in the time histories of the forces as predicted by the Morison Equation is of limited importance when it comes to computing the power requirements for the single flapper.

8.6 Keulegan-Carpenter dependent force coefficients

In section 8.5, it was shown how the force coefficients for the Morison Equation are best determined from test data from the McEel. A two by three matrix of possibilities was presented and it was shown that use of data for force in both directions and the adoption of a unified time series of all the runs produced the best result. When the constant parts of the Keulegan-Carpenter number varying force coefficients are to be determined, the same matrix of possibilities exists. The same method for determining which of these six possibilities render the best result was also used for this numeric method (Graham 1980). The conclusion was the same as in the case of the standard Morison Equation.

In addition, Graham mentions that although the drag coefficient theoretically should vary as a function of the Kc number raised to -1/3, empirical data suggests that raising it to -1/2 produces a better fit. Both of these values were therefore tested and as Graham suggests the variation between the two is negligible. It was therefore decided to use the -1/3 value suggested by Graham. The Morison Equation could thus be compared with its counterpart with Keulegan-Carpenter number varying coefficients.

In terms of the time-varying error between the measured and predicted forces, the methods produced the same accuracy. This can be seen in Table 8.6-1 where the ratio of the r.m.s. error to the r.m.s. of the measured signal is presented for the two methods.

Method:	Fx RMS	Fy RMS
Morison	**0.38**	**0.35**
Kc dependent	**0.38**	**0.35**

Table 8.6-1: The ratio of error to measured signal for the two methods

It may be surprising to see that the predictions from the standard Morison Equation are as good as those computed using Graham's method (Graham 1980). The Keulegan-Carpenter number varies from just over zero at the front joint to just over 100 at the tail in these trials and one might expect it to have a significant impact on the result. One limitation of these trials is however that only the over-all force experienced by the structure is measured. The original Morison Equation might thus give a good approximation of the total force even if Graham's method is better at predicting the forces as they occur along the length of the eel. It is not within the scope of this study to verify whether this is really the case.

It may be hard to visualize the time dependent error that the numbers in Table 8.6-1 represents. Figure 8-2 and Figure 8-3 are however typical time histories and as such may be used as reference.

The two methods also produce similar results for the predicted mean forward thrust of the single flapper. This is depicted in Figure 8-6.

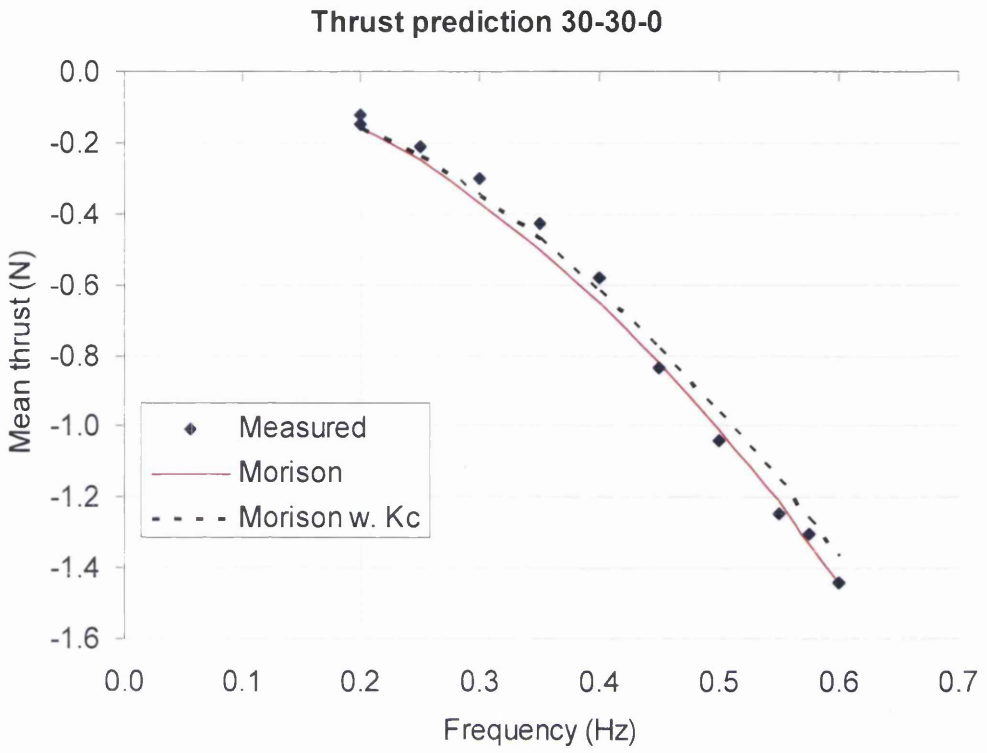

Figure 8-6: The mean force predictions from the two methods

In Figure 8-6, it can be seen that the method using Kc-number dependent coefficients predicts the low frequency runs better whilst the normal Morison Equation is better for the high frequency runs. The average error in the mean forward force prediction is 11% for both methods.

Figure 8-6 was produced with the following force coefficients (or constant part of them):

	Kc	No Kc
added mass	0.14	0.37
drag	7.47	4.45

Table 8.6-2: The force coefficients used

The values for the constant part of the drag coefficient and the constant part of the added mass coefficient in Graham's method are below both the theoretical values of 11.8 and 0.25 and the experimental values of 8.0 and 0.2 presented in the paper (Graham 1980). It is however important to remember that Graham's values were for

a flat plate. As the physical McEel does have a cross sectional area, one would expect its force coefficients to differ from those of a flat plate.

8.7 Discussion

Mathematically the flow encountered by a single flapper is not a pure cross flow. The measured data however shows that predictions made by the Morison Equation with the appropriate force coefficients are quite close to the actual forces measured. Furthermore, it has been shown that the discrepancies between the Morison Equation and measured data cannot be due to the tangential acceleration of this flow.

The main source of error is therefore likely to be the vortices being shed from the eel as it reaches its extreme angle. This vortex shedding is not a phenomenon that is particular to the eel but rather one that occurs in many scenarios to which the Morison Equation is applied. The errors caused by this event are thus not necessarily any larger than those encountered in other calculations relying on the Morison Equation.

The inaccuracies due to end effects are a problem that is greater with the eel than many other structures. As the eel has two moving segments, each 200 mm long with the cross sectional height of 200 mm, it has a low aspect ratio. The tapering of its tail should limit some of these effects.

As shown by the reviewed literature the Morison equation itself is in reality an over simplification of the advanced forces developed by a cross flow and as such it will never give the exact answer. For many applications, though the answer supplied by the equation is accurate enough for its purpose. The question is whether it can be considered accurate enough for calculating the forces acting on a single flapper and equally important how it should be applied and whether it should be used in its original form or with Cd and Ca dependent on Kc number.

When it comes to the question of how the Morison Equation should be applied to get the right force coefficients it has been shown that the inclusion of both longitudinal and transverse forces yields a better prediction. Even if that had not been the case, it could be argued that the force coefficients should not be computed in any other way. Choosing to base the computation of the force coefficients entirely on the transverse

force or on the longitudinal force would be essentially an arbitrary decision. Using both directions on the other hand uses all the available data.

The argument as to whether to use the average values of the force coefficients or whether to compute them in one go is not as straightforward. The case can be argued either way. Luckily, the computed force coefficients based on the same force measurements are typically within 5% of each other depending on whether an average value or a unified time series is used. The latter approach will therefore be used in this thesis unless stated otherwise as it is the more convenient of the two methods.

In the tests presented in this chapter, the version of the Morison Equation with Keulegan-Carpenter number dependent force coefficients produced results of no better quality than the ones produced by the original equation. The decision about which method to use therefore has to be based on other criteria. It could for instance be argued that the original version does not take any account of potential scale effects. If for instance an eel was built at half the height of the one currently tested then the Kc number could change and the hydrodynamic coefficients with it. For the original Morison equation, new hydrodynamic coefficients would have to be measured. Only tests with a similar eel at a different scale can however answer whether the method using Keulegan-Carpenter dependent force coefficients correctly adjusts for scale effects. The choice of which method to use was therefore based on convenience and as all the programming had already been done for the method with varying force coefficients this method will be used for the remainder of this thesis unless stated otherwise.

9 The double flapper

9.1 Introduction

With the addition of a phase-difference between the motions in the two joints, there are far more potential swimming patterns which could be tested. Whilst the single flapper tests had shown that the Morison Equation could predict the measured forces reasonably well, early double flapper tests indicated that this was not so for these tests. It was therefore of interest to see at which exact phase angle the Morison Equation broke down. In total 54 zero speed double flapper runs and 53 double flapper runs with forward speed were tested. The zero speed runs will be presented in section 9.2 whilst the ones with forward speed will be presented in section 9.3.

9.2 The double flapper bollard pull

9.2.1 Introduction

The zero speed double flapper runs are different from the single flapper tests in that segments of the McEel experience tangential velocities and in that, there will be a discontinuity in the middle of the moving part of the McEel's body. Initially, it was still attempted to analyse these tests using the same method as was found suitable for the single flapper tests. This was done partly because the tangential velocities were small (see section 2.3) and partly because the segments of the McEel were designed to create a much smaller drag in the tangential than in the perpendicular direction. Various attempts were made to include tangential drag forces and these will be presented.

The single flapper tests showed that the standard Morison Equation and the method with Keulegan-Carpenter number varying coefficients produced results of similar quality. It was also shown that these coefficients or the constant parts of them were best calculated in one operation for all the runs. It is not obvious that this would still be the case for the tests with phase angle. To examine whether this was so, some of the double flapper trials were analysed using the other methods presented in the matrix in section 8.5. The results were found to be the same as for the single flapper

tests and consequently the standard Morison Equation is therefore not examined in detail.

9.2.2 The double flapper analysed with Cd and Ca

When the bollard pull runs with a phase angle were analysed using Graham's (Graham 1980) form of the Morison Equation the value obtained for the constant part of the added mass coefficient was similar to those obtained for the single flapper runs. The constant part of the drag coefficient was however found to be smaller than that found for the earlier runs.

	Single fl.	Double fl.
added mass:	0.14	0.13
drag:	7.47	5.87

Table 9.2-1: The values for the constant part of the added mass and drag coefficients

Similarly, the average r.m.s. error in the transverse direction was the same as it had been for the single flapper runs whilst for the longitudinal direction it was much worse:

	Single fl.	Double fl.
Fx r.m.s.	0.38	0.47
Fy r.m.s.	0.35	0.35

Table 9.2-2: The ratio of error to the r.m.s. of the measured signal

Again, it may be hard to visualise these errors and for this reason, a typical time history is shown:

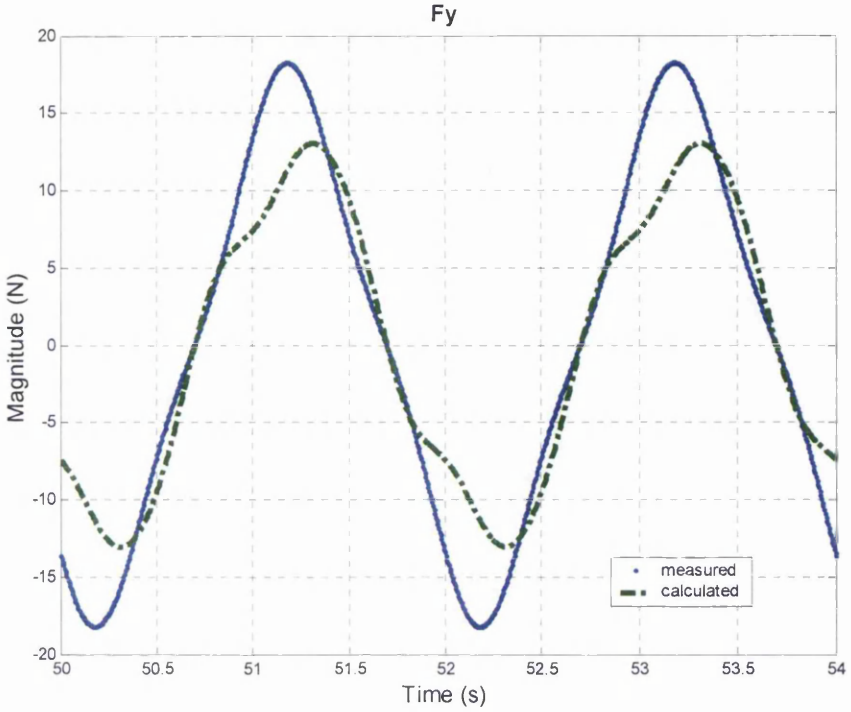

Figure 9-1: A typical time history of the transverse force

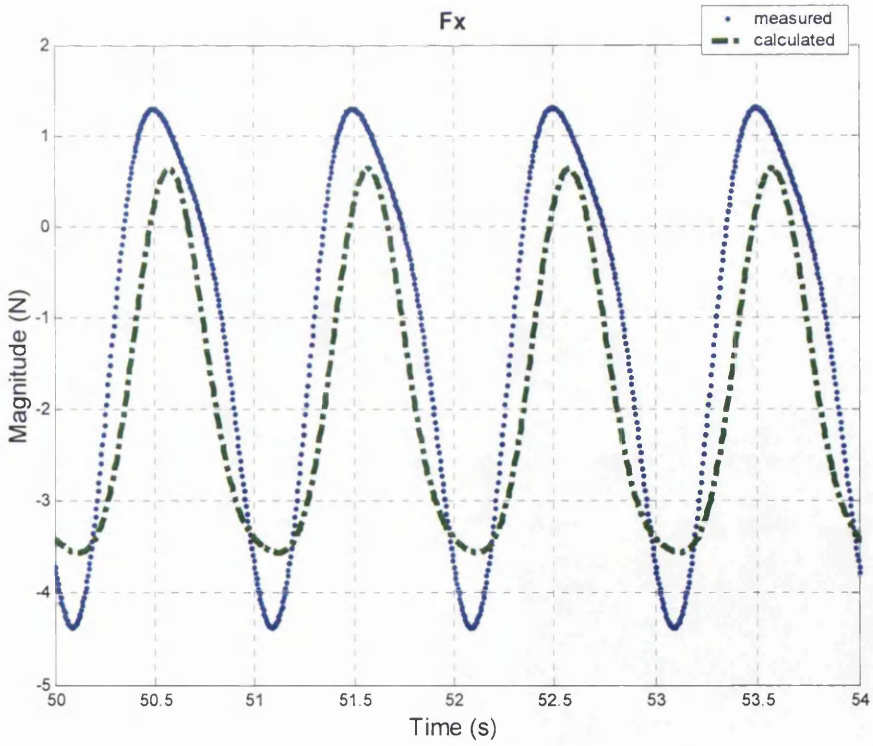

Figure 9-2: A typical time history of the longitudinal force

Figure 9-1 and Figure 9-2 depict the time history of the forces generated in the 30-30-50 scenario at 0.5 Hz and the errors seen are typical in both magnitude and shape.

Looking at Figure 9-2 it seems that the large r.m.s. error in the longitudinal direction is due neither to a shift in the mean value nor to a large phase shift between the two signals. There is a substantial difference in the amplitudes of the two signals but it still seems as if the r.m.s. error is caused primarily by an incorrect shape of the force curve. The measured force oscillates with sharp lower halves and blunter upper halves whilst the computed force did the opposite as seen in Figure 9-2. This again led to an inaccurate mean thrust being calculated. The plot of the mean thrust generated by the 30-40-60 scenario gives a good indication of this:

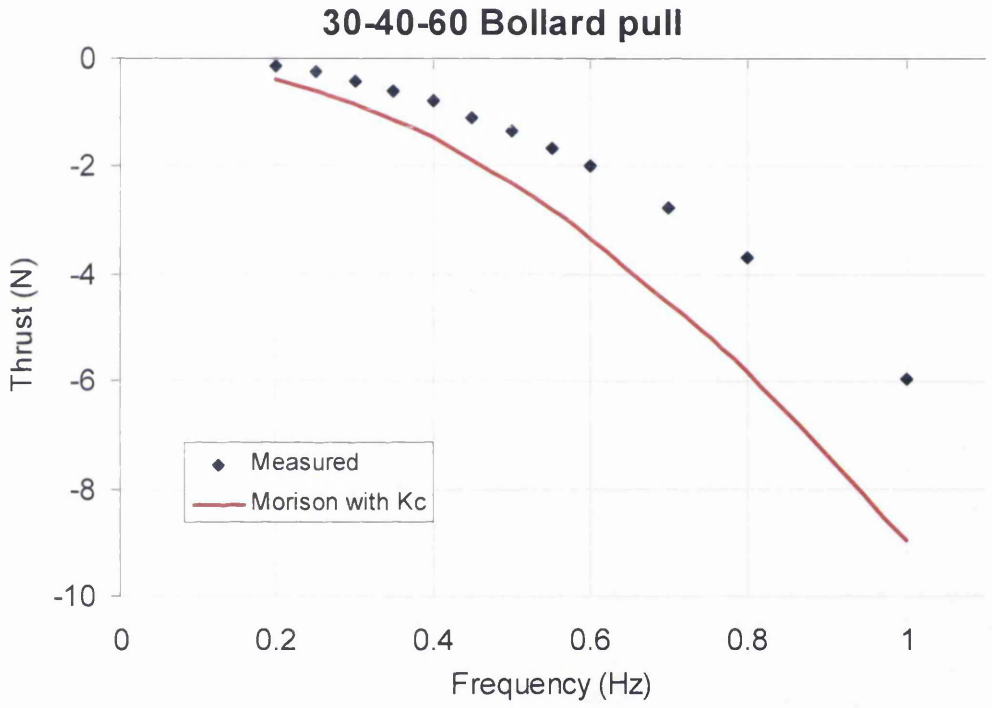

Figure 9-3: The mean thrust for a double flapper

Figure 9-3 can be compared with Figure 8-6 and it immediately becomes obvious that the Morison Equation is much better at predicting the forces from a single flapper.

It is however important to emphasise that the values in Table 9.2-1 are the values for the entire set of double flapper bollard pull runs. When the force coefficients were computed for individual runs, some interesting observations could be made. In the case of the single flapper runs the Kc-independent part of the drag coefficient seemed to increase with increasing excitation frequency. This effect was however measured in the range of excitation frequencies that was tested. In case of the double flapper tests, this effect seemed still to be present but it was overshadowed by the much

larger variations with phase angle. As the phase angle went up the constant part of the drag coefficient went down from around seven with no phase angle to about four with a 60-degree phase angle. This helps to explain why the value for all the double flapper tests in Table 9.2-1 is so different from the one for the single flapper tests presented in Table 8.6-2.

For a while, it was thought that this variation in the constant part of the drag coefficient could help explain the poor force predictions in the longitudinal direction. It was therefore attempted to fit the force coefficients to individual runs. The only effect of this however, was to shift the total r.m.s. error from being mainly in the X-direction to being evenly spread in both directions. It was therefore clear that the Morison Equation on its own is not capable of describing the force generated from the McEel when there is a phase angle between the joints.

As the transverse force is bigger than the longitudinal force, and as it has a longer lever arm than the longitudinal one the inaccuracies in the predicted X-force does not mean that the power requirement cannot be predicted as shown in Figure 9-4.

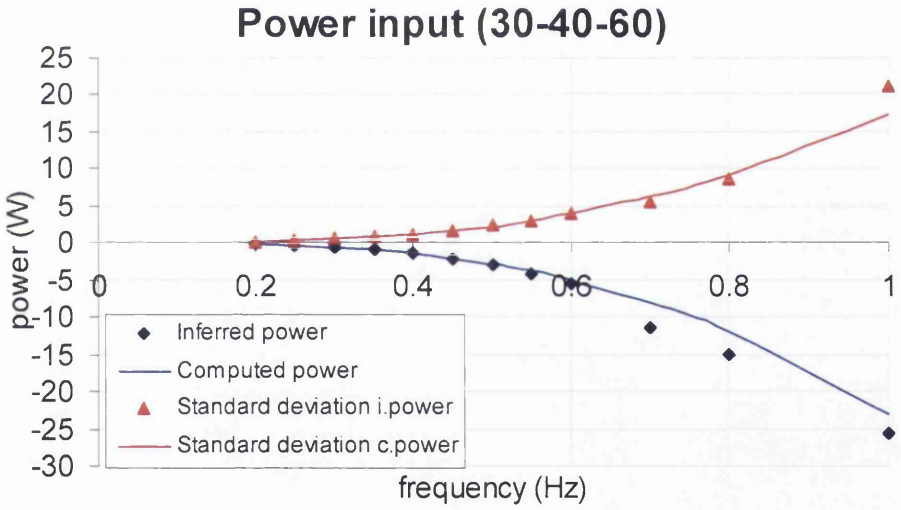

Figure 9-4: The power input, mean and standard deviation, with phase angle

Figure 9-4 is similar to Figure 8-5 and shows how the predicted power differs from the one inferred from the measured forces. The predictions vary more from the measured ones than those shown in Figure 8-5 but the lines still follow the trends of the measured points.

9.2.3 Tangential drag

The most obvious hydrodynamic difference between the single flapper tests and the tests with a phase angle between the two joints is the tangential velocity vector. Numerous attempts were therefore made at trying to include a tangential drag coefficient. The easiest way of doing this would have been to add a tangential drag term to the Morison Equation. This term would then be computed using a tangential drag coefficient. This coefficient could then be evaluated by computing a least square fit for all the three force coefficients. Unfortunately, the Morison Equation does not predict the time history of the forces caused by perpendicular velocities and accelerations particularly well. In addition, the tangential drag force should be quite small as the segments of the McEel are streamlined in the longitudinal direction. Computing a least square fit for the three force coefficient therefore resulted in trying to correct errors in the first two by an addition of a third one rather than computing a sensible value for the tangential drag. This was seen by the tangential drag coefficient taking on widely varying values ranging from negative numbers to very high positive values.

The fact that the least squares fit does not seem to be the right method to compute the tangential drag coefficient does not necessarily mean that one should not be included. Nor could it be guaranteed that the tangential velocities would only generate drag forces. The added momentum method as proposed by Quiggin and Carson (1994) was therefore examined in more detail.

As explained in section 3.3 the method suggested by Quiggin and Carson requires two more coefficients than does the Morison Equation. These two coefficients are Cn, the coefficient of perpendicular skin friction and Ct, the coefficient of tangential drag (assumed to be entirely due to skin friction, see Quiggin and Carson 1994). Both of these coefficients represent small forces and are therefore not suited to be computed using the least squares fit. Values for both of these coefficients are however given in the original paper (Quiggin and Carson 1994). Although the exact value of these coefficients would probably be different for the McEel, the errors in using the suggested values should be small.

Values for Ca and Cd could then be calculated using a least squares fit for all the bollard pull runs with a phase angle. The values for the four force coefficients would then be:

added mass:	**0.13**
drag:	**3.43**
skin friction:	**0.001**
tangential drag:	**0.0025**

Table 9.2-3: The force coefficients used for the added momentum method

As can be seen in Table 9.2-3, both the coefficient for added mass and the drag coefficient are smaller than they were found to be using the normal Morison Equation for the single flapper (see Table 8.6-2).

Using these force coefficients, the mean forward thrust can be computed. This thrust, based on the added momentum method is in general closer to the measured values than the thrust computed using the Morison Equation:

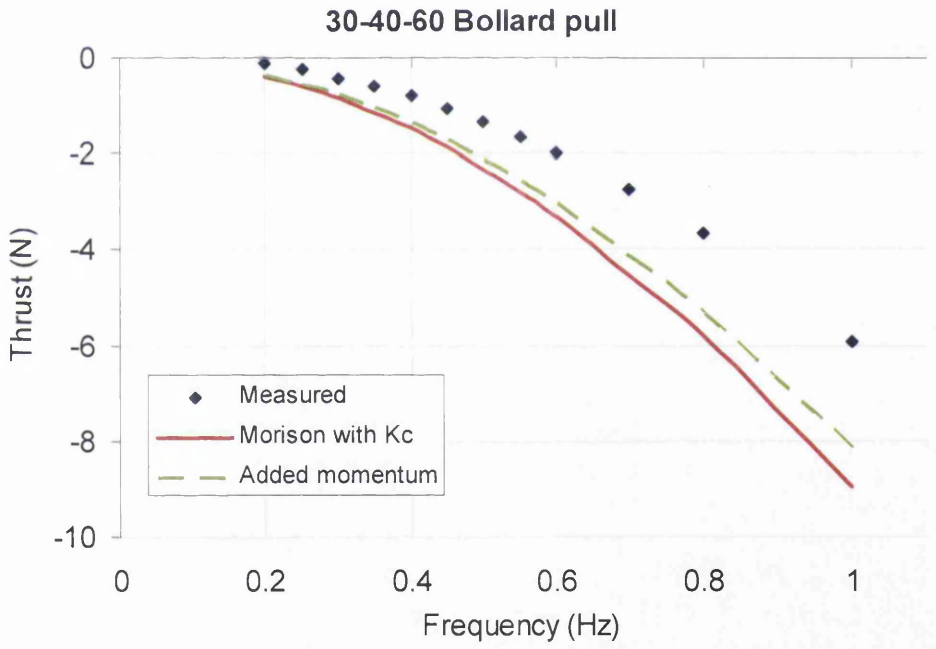

Figure 9-5: The mean thrust predictions compared

As can be seen in this example with the 30-40-60 scenario the added momentum method produces a better estimate of the mean thrust. This is however not the same as saying that the force estimates from the added momentum method are better than the ones generated by the Morison Equation:

Fx RMS	Fy RMS

added momentum	0.54	0.44
Morison (Kc)	0.47	0.35

Table 9.2-4: The ratio of error to r.m.s. of signal

As can be seen from Table 9.2-4, the predictions for the mean thrust may be better using the added momentum method but the time histories of the generated forces are actually worse.

9.2.4 The effect of phase angle on reliability of predictions

Chapter 8 showed that the Morison Equation could predict the forces generated by the McEel fairly well in the single flapper scenario. This section has shown that the predictions become inaccurate with the introduction of a phase angle between the two joints. It is thus of interest to examine at which particular phase angle the predictions break down. The different errors can therefore be examined in detail. The variation in the ratio of error in the transverse force over the r.m.s. of the measured signal is depicted in Figure 9-6.

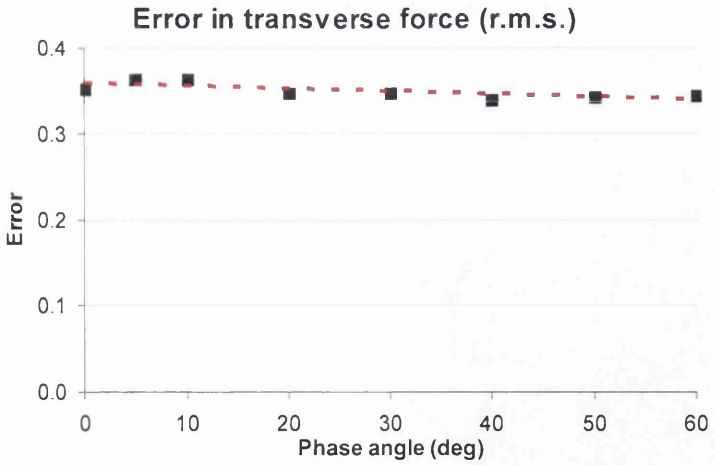

Figure 9-6: The relative transverse error as a function of phase angle

In Figure 9-6, the average value for all the runs with the same phase angle is plotted against phase angle. A linear trend line is added and it can be seen that the average error is actually slightly decreasing with phase angle.

The variation in the ratio of error in the longitudinal force over the r.m.s. of the measured signal is depicted in Figure 9-7.

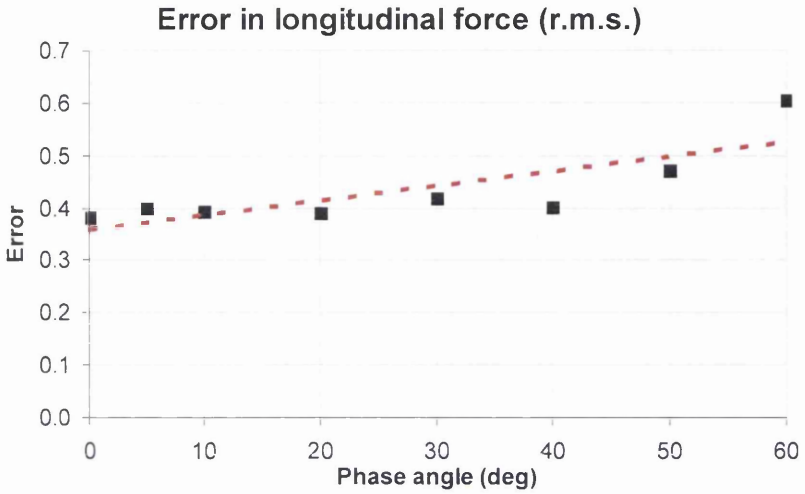

Figure 9-7: The relative transverse error as a function of phase angle

As can be seen the r.m.s. error in the longitudinal direction increases with increasing phase angle. This increasing error in the prediction of the instantaneous force is reflected in an increasing error in the mean forward thrust prediction.

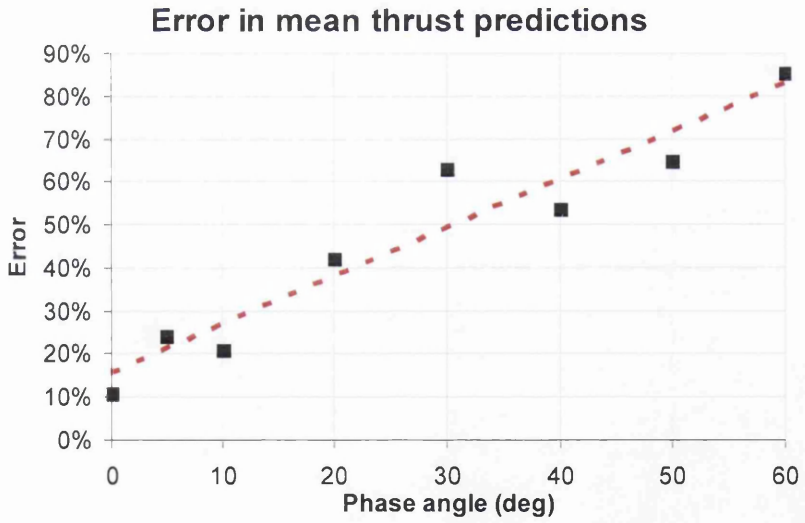

Figure 9-8: The error in the mean thrust as a function of phase angle

Figure 9-8 shows how the mean error in the mean forward thrust prediction increases substantially as the phase angle goes up.

From the errors presented, no exact phase angle at which the analysis breaks down can be found. The force history in the transverse direction is equally good for all phase angles tested whilst the longitudinal force history gets progressively worse

with increasing phase angles. This latter fact seems to be related to the rapidly deteriorating mean forward thrust predictions. Looking back at Figure 6-15 it can be seen that the variations in mean thrust are small with an increasing phase angle. This is not picked up by the Morison Equation. The predicted thrust therefore increases with an increasing phase angle whilst this is only the case to a limited degree and only up to 30-40-degree phase angle for the measured force.

9.2.5 Discussion

Kinematically, the double flapper differs from the single one in that it generates tangential velocity vectors. In so doing, the double flapper encounters a flow field which is truly non-perpendicular. In principle this flow field is therefore similar to the one encountered by real fish. It is therefore worrying that neither the Morison Equation nor the Morison Equation with a tangential drag term nor the method based on added momentum can predict the forces generated.

One possible explanation for this is disadvantageous flow phenomena occurring in the joints. All numeric methods employed in this thesis analyse the McEel in segments, disregarding the discontinuities of the body. This should work well as long as the two segments swing as one. When a phase angle is introduced between the two the tail segment may be set to make bigger propulsive effort but this could be offset by turbulence forming around the joint. The measured force therefore increases only slightly with an increasing phase angle. At higher frequencies though the McEel will start to act as a continuous body, the predictions improve, and a larger variation in thrust should be measured. This corresponds to the observations made but only flow visualisation can verify whether it is the case.

9.3 Runs with forward speed

9.3.1 Introduction

The introduction of forward speed is a fundamental requirement in the understanding of fishlike propulsion. It is however one that adds substantial complexity to the

problem. Most of this is to do with the difficulties of being able to measure the quantities of interest. This was explained in section 6.5. In some respects, fishlike propulsion can be compared to yacht propulsion. As the fish starts to move the thrust generated by its movements decreases just as the thrust of a sail decreases as the yacht speeds up. In addition to this, both the yacht and the fish experience increased resistance from the fluids through which they move.

As explained in section 6.8, 53 different forward speed runs were performed. There were only eight different motion scenarios that were tested however. Each scenario had to be tested at various speeds to ascertain the self-propulsion speed.

The resistance of the eel will be investigated in detail, as an understanding of it is a pre-requisite to the understanding of the runs with forward speed. The time history of the forces generated by the eel in the forward speed mode will then be investigated. The last part of this chapter will look at the mean values of the forward speed runs and thus the attempts at predicting the self-propulsion speed of the McEel.

9.3.2 The resistance

When it comes to comparing the measured forces with the ones computed by the Morison Equation, the resistance of the sting and the stretched straight resistance of the eel should be subtracted to the measured force in the X-direction (see 6.5). This is because the Morison Equation does not attempt to estimate neither the stretched straight resistance of the eel, nor the resistance of the sting. When it comes to estimating the self-propulsion speed of the McEel, the resistance of interest is the stretched straight resistance of the eel only as argued in section 6.5.

The resistance of the eel and sting combined was found empirically well fitted by a cubic polynomial as in Equation 9-1.

$$R = a_1 U + a_2 U^2 + a_3 U^3$$

Equation 9-1

The corresponding coefficients are

Coefficient	Value

a1	2.3
a2	-3.0
a3	8.3

Table 9.3-1: The coefficients for the resistance of both the eel and the sting

This estimate of the combined resistance of the sting and the eel is based on nine selected speed runs ranging from 0.2 m/s to 0.7 m/s as seen in Figure 6-7. The runs that were performed at speeds below 0.2 m/s were deemed inaccurate. The Pearson product moment correlation coefficient squared between the nine data points and the computed resistance was 0.998.

The resistance of the eel on its own was estimated by subtracting the best estimate of the resistance of the sting, as presented in section 6.5 from the combined resistance as computed by Equation 9-1. This resistance was to fit polynomial from Equation 9-1 with the coefficients

Coefficient	Value
a1	1.3
a2	-0.4
a3	3.2

Table 9.3-2: The coefficients for the resistance of the eel

For reference, see Figure 6-7.

9.3.3 The time histories of the generated forces

When comparing the time histories of the forces generated by the McEel with those computed by the Morison Equation the resistance of both the eel and the sting were subtracted from the measured forces. This was done to ensure a fair comparison.

All the forward speed runs that were tested had a phase angle between the two joints. This was done partly as the runs with a phase angle had been found to generate larger thrusts in the bollard-pull condition and partly because it was believed to be closer to actual fishlike propulsion.

The Kc-independent part of the force coefficients were evaluated in one operation for all the runs with forward speed:

	Single fl.	Double fl.	Forw.Speed
added mass:	0.14	0.13	0.15
drag:	7.47	5.87	7.20

Table 9.3-3: The constant part of the force coefficients

As all the forward speed tests are double flapper tests with various forward speeds it may be surprising to see that the value for the constant part of the drag coefficient lies between the one computed for a single flapper and the one computed for the double flapper bollard pull. This could be a result of less turbulence around the joints but again only flow visualisation tools can answer this.

The accuracy of the time histories of the generated forces is not improved with forward speed:

	Single fl.	Double fl.	Double sp.
Fx r.m.s.	0.38	0.47	0.51
Fy r.m.s.	0.35	0.35	0.37

Table 9.3-4: The ratio of error to the r.m.s. of the force signals

Again, these errors may be hard to visualise and for this reason, a typical time history is depicted in detail:

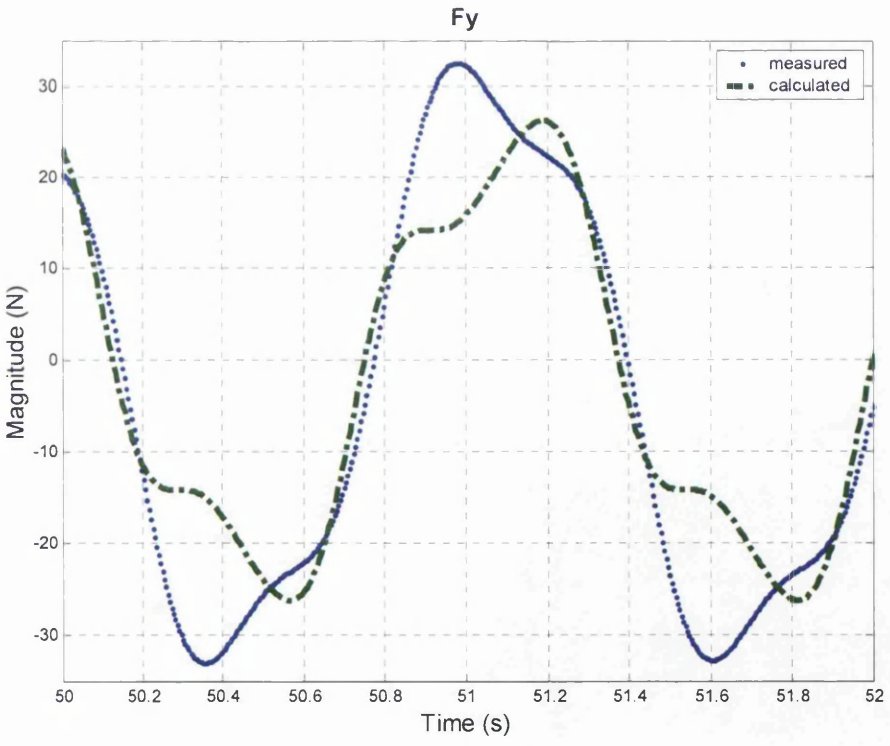

Figure 9-9: A typical time history in the transverse direction

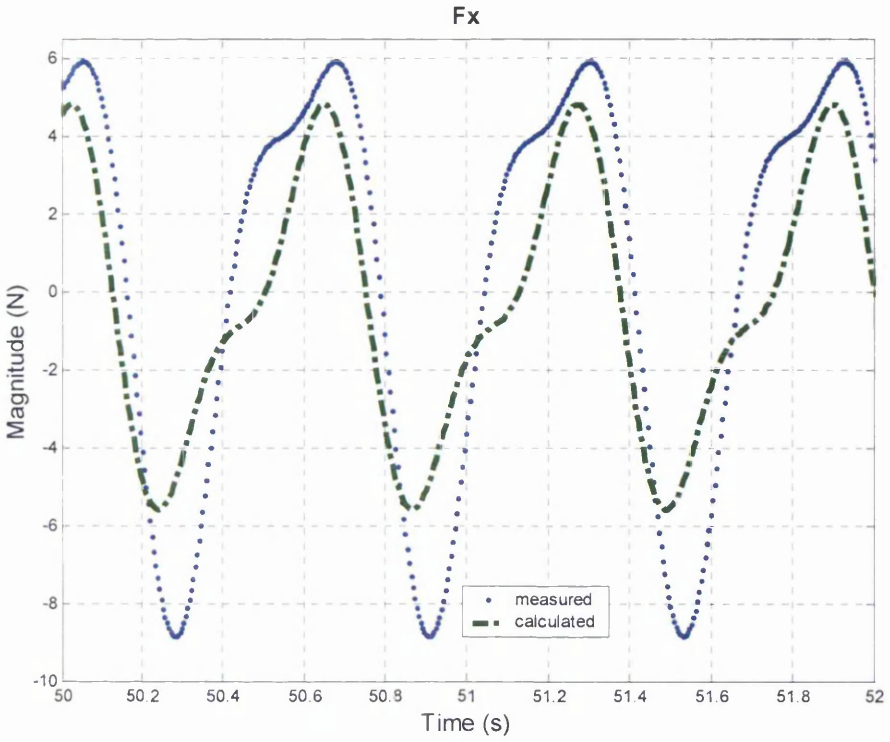

Figure 9-10: A typical time history in the longitudinal direction

Figure 9-9 and Figure 9-10 depict the 30-40-60 scenario at 0.8 Hz excitation frequency and with a carriage speed of 0.5 m/s. The r.m.s. errors for these two graphs are 0.38 and 0.52 respectively and it is typical of the forward speed runs.

As can be seen in these graphs the Morison Equation is not suited to predict the time histories of the generated forces by the McEel. The general pattern from the bollard pull tests with a phase angle can still be observed:

- The prediction is much better in the transverse than in the longitudinal direction.
- The longitudinal force has sharp negative peaks and blunt positive ones whilst the Morison Equation predicts the opposite.
- This leads the Morison Equation to over-predict the forward thrust of the McEel when there is a phase angle between the joints, irrespective of the forward speed.

9.3.4 The McEel at self-propulsion speed

When the self-propulsion speed of the McEel was sought, the resistance of the eel itself also had to be included in the calculation. As seen in section 9.3.2 the resistance of the eel itself was a third degree polynomial. The measured force of the swimming eel with the sting was shown in section 6.8 to follow a straight line. The mean force of the swimming eel without the sting should therefore be a third degree polynomial. As the variation in resistance of the eel was limited though the final curve was considered close enough to a straight line:

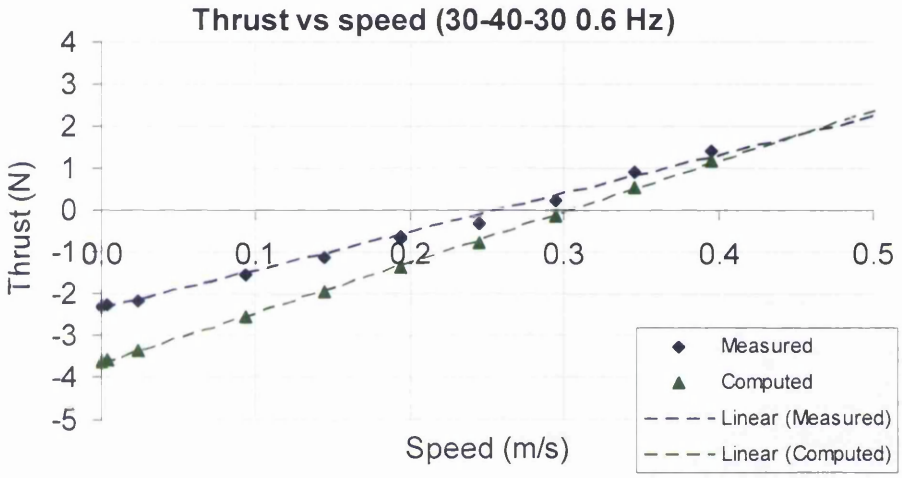

Figure 9-11: A typical plot of thrust against speed

In this graph, a typical scenario is shown. The blue diamonds indicate the measured mean forward thrust without the resistance of the sting. The green triangles show the corresponding values computed by the Morison Equation. A straight line is fitted for both sets of data. The worst Pearson product moment correlation coefficient squared for the eight scenarios was 0.989 and a straight-line curve fit thus seems reasonable.

The computed and measured self-propulsion speeds are shown in Table 9.3-5.

Motion	Frequency (Hz)	Measured (m/s)	Computed (m/s)	Error
30-40-60	0.4	0.19	0.22	19%
30-30-30	0.6	0.26	0.31	19%
30-30-60	0.6	0.27	0.34	29%
30-40-30	0.6	0.26	0.31	17%
30-40-60	0.6	0.28	0.34	21%
30-40-30	0.8	0.35	0.41	18%

30-40-60	0.8	0.40	0.47	16%
30-40-60	1.0	0.58	0.58	2%

Table 9.3-5: The self-propulsion speeds based on measurements compared with computed values

As none of the eight swimming scenarios was actually tested at the self-propulsion speeds given in Table 9.3-5 any computation of the required power at this speed will have to be based on interpolation. This is considered appropriate since the power computed from the measured forces as well as the power computed based on the forces from the Morison Equation both varied smoothly with carriage speed as seen in Figure 9-12.

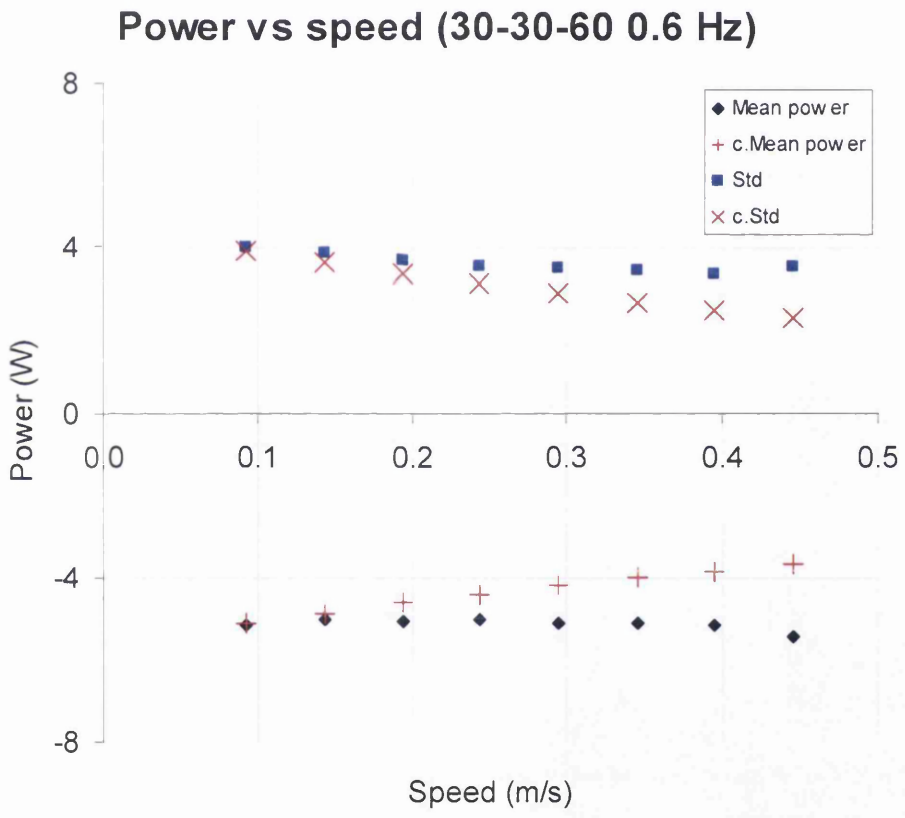

Figure 9-12: The power required vs. carriage speed

In this, graph the mean and standard deviation of the power required by the oscillations of the eel is plotted against carriage speed. As the power varies smoothly with carriage speed, the computed values can be compared to the measured ones at the self-propulsion speed.

Motion	Frequency (Hz)	Speed (m/s)	Inferred mean power (W)	Computed mean power (W)	Error	Inferred stdev (W)	Computed stdev. (W)	Error
30-40-60	0.4	0.2	-1.6	-1.4	14%	0.9	0.8	10%
30-30-30	0.6	0.3	-7.7	-6.5	16%	5.7	5.2	10%
30-30-60	0.6	0.3	-5.7	-4.3	23%	3.1	3.5	15%
30-40-30	0.6	0.3	-9.4	-7.8	17%	6.6	6.1	7%
30-40-60	0.6	0.3	-5.5	-4.6	16%	3.3	2.9	12%
30-40-30	0.8	0.3	-21.8	-18.2	16%	15.6	14.2	9%
30-40-60	0.8	0.4	-13.0	-10.5	19%	7.2	6.6	9%
30-40-60	1.0	0.6	-23.5	-19.3	18%	13.7	12.0	12%

Table 9.3-6: The computed power compared with the inferred power at self-propulsion speed

In this table, power is given in W, speed is given in m/s and frequency is given in Hz. Again, it is important to remember that these figures are based on computed force distributions so they should be read with caution. It is however interesting to see that at self-propulsion speed the Morison Equation seems to under-estimate the mean power requirement by about 20%.

9.3.5 Discussion

In this section, various force and power estimates computed from the Morison Equation have been compared with measured data. It has been shown that the Morison Equation is not well suited to compute the time history of the forces generated by the McEel in the longitudinal direction. This is not surprising as the Morison Equation is unable to predict accurately the time history of the force generated by a wave hitting a vertical pile (Keulegan and Carpenter 1958). Even so, the equation has found widespread use in that particular field as it is simple to use and can generate a prediction that is accurate enough for design purposes.

Only eight different swimming patterns have been investigated, in this section. The empirical data is thus limited, but even so, some conclusions about swimming styles and the suitability of the Morison Equation as a design tool will be drawn.

In Table 9.3-5, the self-propulsion speeds of the various swimming styles are shown. It is clear that excitation frequency is a key parameter in determining self-propulsion speed.

A)

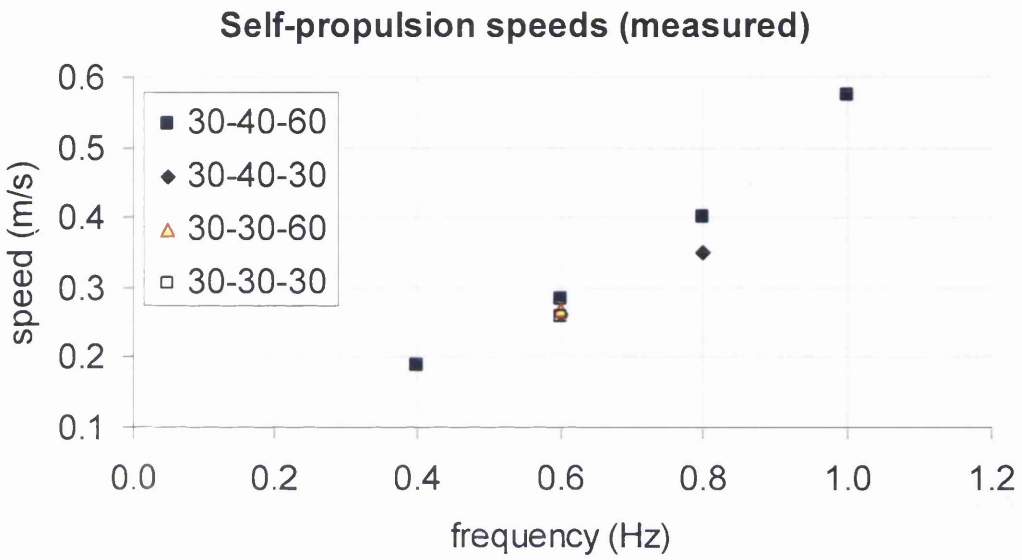

B)

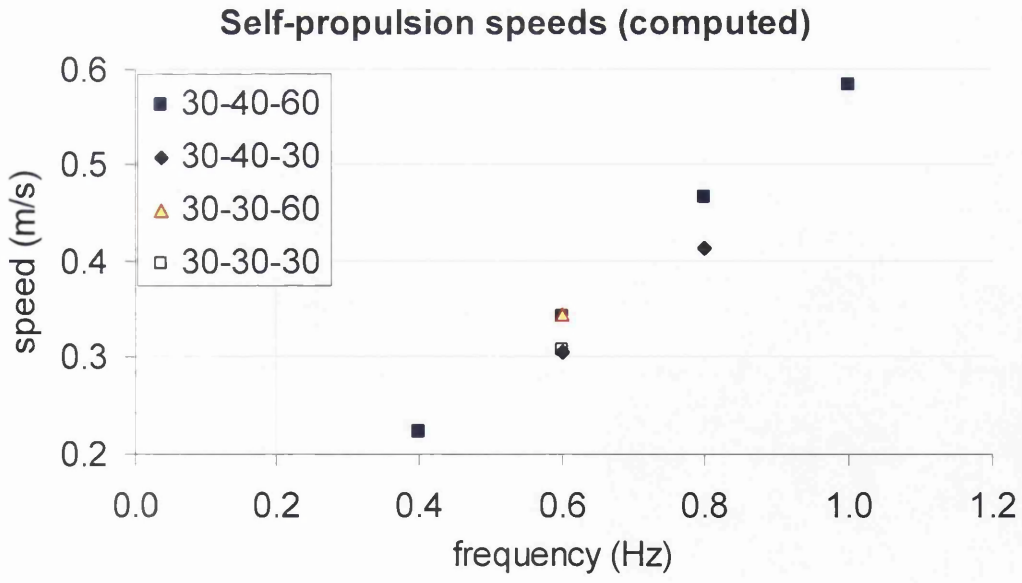

Figure 9-13: The self-propulsion speed against excitation frequency

Figure 9-13 A) shows the measured self-propulsion speeds whilst part B) of the same figure shows the computed self-propulsion speeds. In the measured plot, the four

patterns with an excitation frequency of 0.6 Hz are at similar self-propulsion speeds whilst the two patterns done at 0.8 Hz differ more widely. However, the 30-40-60 swimming style seems to attain the highest self-propulsion speed at both frequencies.

The measured graph shows a similar picture except that the self-propulsion speed of the 30-30-60 scenario seems to be over-predicted by the Morison Equation. In fact, the Morison Equation predicts that the 30-30-60 swimming pattern and the 30-40-60 swimming pattern should have the same self-propulsion speed at 0.6 Hz excitation frequency. Except from this, the Morison Equation correctly predicts the ranking of the self-propulsion speeds.

For most applications, both the attained speed and the power required are of interest. A good measure for this is transport efficiency defined as:

$$\eta_T = \frac{U\Delta}{P}$$

Equation 9-2

In order to compute this, a displacement is needed. However, as it is only the transport efficiency relative to the other swimming styles that is of interest here they can all be normalised. All the patterns are therefore compared to the 0.4 Hz case.

A)

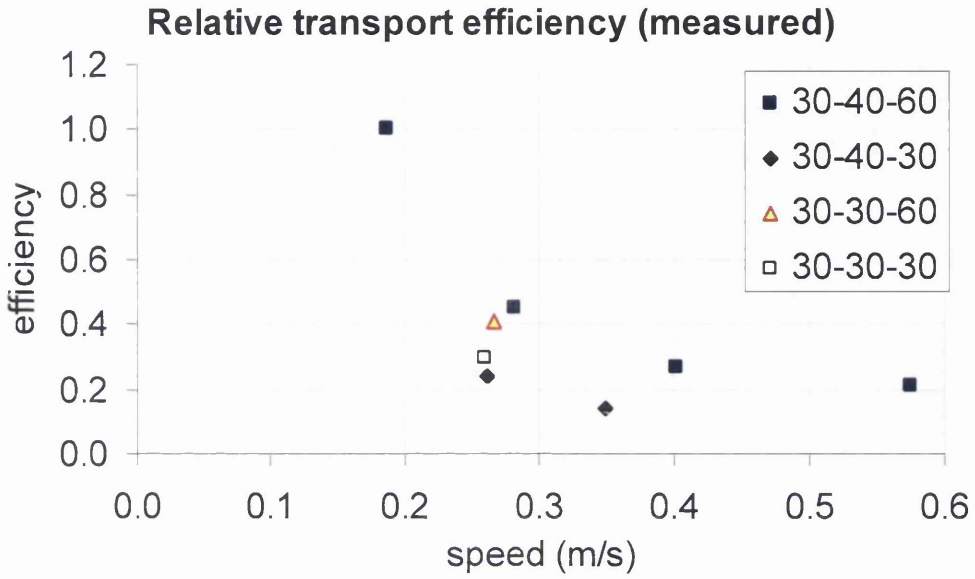

B)

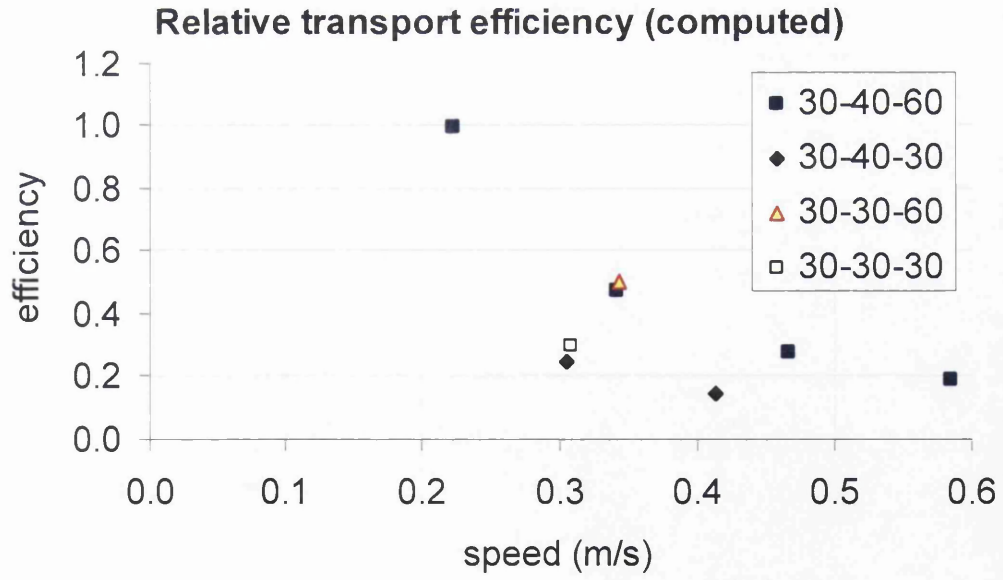

Figure 9-14: The relative transport efficiency of the various swimming styles

Figure 9-14 A) depicts the transport efficiency based on measured values whilst Figure 9-14 B) depicts the computed values. As expected the transport efficiency drops with an increasing speed for both the measured and computed values.

In the first part of the figure, it can be seen that the 30-40-60 swimming style attains the highest transport efficiency as well as the highest self-propulsion speed. This may be surprising as a smaller phase angle produced the highest thrusts in the bollard pull condition (see Figure 6-15).

In Figure 9-14 B) it can be seen that the over prediction of the 30-30-60 0.6 Hz self-propulsion speed leads to a corresponding over prediction of the transport efficiency. Other than that, the Morison Equation correctly predicts the ranking of the relative transport efficiencies.

No apparent reason was found for the discrepancy between the self-propulsion speed from the Morison Equation and the measured one for the 30-30-60 scenario. One possible explanation is that the difference is caused by one of the force components not included in the Morison Equation, such as vortex shedding or lifting forces. Further tests would however be needed to verify this.

The question is therefore whether the estimates provided by the Morison Equation are accurate enough to be useful in the design of a mechanical eel in forward motion. In this section, it has been shown that the predicted self-propulsion speed is likely to be up to 30 % higher than the attained speed and that the power required to oscillate the eel is likely to be up to 25 % higher than that computed by the Morison Equation. However, the discrepancies are relatively consistent and it has been shown that the ranking between the various swimming patterns can generally be well predicted by the Morison Equation. Consequently, the Morison Equation seems reasonably well suited as a preliminary design tool for a mechanical eel.

Conclusions

- The computation of the hydrodynamic forces generated by fishlike motion is a challenging problem, mainly due to the fact that the geometry of the body changes throughout the cycle. Computation of the forces from a mechanical fishlike propulsion device with jointed segments is even more difficult because of the discontinuities along its length.
- It has been shown that segments of a mechanical eel encounter a flow field with both perpendicular and tangential velocity and acceleration vectors. The simple numerical methods that have been commonly used for computing the net longitudinal and transverse hydrodynamic forces arising from fishlike propulsion are mostly based on either drag or inertia forces related to perpendicular components of velocity or acceleration.
- For this reason, an investigation has been made into how well a numerical method based on the Morison Equation can predict the longitudinal and transverse hydrodynamic forces. This approach allows the calculation of both drag and inertia forces but requires values for two force coefficients. Methods were developed with both Keulegan-Carpenter dependent and independent force coefficients.
- A physical model of a mechanical eel has been designed, built and tested in a towing tank. The eel was attached to a load cell beneath the towing tank carriage. The data from the model has been used firstly to determine force coefficients and secondly to compare predictions with measured data.
- A set of tests have been performed to examine how well predictions based on a single set of force coefficients can match the measured data and thus enable the numerical method to make predictions about untested swimming patterns.
- The physical model was tested as a single flapper without forward speed and as a double flapper both with and without forward speed. When it was tested without forward speed, the mean forward force generated was found to increase like a smooth second-degree polynomial with increasing excitation frequency. In the forward speed scenario, the eel performed a set swimming pattern for numerous runs with increasing towing speed. The range of speeds was chosen such that for the first ones the eel was towing the carriage whilst in the latter ones the carriage

was towing the eel. The mean forward force was found to vary linearly with speed in the speed range of interest.

- The least squares fit method was used to fit the force coefficients based on measured data. It was found that fitting the force coefficients for both the transverse and longitudinal forces resulted in the best mean forward force predictions. Allowing the coefficients to vary with Keulegan-Carpenter number was found to yield results of a same quality as the method with constant force coefficients.
- In the longitudinal direction, it was found that the predicted time-history of the force did not match the measured results particularly well. In the single flapper bollard-pull runs, the r.m.s. error was 38 % of the r.m.s. of the measured signal on average. When the eel was tested with a phase angle, this error increased to 47 % when stationary and 51 % in the forward speed runs.
- The forces in the transverse direction the predicted time histories fitted the measured data much better. The average r.m.s. error for the runs without forward speed was 35 % of the r.m.s. of the measured signals, both for the tests with and without a phase angle. For the forward speed runs, the same average error was only marginally worse at 37 %.
- In general, the mean forward thrust predictions were found to be much more accurate than the time history predictions even though the force coefficients were fitted for the time histories and not the mean values. In the single flapper scenario, the Morison Equation was found to be able to predict the mean forward thrust with an average error of 11 %. In the scenario with a double flapper without forward speed, this error increased dramatically to 57 %. However, when the eel was tested with forward speed, the predicted self-propulsion speed matched the measured data with an average error of 18 %.
- The mechanical eel that has been tested in this study consisted of just two moving segments. In the future, it would be interesting to see if the lessons learned from this study hold true for an eel with more segments. The eel was also rigidly attached to a sting and as such, any rotational moment was taken up by the sting. It would also be interesting to see if the lessons learned about swimming patterns would hold true for a free-swimming eel. In order to increase the understanding of the hydrodynamic forces generated by a mechanical eel it

would be beneficial to have access to some flow visualisation technique. Particularly at the discontinuities in the joints, this would be good as it could help explain why the force predictions deteriorate so markedly with the addition of a phase angle between the joints.

References

A. Azuma, 1992, "The Biokinetics of Flying and Swimming", Springer-Verlag, Tokyo.

N. Barltrop, 2004, private correspondence.

D.S. Barrett, 1996, "Forces and efficiency of a flexible hull vehicle", PhD Thesis, Massachusetts Institute of Technology.
http://theses.mit.edu/Dienst/UI/2.0/Page/0018.mit.theses/1996-37/7?

P. W. Bearman et al., 1985,"Forces on cylinders in viscous oscillatory flow at low Keulegan-Carpenter numbers", J. Fluid Mech., vol. 154.

L. E. Borgman, 1958, "Computation of wave forces on inclined cylinders." Trans. Am. Geophysical Union vol. 39 No 5.

C. M. Breder, 1926, "The locomotion of fishes", Zoologica vol. IV, No.5

J. Carling et al., 1998, "Self-propelled anguilliform swimming: simultaneous solution of the two-dimensional Navier-Stokes equations and Newton's laws of motion." J. Exp. Biol., Vol. 201

H. W. Coleman and W. G. Steele, 1999, "Experimentation and uncertainty analysis for engineers", John Wiley & Sons, New York.

Ø. Ekeberg, 1993, "A combined neuronal and mechanical model for fish swimming", Biolgical Cybernetics, Vol. 69

O. M. Faltinsen, 1990, "Sea loads on ships and offshore structures", Cambridge University Press, Cambridge.

Gary B. Gillis, 1996, "Undulatory locomotion in elongate aquatic vertebrates: Anguilliform swimming since Sir James Gray", Amer. Zool., Vol. 36

Gary B. Gillis, 1998, "Environmental effects on undulatory locomotion in the American eel *anguilla rostrata*: kinematics in water and on land", J. Exp. Biol. 201.

J.M.R. Graham, 1980, "The forces on sharp-edged cylinders in oscillatory flow at low Keulegan-Carpenter numbers", J. Fluid Mech., vol. 97 part 1.

J. Gray, 1936, "Studies in animal locomotion- VI. The propulsive powers of the dolphin", J. exp. Biol., 13

S.F. Hoerner, 1958, "Fluid – Dynamic Drag", p.11-18

S. Huang, 1998, private conversation

G.H. Keulegan and L.H. Carpenter, 1958, "Forces on cylinders and plates in an oscillating fluid", J. Research N.B.S. vol. 60, 423.

M. J. Lighthill, 1960, "Note on the swimming of slender fish", J. Fluid Mech.

D.J. Maull & M.G. Milliner, 1979, "The forces on a circular cylinder having a complex periodic motion." Taken from "Mechanics of wave induced forces on cylinders" Pitman, London.

K. A. McIsaac & J. P. Ostrowski, 2003, "Motion Planning for Anguilliform Locomotion", IEEE Trans. On Robotics and Automation, Vol. 19 issue 4.

J.R. Morison et. al., 1950, "The force exerted by surface waves on piles", Pet. Trans., 189

I. Prislin et al., 1998, "Viscous damping and added mass of solid square plates", 17th International conference on Offshore Mechanics and Arctic Engineering, OMAE98-0316.

P. P. Quiggin & R. M. Carson, 1994, "Hydrodynamics of flexibles: Replacing the Morison Inertia Term", Underwater Technology, vol. 20 num. 4.

J. Riis, 2001, "The mechanical Eel – An investigation of the hydrodynamic forces on a slender flexible structure", MSc thesis, University of Strathclyde.

T. Sarpkaya, 1986, "Force on a circular cylinder in viscous oscillatory flow at low Keulegan-Carpenter numbers", J. Fluid Mech., vol. 165.

T. Sarpkaya & M. Isaacson, 1981, "Mechanics of wave forces on offshore structures", van Nostrand Reinhold Company.

V. Sundar et al., 1998, "Hydrodynamic coefficients for inclined cylinders", Ocean Engng., vol. 25

M.S. Triantafyllou et al., 1996,"A new paradigm of propulsion and maneuvering for marine vehicles", SNAME transactions, Vol. 104

M.S. Triantafyllou et al., 1999, US patent 5,997,369, December 7.

J.J. Videler, 1993, "Fish swimming", Chapman & Hall, ISBN 0412408600.

W. J. Vlymen, 1974, "Swimming Energetics of the larval anchovy, *Engraulis Mordaux*", Fish. Bull., Vol. 72

Appendix A The angles in the joints

A.1 Introduction

In nature the exact motion of various anguilliform swimmers vary considerably (Gillis 1996). In engineering terms, it does however seem fair to approximate all anguilliform locomotion to a straight head section and a tail section with a backward travelling wave with increasing amplitude. This tail section will normally contain just over a full wavelength and the amplitude at the tip of the tail will be round about $1/10^{th}$ of the over-all length of the animal.

A.2 Emulating nature

If a mechanical eel were to emulate anguilliform locomotion with rigid sections, oscillating angles of increasing amplitudes would be required in the joints. The exact nature of these angles could be investigated by defining the curve that the rigid segments were to replicate:

$$y = \frac{x}{10}\sin(kx - \omega t)$$

Equation A-1

In this equation y is the distance from the centreline, x is the longitudinal coordinate from the front end of the tail section. The k is the wave number and ω is the radial frequency of the oscillations.

If the length of each of the rigid segments is denoted L, then the front segment would start at (0,0) and end in (L cos θ,L sin θ). The angle θ is then the angle that this front segment makes with the global coordinate system. This angle can be found for any time t by solving the following equation:

$$\frac{x}{10}\sin(kx - \omega t) = L\sin\theta$$

$$\Downarrow$$

$$\frac{L\cos\theta}{10}\sin(kL\cos\theta - \omega t) = L\sin\theta$$

$$\Downarrow$$

$$\frac{1}{10}\sin(kL\cos\theta - \omega t) = \tan\theta$$

Analytically this equation is hard to solve but numerically it is straightforward. In a similar way, all the angles required in the various joints can be found. A numeric example can therefore be examined to see how the angles vary with time.

In the numeric example, the tail section is made up of eight rigid sections of 0.2 m length. The wavelength is 1.44 m and the frequency of oscillation is 1 Hz. The time history of the angle in all the joints can now be given:

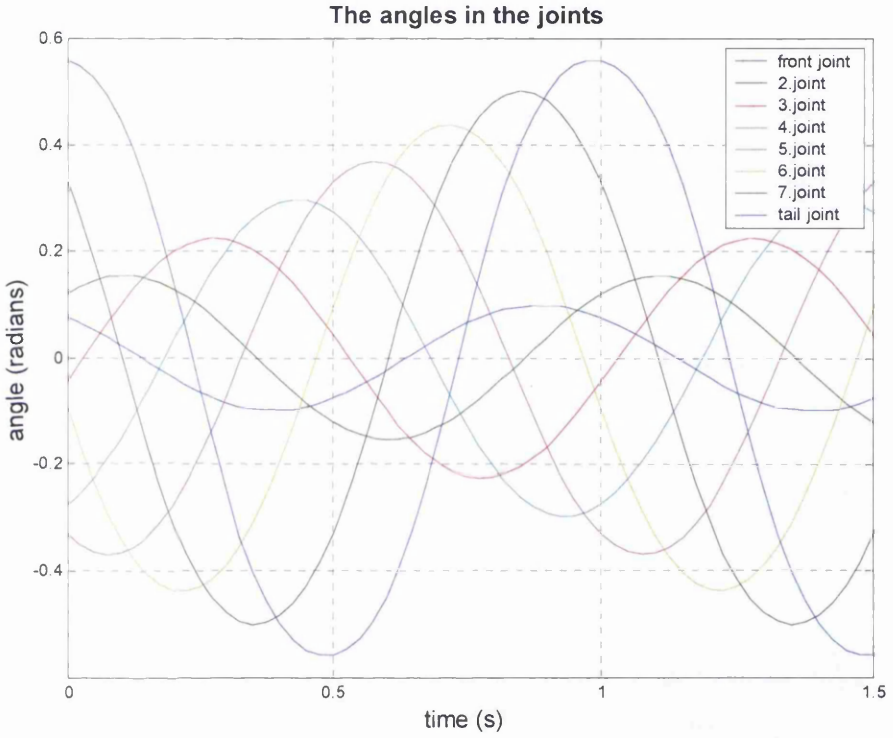

Figure A.2-1: The angles in the various joints

In Figure A.2-1, it can be seen how all the joints seem to be making sinusoids with increasing amplitudes. Moreover, a closer comparison of the angle in front joint with a pure sinusoid reveals how similar they are:

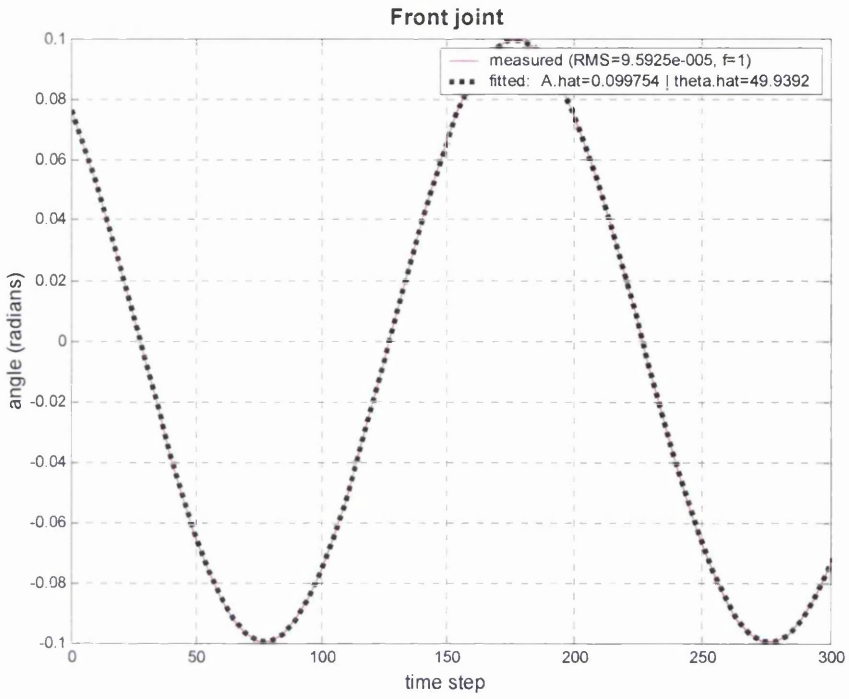

Figure A.2-2: The required angle in the front joint compared to a sinusoid

In this figure, the nearest true sinusoid is plotted with black dots on top of the required angle, which is plotted as a solid red line. A similar comparison between the angle required in the tail joint and the nearest true sinusoid is different:

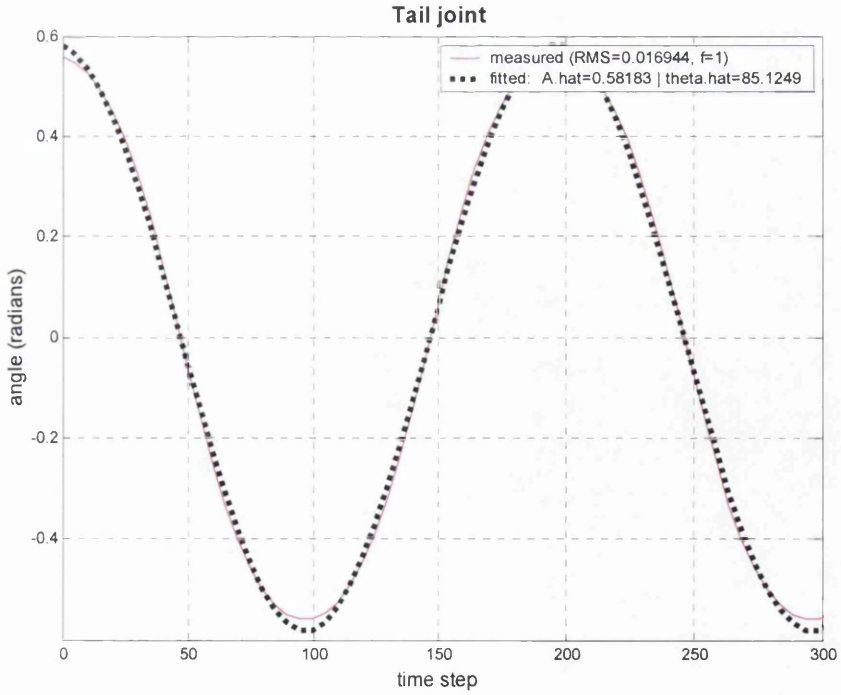

Figure A.2-3: The required angle in the tail joint compared to a sinusoid

Although the required angle is still quite similar to the sinusoid, it does appear to be slightly more like a square wave.

It is important to emphasise that the given numeric example is just one type of anguilliform locomotion. Other types may therefore require other angles in the joints. The example given does however demonstrate that an anguilliform locomotion style which aims to emulate nature may require non-sinusoidal motions in the joints.

Appendix B Other numeric models

B.1 Introduction

In chapter 4, it was shown how the lumped mass model, the distributed mass model, the lumped Morrison model and the distributed Morison model would be implemented. In this appendix, it will be shown how various attempts at including tangential hydrodynamic forces would have been included. As it turned out all these attempts were in the end discarded for various reasons and as such, their mathematical implementation does not merit a place in the main text.

B.2 Tangential forces the traditional way

The pure inertia forces calculated in chapter 4.3 and 4.4 are both tangential and perpendicular to the eel. The hydrodynamic forces on the other hand have so far only been calculated perpendicularly to the eel. In chapter 2, it was shown how the segments of a mechanical eel experience both acceleration and velocity in both tangential and perpendicular directions. Unless it can be asserted that the tangential forces are negligible one must therefore assume that they also need to be evaluated.

The tangential-velocity and -acceleration can be calculated in the same way as their normal equivalents were calculated. The tangential unity vector would be:

$$\vec{\mathbf{T}}_i = \begin{bmatrix} \cos\theta_i \\ \sin\theta_i \end{bmatrix}$$

Equation B-1

This would be the tangential unity vector pointing backward along the eel. Using this vector the tangential velocity of each element of each segment of the eel can be calculated:

$$\vec{\mathbf{v}}_{T,j,i} = \left[\begin{bmatrix} \dot{x}_{j,i} \\ \dot{y}_{j,i} \end{bmatrix} \bullet \vec{\mathbf{T}}_i \right] \vec{\mathbf{T}}_i$$

Equation B-2

Written out in the x- and y-directions this expression would read:

$$\dot{x}_{T,j,i} = \left[\dot{x}_{j,i}\cos\theta_i + \dot{y}_{j,i}\sin\theta_i\right]\cos\theta_i$$
$$\dot{y}_{T,j,i} = \left[\dot{x}_{j,i}\cos\theta_i + \dot{y}_{j,i}\sin\theta_i\right]\sin\theta_i$$

Equation B-3

The tangential drag force can be calculated using a relevant skin friction coefficient Cds:

$$f_{\dot{x}T,j,i} = \tfrac{1}{2}\rho\, sw_{j,i}\, C_{ds}\left(\sqrt{\dot{x}_{T,j,i}^{\,2} + \dot{y}_{T,j,i}^{\,2}}\right)\dot{x}_{T,j,i}$$
$$f_{\dot{y}T,j,i} = \tfrac{1}{2}\rho\, sw_{j,i}\, C_{ds}\left(\sqrt{\dot{x}_{T,j,i}^{\,2} + \dot{y}_{T,j,i}^{\,2}}\right)\dot{y}_{T,j,i}$$

Equation B-4

In this equation $sw_{j,i}$ represents the wetted surface area of the j-th element of the i-th segment. The skin friction coefficient is assumed uniform throughout the eel. This may be an unjustified simplification. No data is available on its variation though and a uniform value would appear to be a suitable first approximation.

Like the vertical forces developed by a floating cylinder subjected to surface waves the added mass forces experienced by the eel in the tangential direction will be assumed to apply only to the end of the tail. This assumption seems reasonable for a straight cylinder. For an eel with substantial angular changes along its length, it is more dubious. The segments of the eel are however considered to be overlapping and it would thus seem a fair assumption that most if not all of the added mass that applies tangentially to the eel follows the acceleration of the tip of tail.

The tangential acceleration of the tip of the tail would be:

$$\vec{a}_T = \left[\begin{bmatrix}\ddot{X}_{N+1}\\ \ddot{Y}_{N+1}\end{bmatrix} \bullet \vec{T}_i\right]\vec{T}_i$$

Equation B-5

Written out in the X- and Y-directions this expression would read:

$$\ddot{X}_{T,N+1} = \left[\ddot{X}_{N+1} \cos\theta_N + \ddot{Y}_{N+1} \sin\theta_N \right] \cos\theta_N$$
$$\ddot{Y}_{T,N+1} = \left[\ddot{X}_{N+1} \cos\theta_N + \ddot{Y}_{N+1} \sin\theta_N \right] \sin\theta_N$$

Equation B-6

A suitable volume of water and a suitable coefficient of tangentially added mass are also needed to complete the calculation of the tangential inertia force. These two quantities are interdependent, as the definition of the volume will affect the magnitude of the coefficient. A definition similar to the one employed by Prislin et al. (1998) has been chosen:

$$F_{\ddot{x}T} = \rho \frac{D^3}{2} C_{it} \ddot{X}_{T,N+1}$$
$$F_{\ddot{y}T} = \rho \frac{D^3}{2} C_{it} \ddot{Y}_{T,N+1}$$

Equation B-7

The overall forces acting on the individual element can now be computed:

$$f_{\Sigma,x,j,i} = \frac{m_i}{k} \ddot{x}_{j,i} + f_{\ddot{x},j,i} + f_{\dot{x},j,i} + f_{\dot{x}T,j,i}$$
$$f_{\Sigma,y,j,i} = \frac{m_i}{k} \ddot{y}_{j,i} + f_{\ddot{y},j,i} + f_{\dot{y},j,i} + f_{\dot{y}T,j,i}$$

Equation B-8

This is Equation 4-35 with the addition of the tangential drag forces taken from Equation B-7.

The instantaneous thrust can now be calculated:

$$Thrust_{inst} = F_{\ddot{X}T} + \sum_{i=1}^{n} \sum_{j=1}^{k} f_{\Sigma,x,j,i}$$

Equation B-9

The moment in the backmost joint would similarly be:

$$M_n = F_{\ddot{y}T}\left(X_{n+1} - X_n\right) - F_{\ddot{x}T}\left(Y_{n+1} - Y_n\right) + \sum_{j=1}^{k}\left(f_{\Sigma,y,j,n}\left(x_{j,n} - X_n\right) - f_{\Sigma,x,j,n}\left(y_{j,n} - Y_n\right)\right)$$

Equation B-10

In this equation, the total force acting on the individual elements of the tail segment is computed according to Equation B-8. The tangential added mass forces appear only in the calculation of the moment in the backmost joint, as the backmost segment is the only segment directly affected by these forces. The moment in the i-th joint is therefore:

$$M_i = \sum_{j=1}^{k}\left(f_{\Sigma,y,j,i}\left(x_{j,i} - X_i\right) - f_{\Sigma,x,j,i}\left(y_{j,i} - X_i\right)\right) + M_{i+1} + \sum_{j=1}^{k}\left(f_{\Sigma,y,j,i+1}\right)L_i\cos(\theta_i) - \sum_{j=1}^{k}\left(f_{\Sigma,x,j,i+1}\right)L_i\sin(\theta_i)$$

Equation B-11

B.3 Forces based on added momentum method

Calculation of the hydrodynamic inertia forces based on added momentum is different from the calculation of the tangential forces in the normal way in that both tangential and perpendicular forces are calculated in one process. This solution does not rely on the calculation of the perpendicular forces from section 4.6 although some of the input variables will be the same.

As the added momentum method on its own, only computes inertia forces they will be computed before the expansion of perpendicular and tangential drag forces is added. The calculation of the hydrodynamic inertia forces is based on Equation 3-3. This is an expression of vectors and as it involves cross multiplication with the angular velocity vector, it has to be computed in all three dimensions. The normal acceleration vector, the first term in the expression would thus be:

$$\vec{\mathbf{a}}_{\perp,j,i} = \begin{bmatrix} \ddot{x}_{\perp,j,i} \\ \ddot{y}_{\perp,j,i} \\ 0 \end{bmatrix}$$

Equation B-12

In this equation, the accelerations in the X- and Y-directions would be the ones calculated in Equation 4-32. As the eel is assumed to be moving in just one plane, relative to its head the acceleration in the Z-direction is zero.

Similarly the angular velocity vector would be:

$$\boldsymbol{\omega}_i = \begin{bmatrix} 0 \\ 0 \\ \dot{\theta}_i \end{bmatrix}$$

Equation B-13

As the entire segment rotates as one, there would be just one angular velocity vector for all the elements of each segment.

The normal velocity vector would be:

$$\mathbf{v}_{\perp,j,i} = \begin{bmatrix} \dot{x}_{\perp,j,i} \\ \dot{y}_{\perp,j,i} \\ 0 \end{bmatrix}$$

Equation B-14

Again, the velocities in the X- and Y-directions would be taken from Equation 4-32.

The second term in Equation 3-3 can now be computed:

$$\boldsymbol{\omega}_i \times \mathbf{v}_{\perp,j,i} = \begin{bmatrix} -\dot{\theta}_i \dot{y}_{\perp,j,i} \\ \dot{\theta}_i \dot{x}_{\perp,j,i} \\ 0 \end{bmatrix}$$

Equation B-15

The third term in Equation 3-3 is slightly more complicated to compute, as it is the normal component of the cross multiplication that is needed. Again, this can be

found using the normal vector defined in Equation 4-16. This vector would however have to be defined in all three dimensions and thus becomes:

$$\vec{\mathbf{N}}_i = \begin{bmatrix} -\sin\theta_i \\ \cos\theta_i \\ 0 \end{bmatrix}$$

Equation B-16

The third term of Equation 3-3 would then read:

$$\perp \mathbf{v}_{i,j} \times \boldsymbol{\omega}_i = \left(-\dot{y}_{j,i}\dot{\theta}_i \sin\theta_i - \dot{x}_{j,i}\dot{\theta}_i \cos\theta_i\right) \begin{bmatrix} -\sin\theta_i \\ \cos\theta_i \\ 0 \end{bmatrix}$$

Equation B-17

In this expression, the velocities of the element would be computed by Equation 4-28 as they are the true velocities rather than a component of them.

The fourth and last term in Equation 3-3 contains the derivative of the normal velocity with respect to the segment length. As each segment is a non-flexible continuous body, this derivative will be the same for all its elements. The last term of Equation 3-3 also contains the tangential velocity. This has already been calculated in Equation B-2 but then only in two dimensions. As the eel moves only in the X- and Y-direction and as the tangential velocity is not involved in a cross multiplication the expressions from Equation B-3 will suffice:

$$\mathbf{v}_{T,i,j} \partial \mathbf{v}_{\perp,i} / \partial \zeta = \begin{bmatrix} \dot{x}_{T,j,i} \\ \dot{y}_{T,j,i} \end{bmatrix} \frac{\sqrt{\dot{X}_{\perp,i+1}^{\ 2} + \dot{Y}_{\perp,i+1}^{\ 2}} - \sqrt{\dot{X}_{\perp,i}^{\ 2} + \dot{Y}_{\perp,i}^{\ 2}}}{L_i}$$

Equation B-18

The total inertia force in the X- and Y-direction from Equation 3-3 can now be computed by the addition of the X- and Y-components of Equation B-12, Equation B-15, Equation B-17 and Equation B-18 and multiplying the sum with the constants as described in the equation. Not surprisingly, this expression has a zero component in the Z-direction.

The calculation of the drag forces proposed by Quiggin and Carson rely on the angle of incidence, denoted here as φ. This is the angle between the velocity of the flow and the element in question.

$$\varphi_{j,i} = \angle\begin{bmatrix}\dot{x}_{j,i}\\ \dot{y}_{j,i}\end{bmatrix} - \theta_i$$

Equation B-19

In this equation, the symbol $\angle$ signifies the angle of the velocity vector.

The rest of Equation 3-4 is equally straight forward:

$$f_{\perp,j,i} = \frac{1}{2}\rho\left(\dot{x}_{j,i}{}^2 + \dot{y}_{j,i}{}^2\right)\left(AP_{i,j}Cd\sin^2\varphi_{j,i} + sw_{i,j}Cn\sin\varphi_{j,i}\right)$$
$$f_{T,j,i} = \frac{1}{2}\rho\left(\dot{x}_{j,i}{}^2 + \dot{y}_{j,i}{}^2\right)\left(sw_{i,j}Ct\cos\varphi_{j,i}\right)$$

Equation B-20

Again $sw_{i,j}$ is the wetted surface area of the element in question whilst $AP_{i,j}$ is its projected area.

The problem with this equation is that it is given in local coordinates. To convert it to global coordinates an orientation matrix may be used:

$$\begin{bmatrix}\mathbf{f}_{\dot{x},j,i}\\ \mathbf{f}_{\dot{y},j,i}\end{bmatrix} = \begin{bmatrix}\mathbf{cos\theta}_i & \mathbf{-sin\theta}_i\\ \mathbf{sin\theta}_i & \mathbf{cos\theta}_i\end{bmatrix}\begin{bmatrix}\mathbf{f}_{\perp,j,i}\\ \mathbf{f}_{T,j,i}\end{bmatrix}$$

Equation B-21

The total force on this element will then be:

$$f_{\Sigma,x,j,i} = \frac{m_i}{k}\ddot{x}_{j,i} + G_{x,j,i} + f_{\dot{x},j,i}$$
$$f_{\Sigma,y,j,i} = \frac{m_i}{k}\ddot{y}_{j,i} + G_{y,j,i} + f_{\dot{y},j,i}$$

Equation B-22

In this equation, the inertia force G would be calculated according to Equation 3-3. The total instantaneous thrust for the eel would be found in the normal manner:

$$Thrust_{inst} = \sum_{i=1}^{n} \sum_{j=1}^{k} f_{\Sigma,x,j,i}$$

Equation B-23

Similarly, the calculation of the moment in the backmost joint would follow Equation 4-37 whilst the calculation of the moment in the i-th joint would follow Equation 4-38.

Appendix C Uncertainty in physical measurements

C.1 Introduction

Since model tests form a major part of this thesis, it is important to evaluate the uncertainty associated with them. This evaluation was inspired by the ITTC recommended procedure 7.5-02-02-02 and the book "Experimentation and uncertainty analysis for engineers" by Coleman and Steele.

The overall uncertainty is dependent on two main factors, the level of accuracy in the physical measurements and the level of accuracy in the data processing. The latter is a result of the substantial post-processing and the uncertainty introduced by this will be examined in Appendix D.

The measured data in this thesis were as follows:

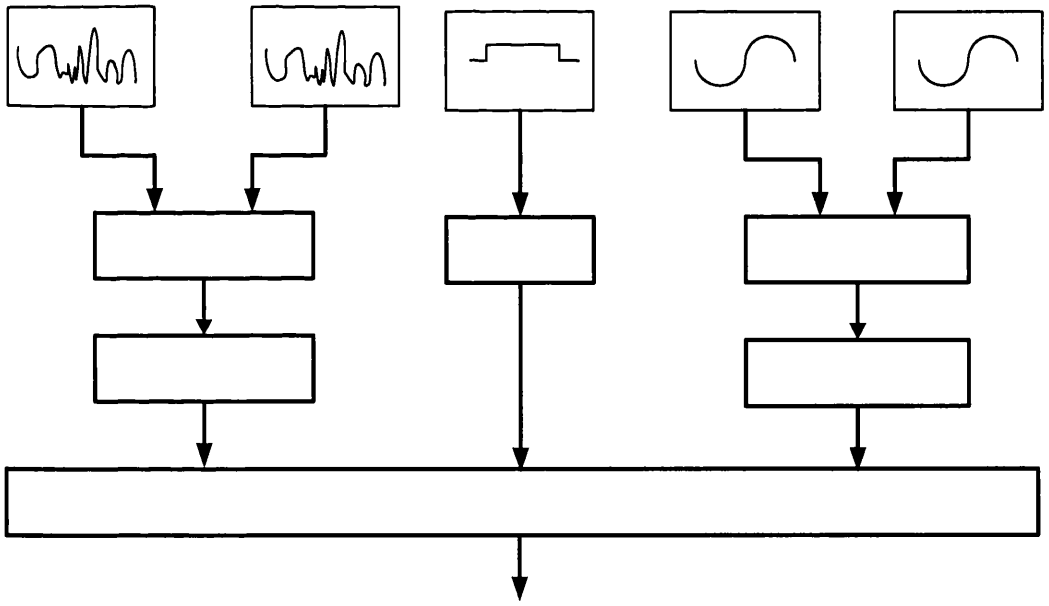

Figure C.1-1 the sources of errors in the measured data

C.2 The accuracy of the force measurements

All force measurements in this thesis were measured using a LMC-6524-1000N 6-component load cell made by Ogawa Seiki. This cell can measure forces up to 1 kN and it was feared that its accuracy in the range of interest was not sufficient. The load cell was therefore calibrated with several, certified weights to ensure both accuracy and linearity. The weights used were certified to M1 and thus accurate to ± 50 mg per kg or 0.005 %. The initial calibration was done on 18. February 2005 and a second calibration was performed after the eel had been tested on 21. March 2005. The ITTC Recommended Procedures 7.6-02-09 inspired these calibrations; following these recommendations, the load cell and its bridge amplifier (DSA-100 from Ogawa Seiki) were given at least half an hour to heat up before testing.

The load cell was mounted horizontally with the dummy sting attached to it. The weights were then placed on a point on the sting where the water line would intersect it during tank testing. This was done to ensure that the moment generated would be of a similar order as the one experienced during testing:

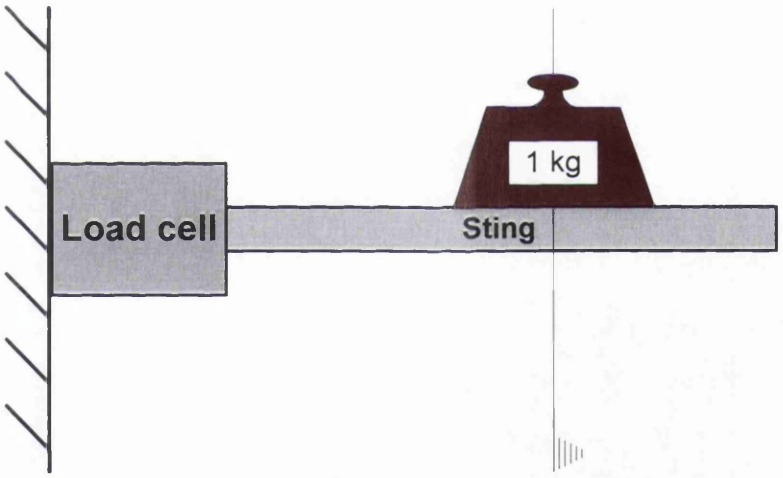

Figure C.2-1 load cell calibration

On the first day of load cell calibration the temperature in the testing area was 16 degrees centigrade.

The X- and Y-coordinates of the load cell were defined by the manufacturer (see E.1) and the load cell was first tested in its Y-direction:

Mass (kg)	Weight (N)	Measured (N)	Error
0.1	0.981	0.980	-0.08%
0.2	1.962	1.955	-0.35%
0.3	2.943	2.933	-0.34%
0.4	3.924	3.906	-0.47%
0.5	4.905	4.880	-0.52%
1.0	9.810	9.783	-0.27%
2.0	19.620	19.571	-0.25%
3.0	29.430	29.373	-0.19%
4.0	39.240	39.175	-0.17%
5.0	49.050	48.969	-0.17%
10.0	98.100	97.985	-0.12%
		Mean =	**-0.27%**

Table C-1

In this table, the masses are in kg and the forces are in N. A similar table for the X-direction was produced:

Mass (kg)	Weight (N)	Measured (N)	Error
0.1	0.981	0.989	0.82%
0.2	1.962	1.973	0.57%
0.3	2.943	2.957	0.47%
0.4	3.924	3.941	0.44%
0.5	4.905	4.921	0.32%
0.6	5.886	5.908	0.37%
0.7	6.867	6.887	0.30%
0.8	7.848	7.867	0.25%
0.9	8.829	8.861	0.37%
1.0	9.810	9.843	0.34%

2.0	19.620	19.659	0.20%
3.0	29.430	29.503	0.25%
4.0	39.240	39.316	0.19%
5.0	49.050	49.156	0.22%
		Mean =	**0.36%**

Table C-2

As the forces generated by the Eel in the X-direction are smaller than the ones generated in the Y-direction smaller weights were used for this set of tests. Since the load cell appeared to be more accurate in the Y-direction it was decided to turn it around 90 degrees compared to the model (for the coordinate system of the model see Figure 4-1). All longitudinal forces experienced by the eel and the dummy sting were therefore measured with the Y-direction of the load cell. When comparing the results from the second day of testing with those from the first it is important to remember that the load cell had been turned at this point and consequently the Y-direction results from the first day should be compared to the X-direction results from the second day and so on.

During the testing of the dummy sting and the McEel itself, several issues regarding the pre-filtering of the measured signals had arisen (see section 7.4). It was therefore decided to re-check the calibration for the load cell with the different pre-filter settings. The temperature in the test area was 18 degrees centigrade during this second day of testing. Looking firstly at the X-direction of the eel (Y-direction of the load cell):

mass	Weight	10 Hz	Error	100 Hz	Error	Pass	Error
1.0	9.810	9.682	-1.31%	9.696	-1.17%	9.689	-1.23%
2.0	19.620	19.367	-1.29%	19.374	-1.25%	19.366	-1.29%
3.0	29.430	29.053	-1.28%	29.059	-1.26%	29.052	-1.28%
4.0	39.240	38.733	-1.29%	38.746	-1.26%	38.731	-1.30%
5.0	49.050	48.417	-1.29%	48.429	-1.27%	48.411	-1.30%
10.0	98.100	96.839	-1.29%	96.872	-1.25%	96.835	-1.29%
	Mean =		-1.29%		-1.24%		-1.28%

Table C-3

In this table the errors in measurement for the three different filter settings of 10 Hz, 100 Hz and pass band are compared. As can be seen the error seems un-affected by the filter setting. It can also be noted that the errors are substantially bigger than they were before the testing in the tank began. The errors seem consistent and it seems as if the slope of the load against voltage curve has changed.

The same three points can be seen in the measurements in the new Y-direction:

mass	Weight	10 Hz	Error	100 Hz	Error	Pass	Error
1.0	9.810	9.945	1.38%	9.939	1.32%	9.928	1.20%
2.0	19.620	19.901	1.43%	19.872	1.28%		
3.0	29.430	29.845	1.41%	29.808	1.29%	29.825	1.34%
4.0	39.240	39.823	1.49%	39.747	1.29%	39.739	1.27%
5.0	49.050	49.772	1.47%	49.683	1.29%	49.679	1.28%
10.0	98.100	99.558	1.49%	99.414	1.34%	99.404	1.33%
	Mean =		1.44%		1.30%		1.29%

Table C-4

It is not certain why the slope of the load against voltage curve has changed. The slight difference in temperature does not explain such a large shift and it is tempting to regard it as a random error with a long period.

In their book, Coleman and Steele (1999) suggest that any experimental quantity should be reported with at least four values. These values are the measured value, the corresponding systematic and random errors and the confidence level. The force measurements reported in chapter 6 rely solely on the accuracy of the load cell and its data collection system. The three missing quantities should therefore be evaluated. This is harder than might be anticipated.

As the Y-direction of the load cell always measure less than the actual load and the X-direction always measures more than the actual load it is tempting to call this systematic rather than random uncertainty. It could however be that the time variations in the random uncertainty of the load cell are of such a long period that they appear to be systematic. Without further tests, there is no way of knowing which

one of these it is. The worst of the errors in the load cell measurements must therefore be considered the total uncertainty of the load cell.

As the load cell was tested on two occasions and with numerous different weights, one might expect to be able to compute a confidence level for the reported uncertainty. There are however numerous questions about which measurements to include in this computation. On the second day of testing it was shown how the pre-filter settings were of little importance when measuring the forces from the weights. The question then arises as to whether all the measurements from this second day of testing should be included or whether the computation should be limited to those from the 10 Hz setting as this value was used during experiments? Should the level of confidence be based on measurements from both days of testing? It seems that if a confidence level was to be reported reliably, load cell calibrations would have had to have been a much more frequent exercise during this study.

The errors reported in Table C-3 and Table C-4 should therefore be seen as an indication of the uncertainty of the force measurements reported in this thesis. As these measurements were performed with the load cell, the bridge amplifier and the data acquisition system all in their normal configuration, the errors given can be seen as the over all error for the force measurements.

C.3 The accuracy of the speed measurements

The speed measurements came from the towing tank carriage and went directly into the data acquisition system. The accuracy of the speed measurements had been measured just a few weeks previous as part of the commissioning of a new speed control system. The speeds measured for this thesis are therefore assumed to be accurate to within 0.01 %.

C.4 The accuracy of the angular measurements

During the initial set up of the McEel great care was taken to ensure the accuracy of the angular measurements. This was in part because they formed a part of the control

system as seen in Figure 5-14. During this process it became apparent that the majority of the inaccuracy in the angular positioning, as well as the angular measuring stemmed from mechanical inaccuracies. The timing belts that controlled the position of the eel were high quality low stretch belts but each joint could still be moved 1.5-2 degrees to either side with the motors jammed in one position.

The inaccuracy of the potentiometers and the data acquisition system are therefore of limited importance when it comes to ascertaining the overall inaccuracy of the angular measurements. What could be important however is the dynamic inaccuracy caused by stretching of the belts. This inaccuracy was evaluated in Figure 5-15.

Appendix D Uncertainty in data processing

Once the data had been collected by the data acquisition system it was filtered and compared to the theoretical model. The only source of error in the data processing for the measured data is the fast Fourier filtering. When it comes to the calculated data there are however more sources. As the more advanced numeric methods were solved numerically rather than analytically the number of elements, which each segment was subdivided into is of importance. Similarly, numeric derivation was used and the number of time steps per cycle is therefore important.

D.1 Fourier analysis

Before the uncertainty introduced by the Fourier filtering of the two force signals can be quantified, the assumptions behind the process need to be stated:

- The force signal and the noise are independent of each other.
- Although the noise is spread over a wide frequency range, there is limited or no noise in the exact frequencies of the signal.

Great care was taken to try to eliminate the noise that was overlapping the force signals. For this reason it seems reasonable to assume that the noise was of a mechanical rather than electrical nature as it would have be possible to eliminate the majority of the latter. The measured noise therefore implies that the system was undergoing excitations at frequencies other than the ones generated by the motion of the eel. These vibrations could also be observed during testing. These motions were however small in comparison to the overall motions of the eel and it therefore seems fair to assume that they would not greatly influence the forces generated by the eels prescribed motion.

The second assumption is more questionable as the frequencies of the noise were in some cases very close to those frequencies that were of interest. This can be seen in Figure 7-1. When examining this figure it is however important to remember that only the 0 Hz value and the two first harmonics are included in the analysis. The second assumption therefore seems reasonable.

The uncertainty introduced by the Fourier filtering can now be evaluated by the analysis of an artificial test file with known components. For this purpose, a force signal was constructed of these parts:

	Longitudinal		Transverse	
	Frequency	Amplitude	Frequency	Amplitude
1. component	0	6.0	0	0
2. component	2.0	10.0	1.0	50.0
3. component	4.0	2.0	3.0	10.0

Table D-1

This force signal is designed to resemble one generated by the McEel when oscillating at 1.0 Hz.

This force signal was then polluted with 20 random noise components in each direction. These noise components had mean amplitude of 20 N in the longitudinal direction and 40 N in the transverse direction. In both directions the noise was randomly distributed around 8 Hz with a standard deviation of 2.5 Hz. The force signals were then filtered using a fast Fourier transform function. This process was repeated 300 times to ensure consistency. The filtered and unfiltered force signals typically looked like this:

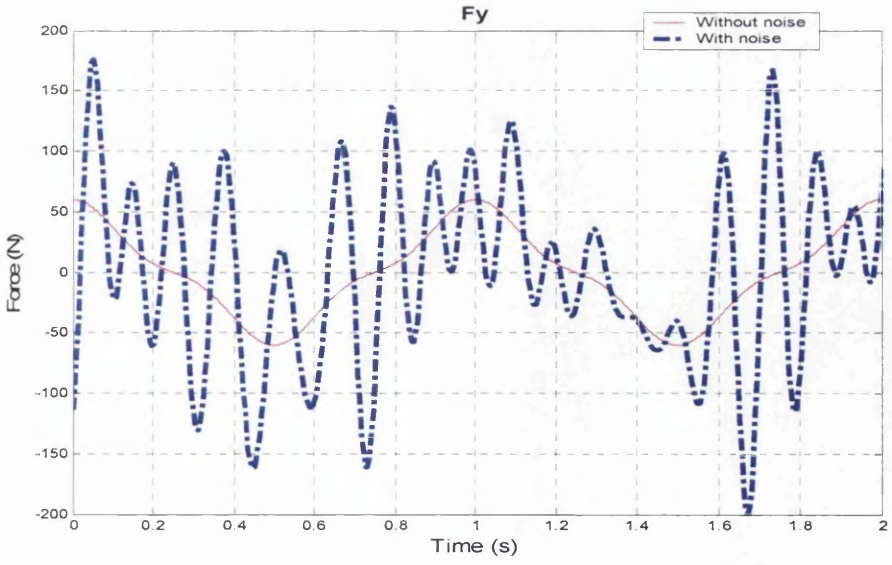

Figure D.1-1 the constructed force signal before and after filtering. Y-direction.

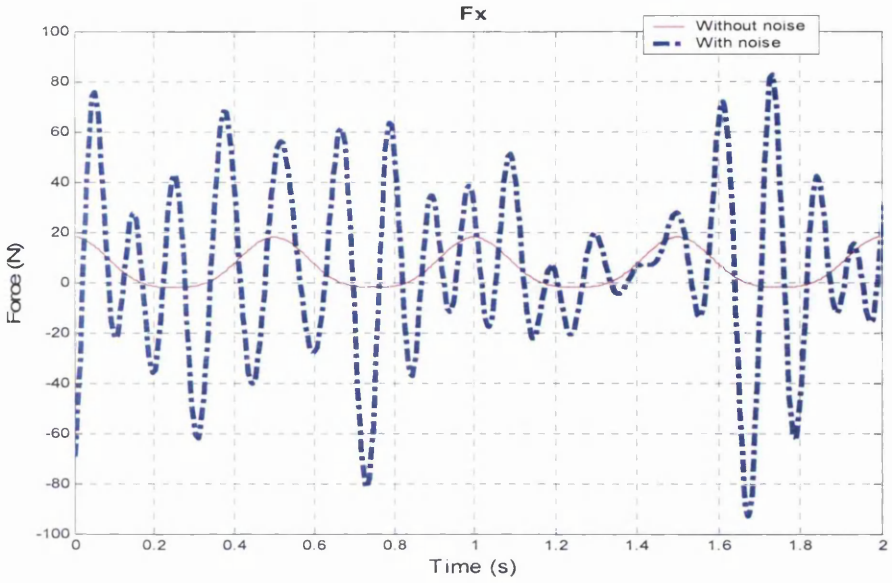

Figure D.1-2 the constructed force signal before and after filtering. X-direction.

These force plots can be compared with the ones in Figure 7-8 and Figure 7-9.

The computed values for the various frequency components varied substantially during the 300 tests. A plot of the three frequency components in the transverse direction shows this:

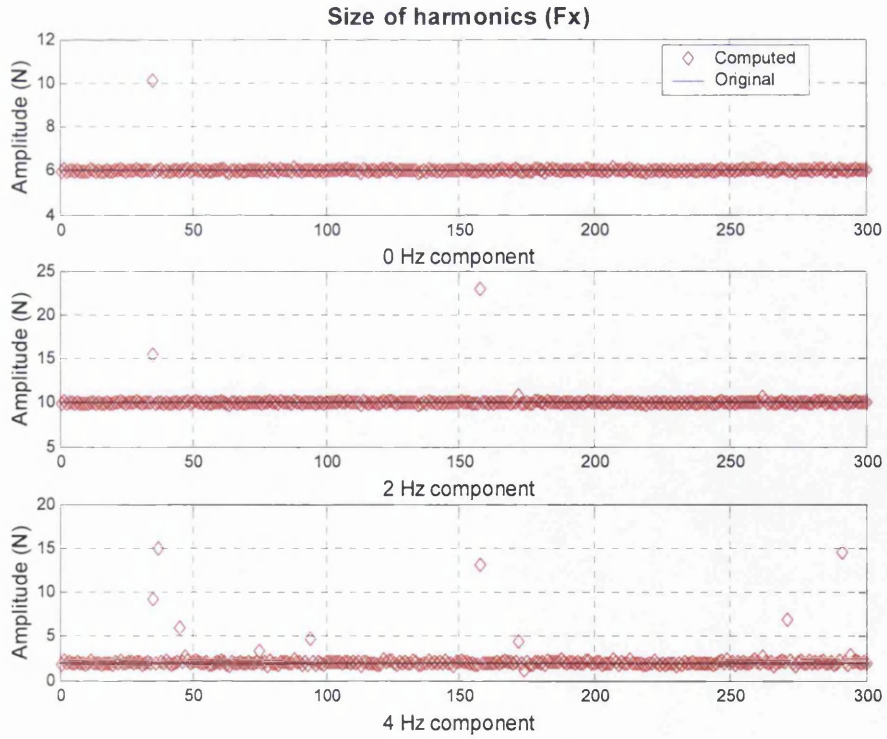

Figure D.1-3 the magnitude of the frequency components

In this plot, it can be seen that the estimates from the Fourier analysis is very good in most of the 300 trials but produces a few bad ones. As all the tests presented in this thesis have been analysed numerous times it seems reasonable to exclude these erroneous results using Chauvenet's criterion (Coleman and Steele 1999). After excluding these frequency components, the computed values become:

	Longitudinal			Transverse		
	Frequency	Mean	Std	Frequency	Mean	Std
1. component	0	6.005	0.040	0	0.016	0.080
2. component	2	10.010	0.107	1	50.018	0.163
3. component	4	2.047	0.362	3	10.007	0.230

Table D-2

Once consistency is ensured, fast Fourier filtering is a very accurate process and the plots of the filtered and original signals shown in Figure D.1-4 and Figure D.1-5 show just how well this filter worked, compared to a Butterworth filter.

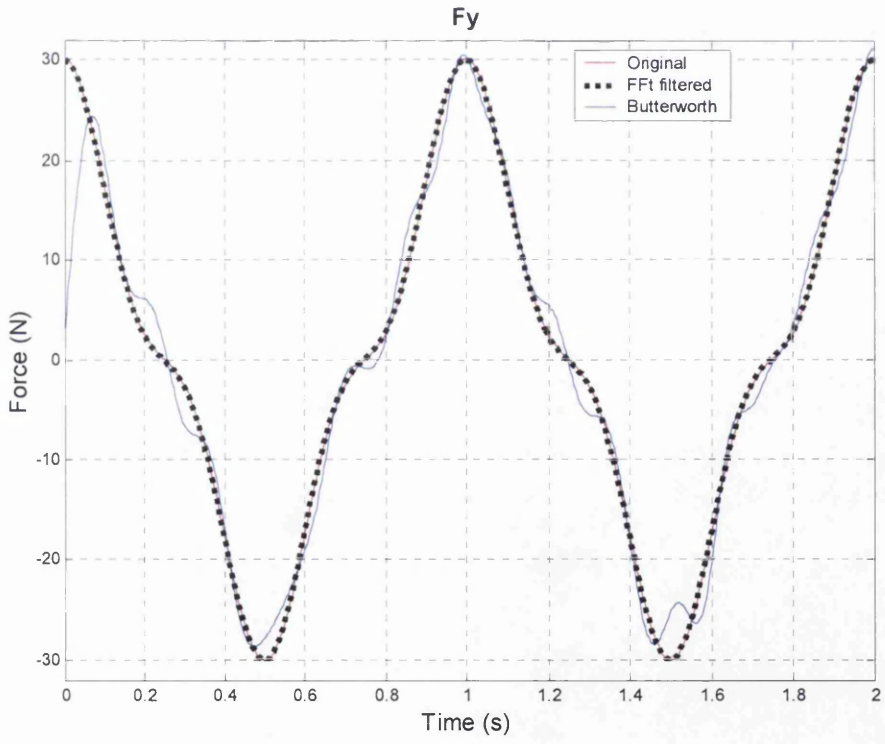

Figure D.1-4 the original and reconstituted signal, Y-direction.

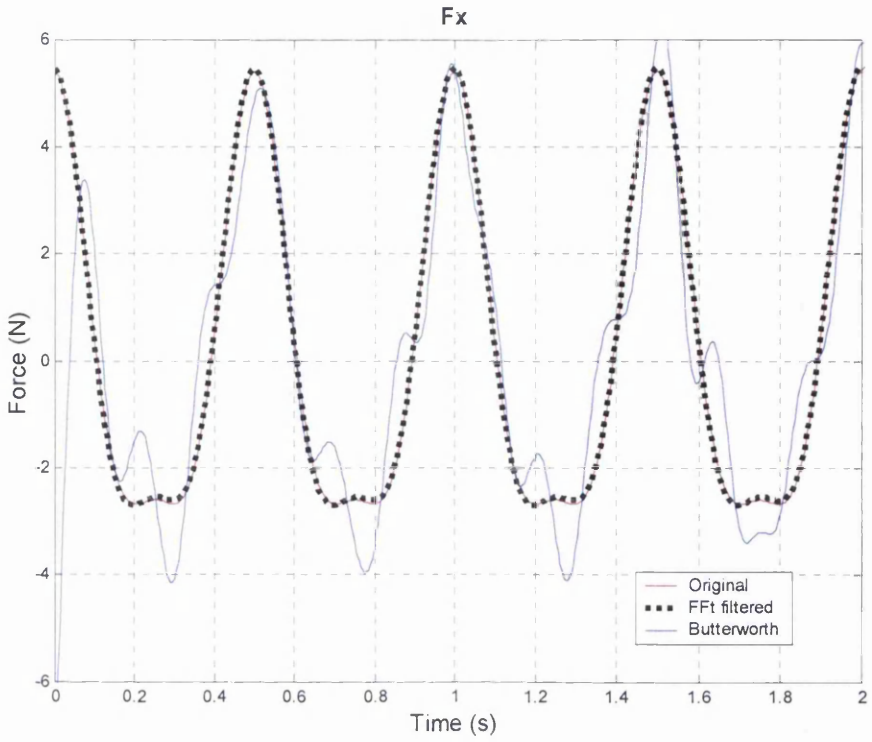

Figure D.1-5 the original and reconstituted force signal, X-direction

D.2 Segmentation

As explained previously all tests within this thesis are with a two segment eel. Most of the hydrodynamic models described are however non-linear and as a consequence there is a need for further segmentation of each of the segments. As described in section 4.4 these parts of the segments will be denoted as elements.

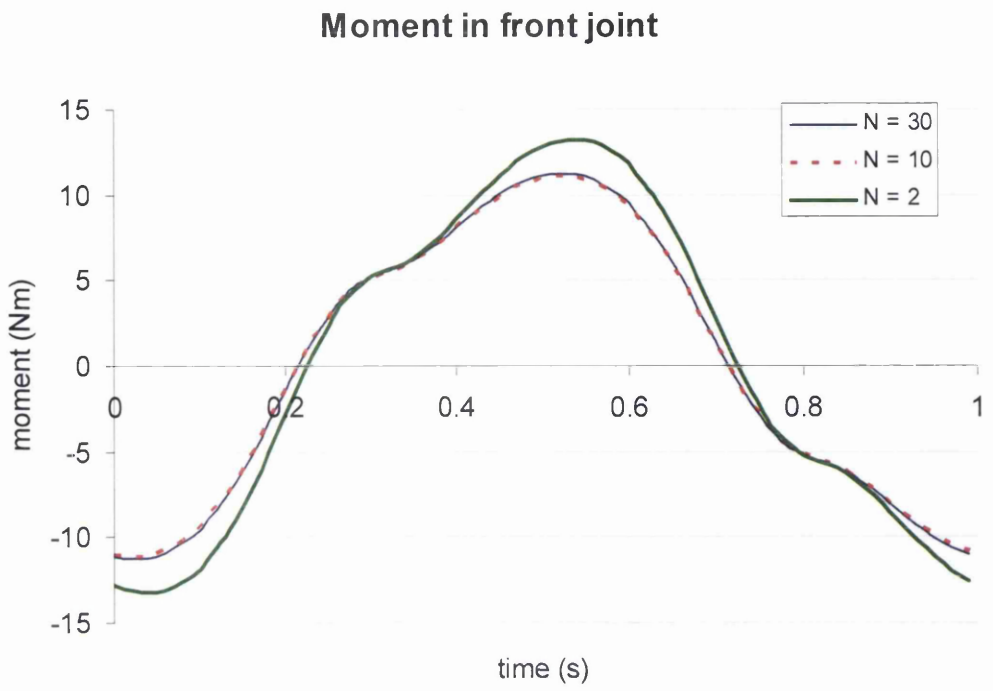

Figure D.2-1 the importance of segmentation

This graph shows the moment in the first joint computed using the added momentum method. The moment depicted is for the 30-40-60, 1 Hz scenario in the bollard pull condition.

As can be seen there is a noticeable difference between the graphs computed using two elements and ten elements per segment. The graphs using 10 and 30 elements are however over-lapping. As 30 elements per segment is within the computational resources available all distributed numeric, models in this thesis were segmented to this level. It is assumed that the error involved with using 30 elements per segment as opposed to an infinite number of elements is negligible.

D.3 Numeric derivation

To simplify the computational process all of the numeric methods in this thesis have been calculated using at least some form of numeric differentiation. For this reason, the number of time steps per cycle is clearly of importance. In the evaluation of the number of time steps required the method relying most heavily on numerical

differentiation, the moment predictions from the added momentum method will therefore be examined:

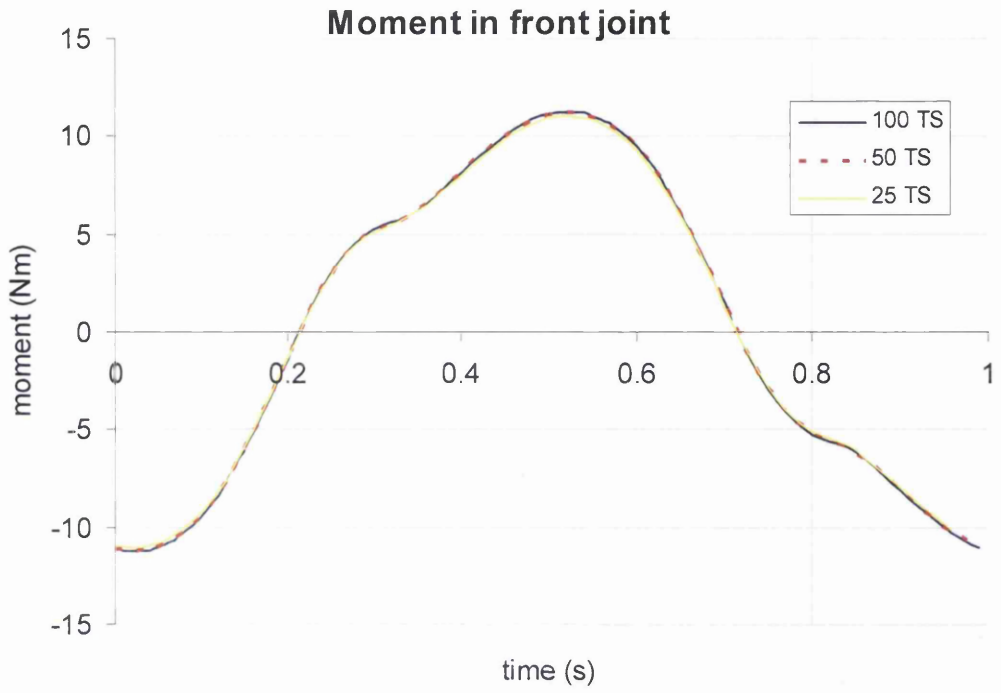

Figure D 3-1 the importance of the time steps

In this figure, the moment in the forward joint is calculated with 100, 50 and 25 time steps. The calculated moments are still based on the 30-40-60 1 Hz bollard pull scenario. The maximum variation between the calculated moments is 0.2 Nm. The maximum difference between the moments calculated using 100 time-steps and the one using 50 time-steps is 0.05 Nm or 0.4 %. Fifty time steps should thus be sufficient but as 100 time steps was within the computational capabilities, all numeric models used this level of differentiation.

D.4 Total uncertainty in numerically derived quantities

The numerically derived quantities reported in this thesis are the force coefficients and the mean and time dependent computed forces. The final uncertainty of these qualities will depend on both the uncertainty in the measured values and the uncertainty in the numeric processes.

In order to verify the computational procedure various artificial data files were created for the different numeric methods. Pre-defined force coefficients were used to create these and the various programs ability to re-create them can be seen as an indication of the uncertainty in this numeric process.

	No Kc		Kc		Added momentum	
	Given	Error	Given	Error	Given	Error
added mass	0.60	0.83%	0.10	4.80%	0.60	0.63%
pressure drag	4.00	1.25%	8.50	0.59%	4.00	1.33%

Table D-3

To make the generated files realistic random noise was included in them and for this reason the error in the force coefficients varied. The errors given are the worst ones.

Table D-3 indicates that the numeric processes are capable of determining the true force coefficients to a high level of accuracy. The biggest percentage error is for the constant part of the added mass coefficient in the method with Kc dependent force coefficients. Although a bigger percentage error than one might have wanted, this error is the smallest one in real terms.

In order to quantify the potential errors in the force coefficients caused by erroneous force measurements the same data file was analysed three times. The first time it was analysed in its original form. The second and third time the measured forces were multiplied by 1.01 and 0.99 respectively to emulate a 1 % error in force measurements.

	No error	+ 1 %	- 1 %
added mass	0.08	0.08	0.08
pressure drag	6.30	6.39	6.27

Table D-4

In this table, it can be seen how an error in force measurements of one percent results in an error in force coefficients of up to 1.5 %.

In addition to the uncertainties in the force measurements and the uncertainties in the numeric method, there are other uncertainties that affect the total uncertainty of the force coefficients. These include uncertainties in the dimensions of the eel and uncertainties in other physical measurements. It does however seem reasonable to assume these inaccuracies to be negligible. The total uncertainty in the force coefficients can then be computed:

$$\frac{U_c}{c} = \sqrt{UMF_m \left(\frac{U_m}{m}\right)^2 + UMF_F \left(\frac{U_F}{F}\right)^2}$$

Equation D-1

This equation is taken from Coleman and Steele (1999). U is the uncertainty with the subscript c meaning the force coefficient, m meaning the numeric method and F meaning the force measurements. Since relative uncertainties are the ones of interest, all uncertainties are divided by the quantity to which they refer. The UMF is the Uncertainty Magnification Factor and in the case of the force measurements, this factor was found in Table D-4 to be 1.5. It is harder to estimate this quantity for the numeric method. It does however seem reasonable to assume that it would take the same value as for the force measurements as both of them refer to the effect an erroneous force has on the computed force coefficient. The total relative uncertainty in the force coefficients is then just over 6 %.

The errors in the time dependent and mean force measurements also depend upon the uncertainty in the numeric method and the uncertainty in the force measurements. The only difference is that the UMF would be one. The relative uncertainty of the measured forces is then just under 5 %.

Appendix E Datasheets

E.1 Load cell

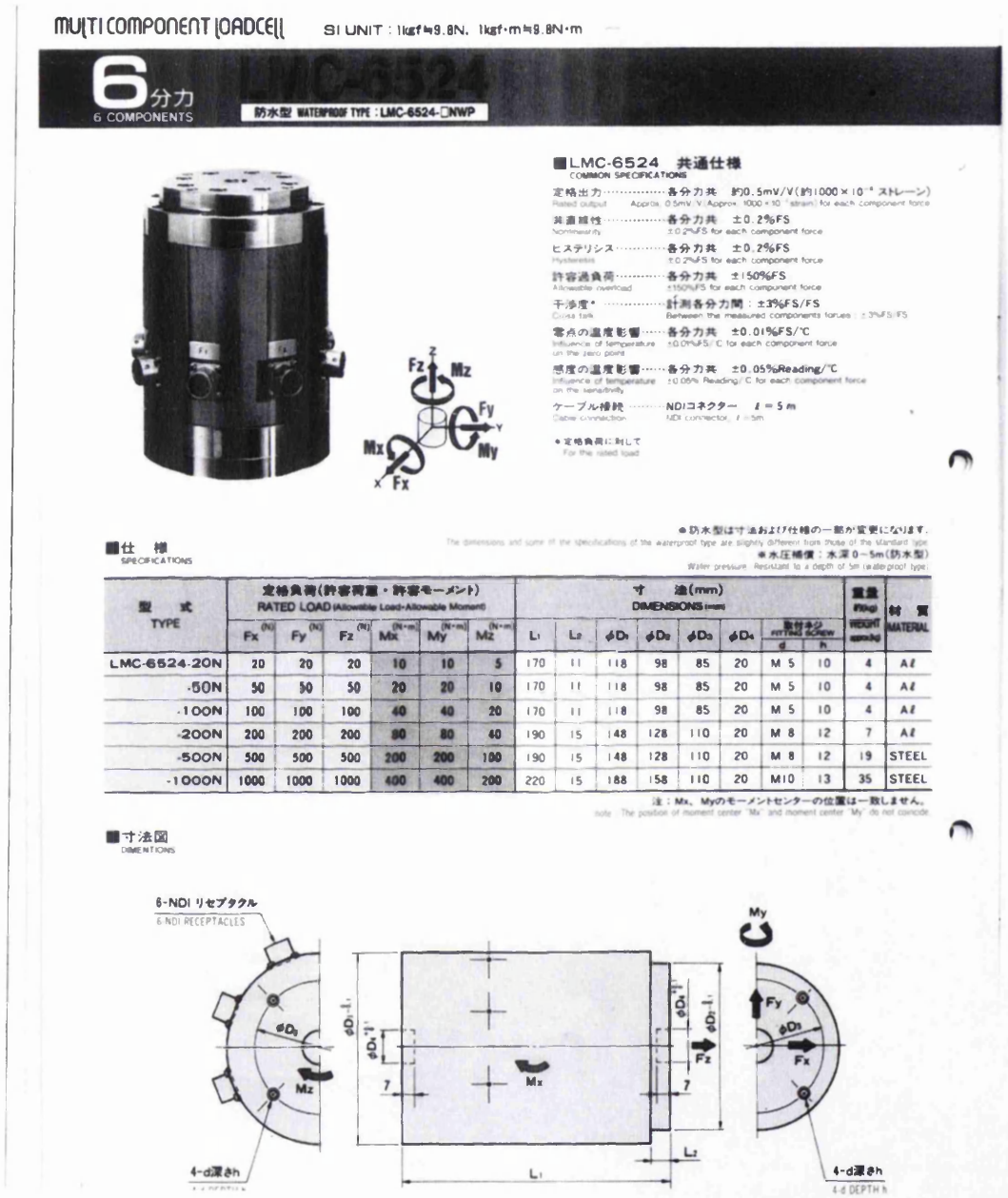

MULTI COMPONENT LOADCELL SI UNIT : 1kgf≒9.8N, 1kgf·m≒9.8N·m

6分力 6 COMPONENTS LMC-6524

防水型 WATERPROOF TYPE : LMC-6524-□NWP

■LMC-6524 共通仕様
COMMON SPECIFICATIONS

定格出力……各分力共 約0.5mV/V(約1000×10⁻⁶ ストレーン)
Rated output Approx. 0.5mV/V (Approx. 1000×10⁻⁶ strain) for each component force

非直線性……各分力共 ±0.2%FS
Nonlinearity ±0.2%FS for each component force

ヒステリシス……各分力共 ±0.2%FS
Hysteresis ±0.2%FS for each component force

許容過負荷……各分力共 ±150%FS
Allowable overload ±150%FS for each component force

干渉度* ……計測各分力間 : ±3%FS/FS
Cross talk Between the measured components forces : ±3%FS/FS

零点の温度影響……各分力共 ±0.01%FS/℃
Influence of temperature on the zero point ±0.01%FS/℃ for each component force

感度の温度影響……各分力共 ±0.05%Reading/℃
Influence of temperature on the sensitivity ±0.05% Reading/℃ for each component force

ケーブル接続……NDIコネクター l=5m
Cable connection NDI connector, l=5m

*定格負荷に対して
For the rated load

■仕 様 SPECIFICATIONS

*防水型は寸法および仕様の一部が変更になります。
The dimensions and some of the specifications of the waterproof type are slightly different from those of the standard type.
*水圧補償 : 水深0~5m(防水型)
Water pressure : Resistant to a depth of 5m (waterproof type)

型式 TYPE	定格負荷(許容荷重・許容モーメント) RATED LOAD (Allowable Load-Allowable Moment)						寸法(mm) DIMENSIONS (mm)								重量(kg) WEIGHT approx.	材質 MATERIAL
	Fx (N)	Fy (N)	Fz (N)	Mx (N·m)	My (N·m)	Mz (N·m)	L1	L2	φD1	φD2	φD3	φD4	取付ネジ FITTING SCREW d	h		
LMC-6524-20N	20	20	20	10	10	5	170	11	118	98	85	20	M 5	10	4	Al
-50N	50	50	50	20	20	10	170	11	118	98	85	20	M 5	10	4	Al
-100N	100	100	100	40	40	20	170	11	118	98	85	20	M 5	10	4	Al
-200N	200	200	200	80	80	40	190	15	148	128	110	20	M 8	12	7	Al
-500N	500	500	500	200	200	100	190	15	148	128	110	20	M 8	12	19	STEEL
-1000N	1000	1000	1000	400	400	200	220	15	188	158	110	20	M10	13	35	STEEL

注 : Mx、Myのモーメントセンターの位置は一致しません。
note : The position of moment center "Mx" and moment center "My" do not coincide.

■寸法図 DIMENSIONS

Figure E.1-1 datasheet for the load cell as supplied by the manufacturer

E.2 Bridge amplifier

直流型歪増巾器
DC STRAIN AMPLIFIER

DSA-100 DSAシリーズ DSA SERIES

DSAシリーズは、H章多分力検出器®の性能を十分に発揮するために設計され、高増巾度・高安定・低ノイズ性を誇る高精度の直流型歪増巾器です。

DSA-Series DC Strain Amplifiers are designed to help Nissho Multi-Component Load Cells® exhibit their full performance. They are very stable and precise amplifiers offering high amplification and low noise.

■特長 FEATURES

- 増巾率（最大17000倍）が非常に高い。
- 直線性が良い。（0.005%FS）
- 平衡調整範囲を粗調・微調の2段とし、調整しやすい。
- 0.3Hzまでのローパスフィルタが内蔵されている。
- 過渡特性が非常に良い。
- ダイナミックファクタが4倍あり、平均値を高精度で計測できる。
- 零点変動、ノイズが少ない。
- コモンモードノイズ除去に優れている。
- 大電流出力の可能な出力が2系統あり、相互に干渉がない。
- 高性能直流増巾器として使用可能。

■仕様 SPECIFICATIONS

ご要望に応じ2～6チャンネルの筐体組込みが可能です。

適用検出器	60Ω～2kΩ
ED加電圧	DC 3、6、9、12V±0.2% 50mA
平衡調整範囲	粗調：±5mV/V（±10000×10⁻⁶ひずみ） 微調：粗調の1/50
入力電圧範囲	±100mV最大
入力抵抗	10MΩ+10MΩ平衡差動
増巾度	最大17000倍
感度調整器	0.1/1、1/2、1/5、1/10、1/20、1/50 ±0.2%および1/1～1/3連続可変
定格出力	±10V 2系統、出力抵抗各50Ω（BNCコネクタケーブル1.5m 1本）
	出力電流合計 ±100mA
零点変動	0.3μV/℃、3μV/24H（入力換算値）
感度変化	測定値の0.01%/℃、0.03%/24H
非直線性	0.005%FS
フィルタ	周波数レンジ：0.3、1、3、10、30、100、300Hz、PASS（2kHz）
	減衰特性：−12dB/oct. ベッセル型

ノイズ（アンプ単体において）	周波数レンジ（Hz）	0.3	1	3	10	30	100	300	PASS
	入力換算（μVp-p）	0.2	0.2	0.2	0.3	0.4	0.6	0.8	1.5

ダイナミックファクタ	400%
較正ひずみ*	±50、100、200、500、1000、2000、5000×10⁻⁶ひずみ ±（0.2%+0.5×10⁻⁶ひずみ）入力信号に重畳 *但し、ゲージ率2.00のときのひずみ数値
所要電源	AC 100V±10% 50/60Hz 20VA
消費電力	約6 5W/1ch
ケーブル	1chにつき3m 1本付

■外形寸法図 EXTERNAL DIMENSIONS

重量：DSA-100-1ch 約3kg
DSA-100-6ch（ケース組入） 約20kg
DSA-100-6ch（ケースのみ） 約4kg

DSA-100 1チャンネル

パネルカット寸法 PANEL CUT OUT DIMENSIONS

■医体組込み外形寸法図 EXTERNAL DIMENSIONS OF THE AMPLIFIER WITH THE CASE

3チャンネル（ケース組込型） 3チャンネル+4½ DPMM付

6チャンネル（ケース組込型）

6チャンネル（ラック収納型）

20

Figure E.2-1 datasheet for the bridge amplifier as supplied by the manufacturer

E.3 Potentiometers

VISHAY

Model 533, 534, 535
Vishay Spectrol

7/8" (22mm) Precision Wirewound Potentiometer

ADDITIONAL FEATURES
- Special Resistance Tolerances to 1%
- Rear Shaft Extensions and Support Bearing
- Non Turn Lug
- Dual Gang Configuration and Concentric Shafts
- High Torque and Center Tap
- Special Markings and Front Shaft Extensions
- Servo Unit available and Slipping Clutch

Note: The color of this product is changing to blue, during the internal period you may recieve either black or blue.

ELECTRICAL SPECIFICATIONS

PARAMETER	MODEL 533	MODEL 534	MODEL 535
Resistance Range Standard Values	50Ω to 20KΩ	100Ω to 100KΩ	50Ω to 50KΩ
Capability Range	5Ω to 60KΩ	10Ω to 200KΩ	5Ω to 100KΩ
Standard Tol	± 5%	± 5%	± 5%
Linearity (Independent)	± 0.25%	0.20%	± 0.25%
Noise	100Ω ENR	100Ω ENR	100Ω ENR
Rotation (Electrical & Mechanical)	1080° ± 10%	3600° ± 10%	1800° ± 10°
Power Rating (@ 70°C)	1.0 watts	2.0 watts	1.5 watts
Insulation Resistance	1000MΩ minimum 500VDC		
Dielectric Strength	1000V_{RMS} minimum 60Hz		
Absolute Minimum Resistance	Not to exceed linearity x total resistance or 1Ω, whichever is greater		
Tempco	20ppm/°C (standard values, wire only)		
End Voltage	0.25% of total applied voltage, maximum		
Phasing	CCW end points - section 2 phased to section 1 within ± 2°		
Taps	Center tap only		

MARKING

Unit Identification	Manufacturer's name and model number, resistance value and tolerance, linearity specification date code and terminal identification

RESISTANCE VALUES

Ohms	
533:	50R, 100R, 200R, 500R, 1K, 2K, 5K, 10K, 20K
534:	100R, 200R, 500R, 1K, 2K, 5K, 10K, 20K, 50K, 100K
535:	50R, 100R, 200R, 500R, 1K, 2K, 5K, 10K, 20K, 50K

ORDERING INFORMATION

The Models 533 (3 turn), 534 (10 turn) and 535 (5 turn) can be ordered by stating

534	1	2	XXX
MODEL	MOUNTING	NUMBER OF SECTIONS	RESISTANCE EIA CODE
	1. Bushing 2. Servo	1. Single section 2. Dual section	

Document Number: 57065
Revision 09-Jan-04

For technical questions, contact sfer@vishay.com

www.vishay.com
1

Figure E.3-1 datasheet for potentiometers page 1

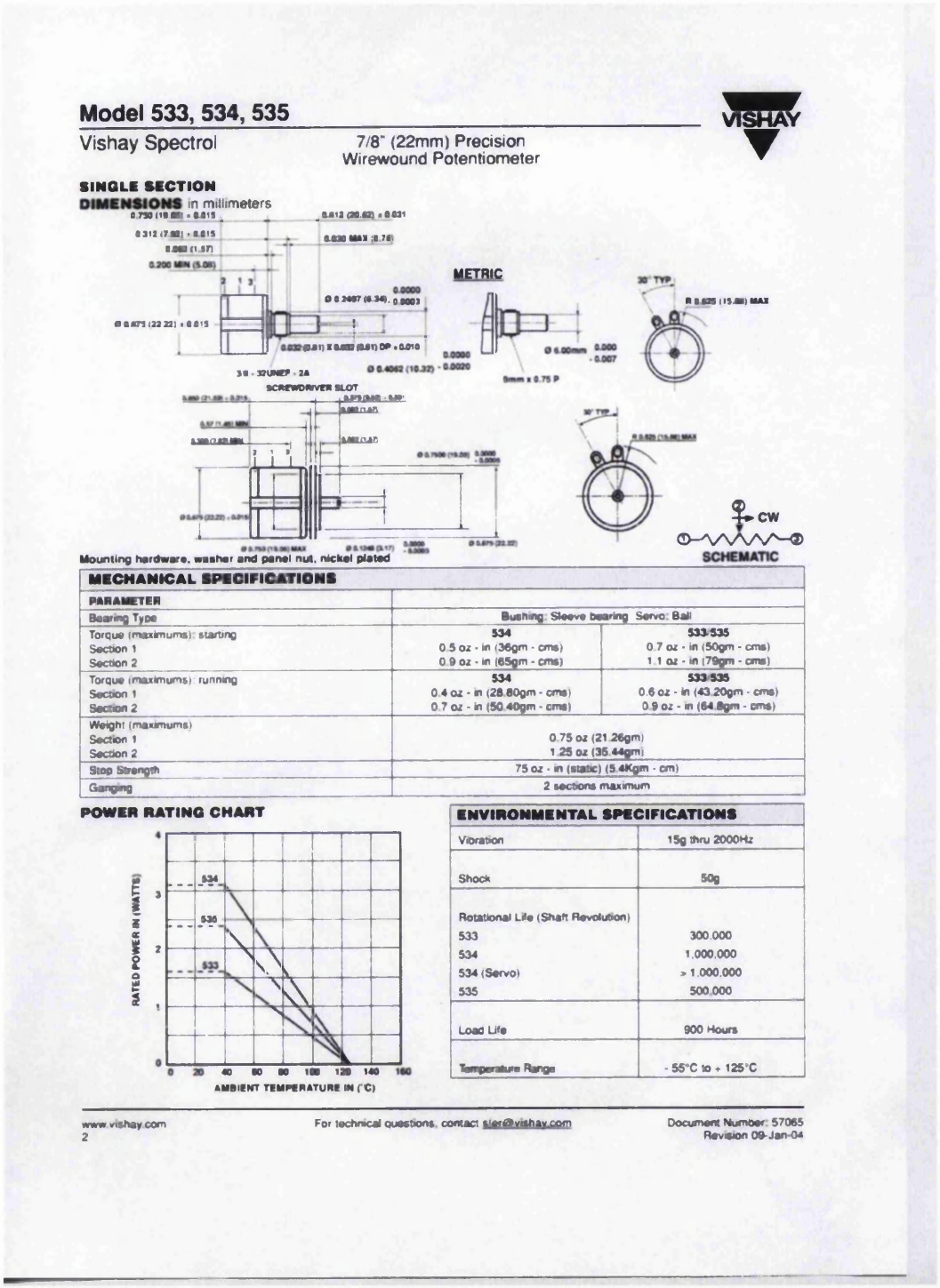

Model 533, 534, 535

Vishay Spectrol — 7/8" (22mm) Precision Wirewound Potentiometer

VISHAY

SINGLE SECTION

DIMENSIONS in millimeters

Mounting hardware, washer and panel nut, nickel plated

MECHANICAL SPECIFICATIONS

PARAMETER		
Bearing Type	Bushing: Sleeve bearing Servo: Ball	
Torque (maximums): starting Section 1 Section 2	534 0.5 oz - in (36gm - cms) 0.9 oz - in (65gm - cms)	533/535 0.7 oz - in (50gm - cms) 1.1 oz - in (79gm - cms)
Torque (maximums): running Section 1 Section 2	534 0.4 oz - in (28.80gm - cms) 0.7 oz - in (50.40gm - cms)	533/535 0.6 oz - in (43.20gm - cms) 0.9 oz - in (64.8gm - cms)
Weight (maximums) Section 1 Section 2	0.75 oz (21.26gm) 1.25 oz (35.44gm)	
Stop Strength	75 oz - in (static) (5.4Kgm - cm)	
Ganging	2 sections maximum	

POWER RATING CHART

ENVIRONMENTAL SPECIFICATIONS

Vibration	15g thru 2000Hz
Shock	50g
Rotational Life (Shaft Revolution)	
533	300,000
534	1,000,000
534 (Servo)	> 1,000,000
535	500,000
Load Life	900 Hours
Temperature Range	- 55°C to + 125°C

Figure E.3-2 datasheet for the potentiometers page 2

VISHAY

Model 533, 534, 535

7/8" (22mm) Precision Wirewound Potentiometer

Vishay Spectrol

RESISTANCE ELEMENT DATA

RESISTANCE VALUE (Ω)			RESOLUTION %			OHMS PER TURN			MAX CURRENT AT 70°C AMBIENT (mA)			MAX VOLTAGE ACROSS COIL (V)		
533	534	535	533	534	535	533	534	535	533	534	535	533	534	535
50	–	50	0.149	–	0.120	0.0746	–	0.0603	141.0	–	173.0	7.07	–	8.66
100	100	100	0.111	0.060	0.075	0.1114	0.0603	0.0746	100.0	141.0	122.0	10.0	14.1	12.2
200	200	200	0.097	0.037	0.061	0.1954	0.0746	0.1220	70.7	100.0	86.6	14.1	20.0	17.3
500	500	500	0.069	0.031	0.049	0.3424	0.1520	0.2459	44.7	63.2	54.7	22.4	31.6	27.4
1K	1K	1K	0.063	0.025	0.041	0.6331	0.2459	0.4113	31.6	44.7	38.7	31.6	44.7	38.7
2K	2K	2K	0.041	0.021	0.031	0.8206	0.4113	0.6331	22.4	31.6	27.4	44.7	63.2	54.8
5K	5K	5K	0.044	0.016	0.034	2.2330	0.8206	1.7230	14.1	20.0	17.3	70.7	100.0	86.6
10K	10K	10K	0.034	0.017	0.030	3.4510	1.7230	3.0160	10.0	14.1	12.2	100.0	141.0	122.0
20K	20K	20K	0.031	0.015	0.020	6.1790	3.0160	3.9910	7.07	10.0	8.66	141.0	200.0	173.0
–	50K	50K	–	0.009	0.015	–	4.6690	7.4560	–	6.32	5.47	–	316.0	274.0
–	100K	–	–	0.007	–	–	7.4560	–	–	4.47	–	–	447.0	–
–	–	–	–	–	–	–	–	–	–	–	–	–	–	–
–	–	–	–	–	–	–	–	–	–	–	–	–	–	–

Figure E.3-3 datasheet for the potentiometers page 3